From Cataclysmic Variables to AM CVn Systems
Modeling LISA Gravitational Wave Sources Using MESA

AALBORG UNIVERSITY

DENMARK

Masters Thesis

Physics

Aalborg University

Submitted: 30-05-2025

Casper Christian Pedersen

Hans Christian Gjedsig Larsen

Title Sheet

Physics
Department of Materials and Production
9000 Aalborg

Title:

From Cataclysmic Variables to AM CVn Systems:

Modeling LISA Gravitational Wave Sources Using MESA

Project:

Master Thesis

Project Period:

September 2024 - May 2025

Participants:

Casper Christian Pedersen

Hans Christian Gjedsig Larsen

Supervisor:

Thomas Tauris

Number of Pages:

72

Number of Appendix Pages:

10

Abstract:

The aim of this thesis is to simulate AM CVn binaries, using the cataclysmic variable formation channel to provide insight into the expected gravitational strain amplitudes of AM CVns and the detectability with respect to THE Laser Interferometer Space Antenna (LISA). Relevant physics including mass transfer, novae eruptions, magnetic braking and gravitational wave radiation is presented to give an overview of the different effects, which play a role in the evolution of these systems. The convection and rotation boosted (CARB) magnetic braking prescription is used. Furthermore, the strain amplitude of the gravitational wave signal and the LISA sensitivity curves were included to evaluate the gravitational signal received from these binaries.

Modules for Experiments in Stellar Astrophysics, MESA, version 24.08.1 is used to simulate the evolution of these systems, implementing the presented physics. To evaluate the simulations, we found observational data for AM CVn systems to use as benchmarks, and evolved CV systems. The latter were included such that we can determine whether we also are able to reproduce these, which is required following the assumed evolution.

We found that it is possible to reproduce known AM CVn systems, assuming this CV evolutionary channel. Furthermore, our simulated systems shows strong gravitational wave signals and most are detectable with LISA, once operational. The CARB magnetic braking model was found to have a strong impact on the evolution of these AM CVn systems. The initial parameter fine-tuning was resolved by using this stronger model. However, this model also caused our simulated systems to yield higher mass transfer rates than that of the observational data in the AM CVn phase. Turning of magnetic braking for the compact donors yielded better results, however during so caused too low mass transfer rates. Thus another prescription is needed for compact donors in order to reproduce more observed systems.

Preface

This thesis project was carried out by 4th semester master students in Physics at Aalborg University - Department of Materials and Production, in collaboration with Thomas Tauris as our supervisor.

The sources are referenced to with the apalike method and are found in the bibliography in alphabetical order. Furthermore, references to equations are noted with parenthesis around the equation number.

Generative artificial intelligence (AI) has been used as a source of inspiration for both coding solutions and sentence formulation. Further, the spell checking AI tool Writefull, integrated in Overleaf, has been utilized.

We would like to express our sincere gratitude to our supervisor Thomas Tauris for his invaluable guidance and for providing us, and others, with numerous opportunities to work in the field of astrophysics during our time here at Aalborg University.

Hans Christian G. Larsen
hcgl20@student.aau.dk

Casper Christian Pedersen
ccpe20@student.aau.dk

Summary

The aim of this thesis is to simulate AM CVn binaries, using the cataclysmic variable formation channel to provide insight into the expected gravitational strain amplitudes of AM CVns and the detectability with respect to LISA.

We start with a chapter on the preliminary theory of the relevant physics, which play a prominent role for these systems. This starts with an overview of the evolutionary channels these AM CVns can form from. Afterwards a section about mass transfer is included. Here the Eddington accretion limit for a white dwarf is also presented, which limits the amount of material it can accrete. Another effect that determines this accumulation is novae eruptions, which is included in the section after mass transfer. Finally the preliminary theory is rounded off by addressing magnetic braking and gravitational wave radiation. Both of which play an important role in these binaries when it comes to the evolution of their orbits. The latter section also includes the physics behind the gravitational wave radiation emitted from these tight circular binaries, and the detectability of them with respect to Laser Interferometer Space Antenna (LISA).

To asses our simulated systems, a chapter which present observational data is included. Here known AM CVns and evolved cataclysmic variables, which we use to compare with our simulations, are presented. Our simulations are made using Modules for Experiments in Stellar Astrophysics, `MESA`, version 24.08.1. The simulation specific settings is also presented in this chapter.

The thesis is then rounded off by showing our simulated results and the comparison to the observational data is the final chapter. We found that it is possible to reproduce known AM CVns and evolved cataclysmic variable systems, assuming this cataclysmic variables evolutionary channel. Furthermore, our simulated systems shows strong gravitational wave signals and most of them become detectable with LISA, once operational, with signals up to 300 times the sensitivity. The CARB magnetic braking model was found to have a strong impact on the evolution of these AM CVn systems. The initial parameter fine-tuning, which is a problem for weaker models, was resolved by using this stronger model, and we are able to find many AM CVn systems using different initial parameters. However, most was found to have an initial mass of around 1.25 $M_\odot$. This model was also found to have a strong impact in the AM CVn phase. It caused our simulated systems to yield higher mass transfer rates than that of the observational data in the AM CVn phase. Turning off magnetic braking for the compact donors yielded better results, however during so caused too low mass transfer rates. Thus another prescription is needed for compact donors in order to reproduce more observed systems.

List of Figures

Contents

Chapter 1

Introduction

Gravitational wave is a trending topic and has provided us with very exciting insight into fundamental physics. This has led to many initiatives, such as the Laser Interferometer Space Array (LISA) observatory, scheduled for launch in 2035, ESA (2025). LISA works in the 10^{-4} Hz to 1 Hz band. This places it in a band between ground based detectors, like the Laser Interferometer Gravitational-Wave Observatory (LIGO) which work in the band 10 Hz to 1 kHz band (Martynov et al., 2016), and the Pulsar Timing Array (PTA) working in the nHz band (Reardon et al., 2023). Thus, helping to bridge the gap in current gravitational wave astronomy. Compact white dwarf (WD) binaries can have very short orbital periods of the order of minuets to about an hour (Esposito et al., 2014; Ramsay et al., 2018). Thus, the gravitational wave frequencies emitted from these systems are in the range $f_{gw} \in [5.5, 55] \times 10^{-4}$ Hz, and LISA is therefore capable of detecting these systems, given that the strain amplitude of the wave exceeds the sensitivity of the detector.

A compact sub species of Cataclysmic variables (CVs) called AM CVns, named after the system AM Canum Venaticorum star, (Warner, 1995), are characterized by their short orbital periods ($P < 1$ hr) and hydrogen-deficient spectra. One evolutionary channel that these systems can be born from, is though the CV channel. Here a WD accretes material from a low mass donor star, that later during it evolution becomes a WD and potentially a compact binary which initiate mass transfer again. After the donor losses its hydrogen envelope, these compact binaries will then consist of a helium-rich and hydrogen-deficient donor and are classified as AM CVns.

Different accretion physics are relevant when considering CVs as they can have a huge influence on the response on the binary, and on how much mass the WD accumulates. Among these are the Roche-lobe radius, which is crucial for determining when mass transfer occurs. Another is the response of mass transfer, both for the binary and the donor; the former determines if the binary expands or tightens, and the latter determines if stable mass transfer can occur. Nova eruptions also become relevant because specific mass transfer rates are required for the WD accretor to grow. However, these are, of course, not the only effects that are very relevant when investigating the evolution of these systems. Without magnetic braking, many CV systems would not reach the small periods that they do (Hellier, 2001).

Magnetic braking is one of the main mechanism for loss of orbital angular momentum for binaries, which includes a low mass star. This therefore serves to tighten the initial orbital period and bring the system into a semi-detached phase from which the initial mass transfer is initiated. These systems need to be somewhat evolved before the initial mass transfer phase, in order to have enough helium in its core such that they have the potential of becoming AM CVns. Therefore, the strength of the magnetic braking prescription plays a crucial role.

There are several great advantages arising from studying AM CVns within the field gravitational wave astronomy. Known AM CVns can help calibrate future space-based gravitational wave missions, such as providing insight into the early universe (Amaro-Seoane et al., 2017), by serving as intergalactic

astrophysical beacons with known gravitational wave frequencies and strain amplitudes. Another advantage through this multi-messenger perspective is being able to further constrain system parameters, as the gravitational wave amplitude, received from these tight binaries, depends on orbital period, inclination angle, distance and the masses of the system. By combining gravitational wave measurements with electromagnetic observations, such as x-ray or optical, tighter constraints can be placed upon the systems physical properties, and ultimately lead to a more complete understanding of these binaries' structure and evolutionary state.

In this thesis Modules for Experiments in Stellar Astrophysics (MESA) are utilized, in order to evolve post-common envelope (CE) low mass binaries consisting of a zero age main sequence star (ZAMS) and a WD accretor. The initial parameter space of different masses and orbital periods is then constrained to identify systems which evolve into AM CVns, which can be compared with observational data.

The goals of this thesis is:

1. To confirm the viability of the CV evolutionary channel for AM CVn systems
2. Provide a detailed insight into the CV evolutionary channel for AM CVn system
3. Provide insight into the expected gravitational strain amplitudes of AM CVns and the detectability with respect to LISA
4. Investigate the influence of magnetic braking in the AM CVn phase

Chapter 2

Preliminary Theory

2.1 Cataclysmic Variables

To motivate the origin of these AM CVn systems, the evolution scenarios and properties of CVs are briefly elaborated, before moving on to the different formation channels of AM CVns.

CVs form from binaries with a low- or intermediate-mass, zero age main sequence (ZAMS) star $M < 10\ M_\odot$ and a lower mass star $M \sim 1\ M_\odot$ (Tauris and van den Heuvel, 2023; Hellier, 2001). The initially bigger star evolves on a shorter timescale, turning into a red giant before the low mass star. If the two stars are close enough it will fill its Roche lobe, transferring mass to the low mass star, which then accretes it. However, as this star is much bigger, the response of the mass transfer is for the orbital separation to decrease in order to preserve angular momentum, as the low mass star gains mass (see Section 2.2.2). This leads to unstable mass transfer, and eventually the low mass star is captured in the envelope of the donor star, leading to the common envelope (CE) phase. In this phase, the orbital period is substantially shortened and the envelope of the donor is expelled, leaving behind a WD.

2.1.1 Common Envelope

From a binary evolutionary perspective, if the white dwarf of a CV system is formed, interdependently from its companion, as the core of a supergiant, then the system must have had a fairly long orbital period. This is in order not to initiate mass transfer from the supergiant to its less evolved companion. Thus, a mechanism is needed which brings down the orbital period to the observed periods of around a couple of hours (Paczynski, 1976). CE evolution is a plausible explanation of how these low period CV systems are formed.

Investigating the CE phase is beyond the scope of this thesis, and is still an unsolved problem within astrophysics. However, since it is the current accepted model for CVs, see Ivanova et al. (2013), a brief explanation of the evolution will be presented here.

The term CE refers to a phase in which the stellar surface of a contact binary moves beyond the outer Lagrangian point (Paczynski, 1976), creating a binary which orbits inside a single shared envelope. Ivanova et al. (2013) breaks down the CE evolution into 5 distinct phases. The first phase, named *loss of corotation*, happens when the rotation of the expanding star goes from being most likely synchronized with the orbit, to it losing this coronation due to the binary starting to spiral inwards. The start of the inward spiral can happen due to runaway mass transfer, due to the accretors response to the mass transfer or due Darwin instability where orbital angular momentum is drained into spinning up a asynchronous donor (Ivanova et al., 2013). The second phase is the *Plunge-in* where orbital energy is transferred to the envelope, which then drives the expansion of it and may result in a direct envelope ejection, or a merger of both stars. The third is the *self-regulating* in-spiral which is followed by the subsequent termination of this phase. In this phase, the expansion of the envelope may cause the in-spiral of the binary to slow down. This can then form a self-regulating phase where frictional energy, released by the in-spiral, is transported

to the surface of the envelope where it is radiated away. This phase is then terminated by either ejection of the envelope or if either one of the cores fills its Roche lobe. It should be noted here that it is difficult to define the boundary between the core and the envelope. Moreover, the point which separates the ejected mass from the mass that stays behind is not clear in relation to this boundary (Ivanova et al., 2013), further obscuring CE evolution. The final phase is the *Post-CE* phase in which the final orbital properties settle, as these might be changed by the remaining circumbinary matter or winds from the remnant Ivanova et al. (2013).

A final note on CE evolution, is the undergoing struggle to reproduce this phenomenon, in simulations. This emphasizes the uncertainties still surrounding this theory. Simple models which only account for hydrodynamics and gravity often fail to eject the envelope. Including other envelope ejection effects, such as the thermalization of recombination energies, is dependent on the opacity in different regions, which is difficult to represent numerically (Schneider et al., 2025). Additionally, the cores are usually treated as a point mass. This further prevents realistic core-core interactions for the sake of computable 3D simulations (Schneider et al., 2025).

The resulting system of a WD and a low mass star will eventually start mass transfer as they get close enough for the low mass star to fill its Roche lobe, resulting in a CV. This scenario is depicted in Figure 2.2, as the first five steps. (Hellier, 2001)

2.1.2 Period Evolution in the CV Phase

The primary mechanism believed to pull the stars together is magnetic braking (MB) and gravitational wave radiation (GWR), which influence the orbital angular momentum of the binary, causing the orbit to shrink. There is also a contribution from the mass loss of the binary, if mass transfer is not conservative, along with spin-orbit coupling. Summarizing these four terms, the total change in orbital angular momentum can be stated as (Tauris and van den Heuvel, 2023)

$$\frac{\dot{J}_{orb}}{J_{orb}} = \frac{\dot{J}_{gwr}}{J_{orb}} + \frac{\dot{J}_{mb}}{J_{orb}} + \frac{\dot{J}_{ls}}{J_{orb}} + \frac{\dot{J}_{ml}}{J_{orb}}, \tag{2.1.1}$$

where $\dot{J}_{gwr}$ is the angular momentum loss from gravitational radiation, $\dot{J}_{mb}$ magnetic braking, $\dot{J}_{ls}$ spin-orbit coupling and $\dot{J}_{ml}$ from mass loss. Spin-orbit coupling will not be considered in this thesis, as they are initially synchronized as a consequence of the CE phase, when starting the simulations from the CV phase. The prescription for the other terms will be elaborated in Sections 2.2,2.4 and 2.5.

In order to investigate the evolution of CVs, it is advantageous to inspect the distribution of the measured orbital periods of the observed systems (see Figure 2.1).

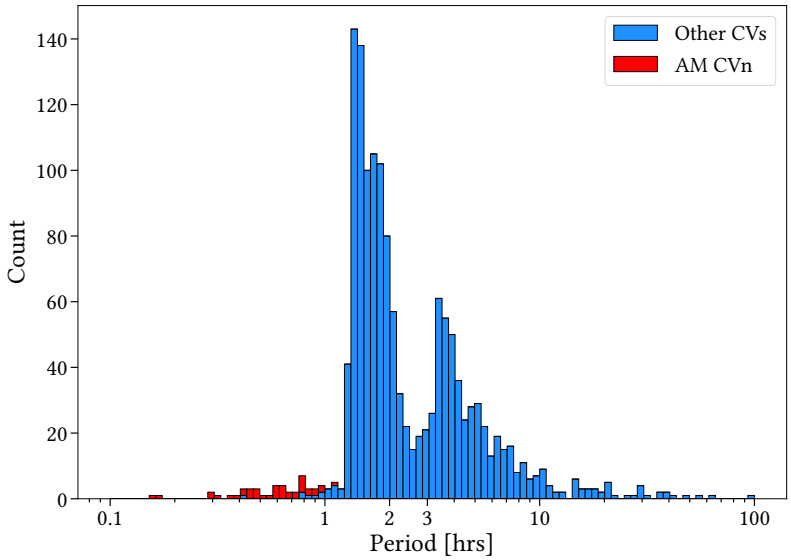

Figure 2.1: The distribution of measured orbital periods for observed cataclysmic binaries, data taken from Ritter and Kolb (2003).

It is believed that in CVs with orbital periods above ~3 hrs, MB is the dominant effect that decreases the period of the binary, as the stars are still too far apart for GWR to have a large effect. However, once the orbital period reaches this soft limit, the dynamo that caused MB seems to weaken and the binary system widens, due to mass transfer, giving the donor time to settle and causing it to shrink to a normal size, fitting of its mass (Knigge et al., 2011). This in turn causes mass transfer to stop, making the system undetectable. That is, until GWR pulls the stars together and the donor again fills its Roche lobe at a period of ~2 hrs, making the system detectable again. This is the reason for the period gab seen in Figure 2.1, between 3–2 hrs.

From this point the period will decrease in accordance with GWR until the period minimum is reached, and the orbit widens again. The reason this happens is that when the donor becomes degenerate it's response to mass loss is to expand. Therefore, as the orbit expands due to mass loss, so will the donor and it can continue to fill it's Roche lobe. Before, the orbit needed to shrink for the donor to keep filling its Roche lobe, as the two stars would otherwise be too far apart. Thus, the period bounces at this period minimum around 78 minutes.

However, looking at Figure 2.1, systems in the period gap and below this period minimum are still seen. Systems containing a magnetic WD can occupy the period gap, as its field couples to the the secondary's field, synchronizing the orbital period and spin period of the WD. CVs that first start mass transfer at these periods can also occupy this area, as the donor has not been driven out of hydrostatic equilibrium before reaching these periods. There are also systems which have periods below the period minimum, some of these contain a helium-rich donor that is more compact, and hence is able to reach lower periods. These systems are called AM CVns and will be investigated further throughout this thesis. Therefore, a detailed description of the different evolutionary scenarios will be given.

2.1.3 AM CVns

As stated previously, AM CVns, named after the first of their kind, the AM CVn, are CVs with a helium-rich donor.

Looking at Figure 2.2, we see the two evolutionary branches leading to AM CVns, following a CV

phase. One, where there is unstable mass transfer and the other, where there is stable. Unstable mass transfer leads to a CE phase where the envelope of the donor is expelled, and depending on whether the core reached degeneracy, a WD or helium star can emerge, this is the branch to the left in Figure 2.2. If the donor had a mass of $M_2 \leq 2.3\ M_\odot$ the core can become degenerate and a helium WD can be formed after the second CE phase leading to a double WD system. This system will then become an AM CVn once the period is sufficiently short and the donor comes into contact with the primary. However, if the donor has a mass $2.3\ M_\odot \leq M_2 \leq 5\ M_\odot$ it has enough mass to form a non-degenerate core, due to helium fusion, and can therefore form a helium star once the envelope is lost in the CE phase. This system can also end up as a double WD system, if the helium star becomes degenerate, although this is not depicted in Figure 2.2. Again, once the period is sufficiently short and mass transfer starts, an AM CVn is born.

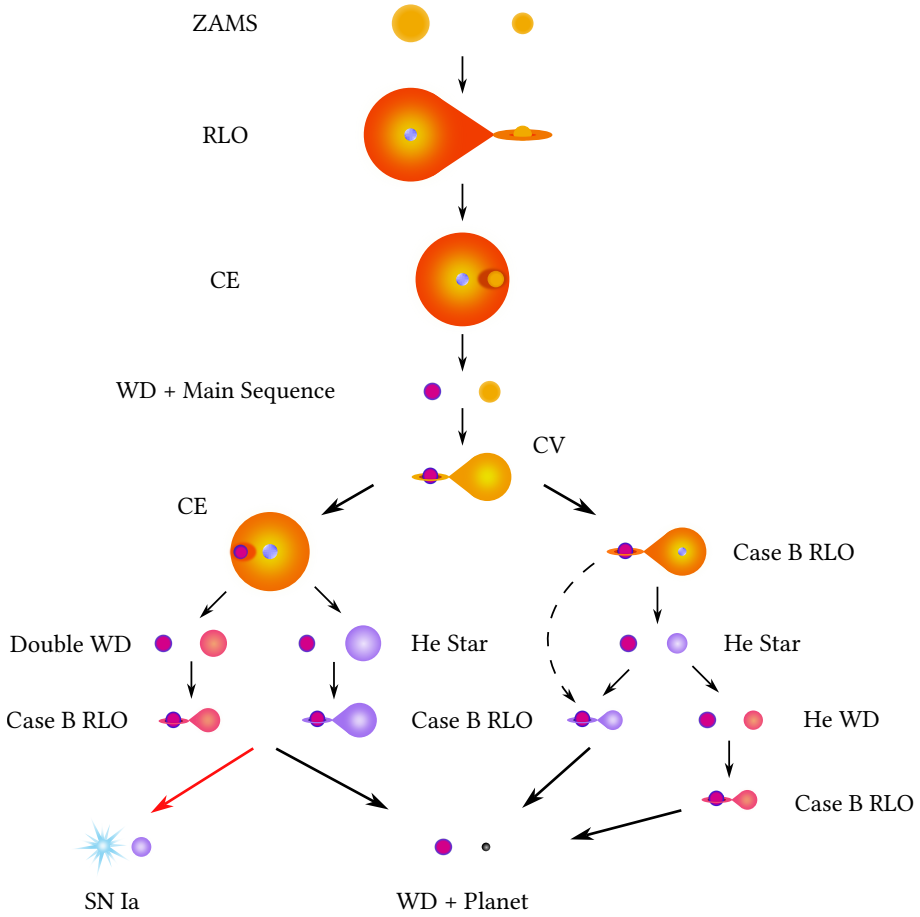

Figure 2.2: A schematic overview of the different formation channels of AM CVns (read the text for a detailed review).

In the branch to the right in Figure 2.2, no second CE phase takes place, but the end result is still an AM CVn. This happens for donors of $\sim 1\ M_\odot$, which are at the end of hydrogen core burning or have finished hydrogen core burning, before the onset of mass transfer. These systems can experience continuous mass transfer from the CV phase as the donor evolves, or there might be mass transfer followed by a detached phase before it continues again. Once the donor has been stripped of all its hydrogen, a helium star emerges, and if it becomes degenerate, a WD, creating an AM CVn. Solheim (2010)

The ultimate fates of these systems are either to end up in a type Ia supernova or for the donor to get stripped down to a planet-like object with very low mass, equivalent to that of Jupiter.

It is the systems of the right branch (see Figure 2.2), which are the focus of this thesis, they will be

simulated from just after the first CE phase and until a planet-like object is left or a Hubble time is reached.

Mass transfer will now be investigated in greater detail in order to give an overview of the relevant criteria and mechanics.

2.2 Mass Transfer in CVs

As is evident from the previous section, mass transfer plays a crucial role in the evolution of CVs, determining when they are visible and how the period evolves. Therefore, a brief overview of the relevant physics and most important consequences will be given.

Roche-lobe mass transfer occurs when the gravitational pull acting on the material of a star is greater from another star rather than the star itself. In this case, the material from the donor experiences a greater pull from the WD, rather than the donor star. To examine this, the Roche-lobe approximation is used to determine when mass transfer is possible. It is useful to use the equipotential equation, where the total effective potential is set equal to a constant (Livio, 1994)

$$-\frac{GM_1}{(x^2+y^2+z^2)^{1/2}} - \frac{GM_2}{((x-a)^2+y^2+z^2)^{1/2}} - \frac{1}{2}\Omega_B^2\left[\left(x-\frac{M_2}{M_1+M_2}a\right)^2+y^2\right] = \text{const}, \tag{2.2.1}$$

where M_1, M_2 are the masses of the WD and star, respectively, and Ω_B is the angular velocity of the binary,

$$\Omega_B = \left(\frac{G(M_1+M_2)}{a^3}\right)^{1/2}.$$

The reference frame used in this equation is a co-rotating one, meaning that the coordinate system rotates with the binary. This is valid because the two stars are tidally locked, following the CE phase. Furthermore, the origin is set to be at the WD, so that the two stars lie along the x-axis and the rotation axis is along the z-axis. A depiction of different equipotentials can be seen in Figure 2.3 following different constant values of (2.2.1), corresponding to the different Lagrange points.

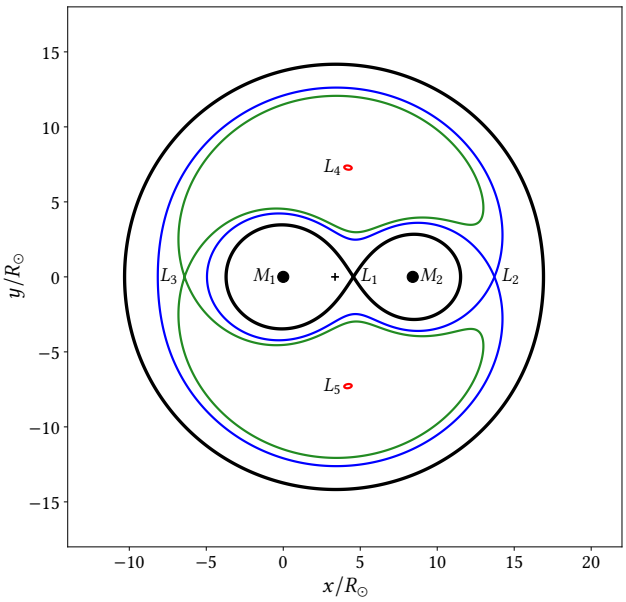

Figure 2.3: The different equipotentials corresponding to Lagrange points 1–5, for a binary with masses $M_1 = 0.8\ \mathrm{M}_\odot$, $M_2 = 1.2\ \mathrm{M}_\odot$ and a orbital period of $P = 2$ days corresponding to $a = 8.4\ \mathrm{R}_\odot$.

When considering mass transfer, Lagrange point one, L_1, is often the first thing that comes to mind, as it is the point where mass starts to fall from the donor to the primary. It can be seen in Figure 2.3 as the point where the two "pear" shapes meet, which is the Roche-lobes of the two stars.

If this radius exceeds its Roche lobe, then the mass outside the Roche lobe is more drawn toward the other star, and mass transfer is initiated. It is therefore of interest to be able to calculate when this volume is filled. This is done by calculating the radius of a sphere of the same volume, which, using previously tabulated data, Peter P. Eggleton made a convenient approximation for. This is given in Eggleton (1983) as,

$$R_L = a\frac{0.49q^{2/3}}{0.6q^{2/3} + \ln(1 + q^{1/3})}, \tag{2.2.2}$$

where $q \equiv M_{\text{donor}}/M_{\text{accretor}}$ and R_L is the radius of the donor star's Roche lobe given the orbital separation a.

The mass transferring from the donor onto the WD can be seen as going through a nozzle at L_1,

$$|\dot{M}_2| \simeq \rho v_s Q, \tag{2.2.3}$$

with ρ being the density of the material, v_s the local sounds speed and Q the effective cross section.

Following the Roche-lobe approximation, mass transfer starts once the star is filling its Roche-lobe, $R_2 > R_L$, so that it keeps a radius equal to its Roche-lobe. However, as stars do not have sharply defined edges this ends up being a rough approximation as one would expect a more gradual increase in mass transfer once the star starts to fill it's Roche-lobe. This can be helped by taking the scale height of the stellar atmosphere into consideration. The atmosphere of a star starts at the photosphere, where it becomes transparent, and is often the point at which the radius of the star is defined. In this atmosphere there is still material, but the density decreases exponentially, such that

$$\rho(R_L) = \rho_{ph}\mathrm{e}^{-(R_L - R_2)/H}, \tag{2.2.4}$$

where ρ_{ph} is the density of the photosphere and H is the scale height. (Tauris and van den Heuvel, 2023)

Combining these two interpretations, the mass transfer scheme of Ritter (1988) can be defined. The mass transfer rate is

$$|\dot{M}_2| = \frac{1}{\sqrt{\mathrm{e}}}\rho_{ph} v_s Q \mathrm{e}^{-\Delta R/H_p}, \tag{2.2.5}$$

where $v_s = \sqrt{kT/(\mu m_H)}$ and $\Delta R \equiv R_L - R_2$. The scale height of the stellar atmosphere is

$$H_p = \frac{kTR_2^2}{\mu m_H G M_2}, \tag{2.2.6}$$

where k is the gas constant, T the temperature, μ is the mean molecular weight of the photosphere and m_H is the weight of a hydrogen atom. This scheme was developed considering low mass main sequence stars where $H_p \ll R_2$ and $\Delta R/R_2 \ll 1$.

Now, the mass transfer rate scales with H_p and the difference between the stars radius and its Roche-lobe, making the transition smoother.

It it also important to determine when stable mass transfer occurs, this depends heavily on the donors stars response to mass loss, and has great influence on the evolution of the CV.

2.2.1 Stability Criteria

When the donor star loses mass it is perturbed out of hydrostatic equilibrium. It then settles into a new one following two time scales, the dynamical τ_{dyn} and the thermal τ_{th}, also called the Kevin-Helmholtz

timescale. It does this by expanding or contracting. However, as the star losses mass the Roche-lobe radius also changes, if the star keeps filling its Roche-lobe, mass transfer is stable and continues following the thermal timescale. Otherwise, it is said to be unstable and follows the dynamical timescale. (Tauris and van den Heuvel, 2023)

A stability criteria can be defined using the power law

$$R \sim M^{\zeta}, \tag{2.2.7}$$

which estimates the radius of a star given its mass. For a normal main sequence star $\zeta = 0.8$. Thus for the radius of the donor star and its Roche-lobe the exponents become,

$$\zeta_{donor} \equiv \frac{\partial \ln R_2}{\partial \ln M_2}, \quad \zeta_L \equiv \frac{\partial \ln R_L}{\partial \ln M_2}. \tag{2.2.8}$$

To start mass transfer $R_2 = R_L$ within the binary, and thus the criteria

$$\zeta_L \leq \zeta_{donor} \tag{2.2.9}$$

is reached. This states the same as above, as long as the star keeps filling its Roche-lobe following mass loss, mass transfer has the potential to be stable. However, this statement must be evaluated in terms of the response of the binary and the donor. If the radius of the donor or orbit expands or shrinks to fast, respectively, dynamically unstable mass transfer can ensue.

2.2.2 System Response to Mass Loss

To investigate the binaries' response to mass loss, the isotropic re-emission model is considered. In this model matter flows from the donor onto the accretor before a fraction of it is ejected, this fraction is denoted β, so that

$$\dot{M}_1 = -(1-\beta)\dot{M}_2. \tag{2.2.10}$$

For simplicity and for the sake of investigating the effects of mass loss the angular momentum losses $\dot{J}_{mb} = \dot{J}_{gwr} = \dot{J}_{ls} = 0$ and

$$\frac{\dot{J}_{ml}}{J_{orb}} = \frac{\beta q^2}{1+q} \times \frac{\dot{M}_2}{M_2}. \tag{2.2.11}$$

The material is ejected with the specific angular momentum of the accretor, such that

$$\mathrm{d}J_{orb} = \frac{J_1}{M_1}\beta \mathrm{d}M_2, \tag{2.2.12}$$

with $J_1 = (M_2/M)J_{orb}$ (Tauris and van den Heuvel, 2023). Following these assumptions the following relation can be obtained from the general equation for orbital changes due to mass transfer and mass loss in a binary (Tauris and van den Heuvel, 2023),

$$\frac{a}{a_0} = \left(\frac{q_0(1-\beta)+1}{q(1-\beta)+1}\right)^{\frac{3\beta-5}{1-\beta}} \left(\frac{q_0+1}{q+1}\right)\left(\frac{q_0}{q}\right)^2. \tag{2.2.13}$$

Now an analytical expression, which includes the orbits response, can be derived for ζ_L by expanding (2.2.8)

$$\zeta_L = \frac{\partial \ln R_L}{\partial \ln M_2} = \left(\frac{\partial \ln a}{\partial \ln q} + \frac{\partial \ln(R_L/a)}{\partial \ln q}\right)\frac{\partial \ln q}{\partial \ln M_2}. \tag{2.2.14}$$

Using (2.2.2), (2.2.10) and (2.2.13) can give a final expression.

It is useful to investigate the first term of (2.2.14) to get an idea of how the orbital separation responds to mass loss, in terms of the mass ratio of the two stars in the binary,

$$-\frac{\partial \ln a}{\partial \ln q} = 2 + q\frac{q}{q+1} + q\frac{3\beta - 5}{q(1-\beta)+1}. \tag{2.2.15}$$

Plotting this equation for different values of β yields the tracks in Figure 2.4.

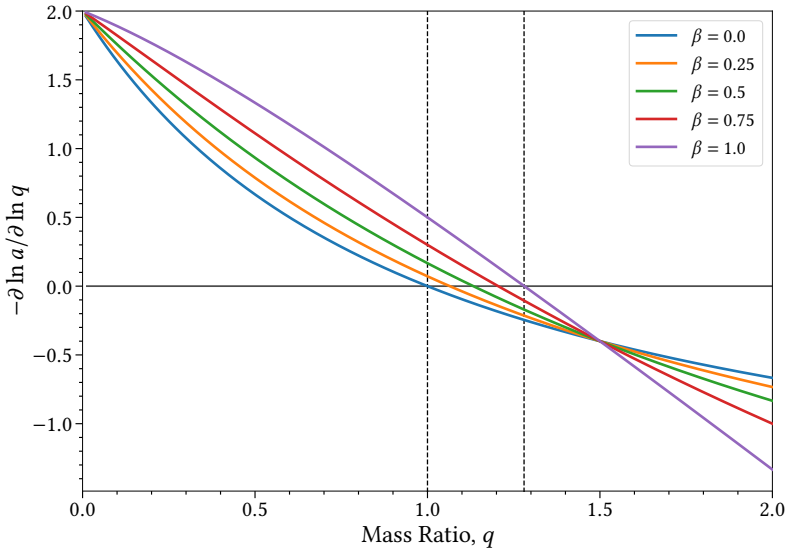

Figure 2.4: The binary separations response to mass loss in terms of the mass ratio, q. Tracks corresponding to different values of β have been plotted.

Here it seen that if the accretor is more massive than the donor, $q \leq 1$, then the orbit widens as a response to mass loss. It becomes more difficult for the opposite case where $q > 1$. For $1 < q < 1.28$ it depends on β, whereas for $q > 1.28$ it always shrinks. Thus, different limits for the response of mass loss exists for the binary separation and, as can be seen in (2.2.2), this influences the Roche-lobe radius and in turn helps determine whether there is stable mass transfer. How the donor responds becomes very relevant considering the stability criteria, as the star must keep filling its Roche-lobe. This response depends on the structure of the donor. If the donor has a radiative envelope, its radius tends to shrink, whereas if it has a convective envelope it expands. (Tauris and van den Heuvel, 2023)

For a donor star with radiative envelope, dynamically stable mass transfer is often possible, as long as q is not too large, as its radius will shrink or stay roughly the same. However, for stars with deep convective envelopes, the response of mass loss is for the star to rapidly expand, thus the mass ratio must be small for stable mass transfer to occur. If the orbit does not widen according to this expansion, this can lead to the formation of a CE.Tauris and van den Heuvel (2023)

Of course, other effects also play a crucial role in the evolution of these systems, and only considering the effect of mass loss is a simplified example. These effects include MB, GWR and stellar winds from the donor star. However, in terms of the mass loss response, this helps to give insight into the consequences of mass loss during mass transfer.

In terms of mass transfer rates, these are proportional to how much the donor overfills its Roche-lobe as seen in (2.2.5). However, an upper limit at the Eddington luminosity can be reached, which is essential when considering high mass transfer rates. Therefore, this will be briefly elaborated.

2.2.3 Eddington Accretion Limit

The Eddington accretion limit is a fundamental property when considering binary stellar evolution for compact objects. It determines how much material a compact object can accumulate during mass transfer, as once a critical luminosity called the Eddington luminosity, L_{Edd}, is reached, further accretion is hindered due to the outward radiation pressure. In this section, the aim is to derive an expression for which the Eddington accretion limit can be calculated for a WD, depending on its mass and the material which is accreted. This limit is given by equating the outward radiation pressure force on the plasma near the stellar surface of the WD to the gravitational force (Tauris and van den Heuvel, 2023), such that

$$\left|\vec{F}_{rad}\right| = \left|\vec{F}_{grav}\right| \tag{2.2.16}$$

$$\frac{L_{edd}\sigma_T}{4\pi r^2 c} = \frac{GM_1 m_p \mu_e}{r^2}, \tag{2.2.17}$$

where $\mu_e \simeq 2/(1+X)$ is the mean molecular weight per electron and σ_T is the Thompson scattering cross section, given by

$$\sigma_T = \frac{8\pi}{3}\left(\frac{e^2}{m_e c^2}\right)^2 \text{cm}^2. \tag{2.2.18}$$

Introducing the mean opacity and using the previous equation, gives

$$\kappa = \frac{\sigma_T}{m_p \mu_e} \simeq 0.2(1+X)\text{cm}^2\text{g}^{-1}. \tag{2.2.19}$$

Now returning to (2.2.17) and using the mean opacity, one obtains an expression for the Eddington luminosity

$$L_{Edd} = \frac{4\pi G M_1 c}{\kappa} \simeq \frac{4\pi G M_1 c}{0.2(1+X)}. \tag{2.2.20}$$

Furthermore, the accretion luminosity can be started to be

$$L = \epsilon \dot{M}_1, \quad \epsilon = \epsilon_{nuc} + \epsilon_{grav}, \tag{2.2.21}$$

where ϵ is the energy production per unit mass, which is the result from the energy released by fusion of the accreted material, ϵ_{nuc}, and gravitational energy, ϵ_{grav}. Thus, the Eddington accretion limit is found to be

$$\dot{M}_{edd} = \frac{4\pi G M_1 c}{\kappa \epsilon} \simeq \frac{4\pi G M_1 c}{0.2(1+X)\epsilon}. \tag{2.2.22}$$

For WDs, the main contribution to the accretion luminosity comes from ϵ_{nuc}, which has the following value for hydrogen $\epsilon_{nuc} \sim 6.4 \times 10^{18}$ erg g^{-1} and for helium $\epsilon_{nuc} \sim 7.5 \times 10^{17}$ erg g^{-1} (Tauris and van den Heuvel, 2023). However, a small contribution also stems from the release of gravitational energy, which is given by (Tauris and van den Heuvel, 2023)

$$\epsilon_{grav} = \frac{GM_1}{R_1}. \tag{2.2.23}$$

This leads to some issues, as the radius of the WD is not considered in the simulations because it is assumed to be a point mass. Therefore, an estimate is used from Nauenberg (1972), which takes in the mean molecular weight of the WD, μ, and the mass of the WD

$$R_1 = \frac{0.0225}{\mu}\left(\left[\frac{1.4\ \text{M}_\odot}{M_1}\right]^{2/3} - \left[\frac{M_1}{1.4\ \text{M}_\odot}\right]^{2/3}\right)^{1/2} \text{R}_\odot. \tag{2.2.24}$$

Here $\mu = 2$, which is the mean molecular weight per electron, assuming that the atomic number and the atomic mass number are $Z/A \approx 0.5$ and $m_u = m_B = 1.66 \times 10^{-24}$ g. (Shapiro and Teukolsky, 1983).

Thus an expression for the Eddington accretion limit has been found which depends only on the mass of the WD and the composition of the accreted material. One just need to use the appropriate ϵ_{nuc}, once the material becomes sufficiently helium-rich.

Nova eruption may also occur throughout the evolution of these systems, and different criteria apply when the WD accretes hydrogen-rich or helium-rich material. Therefore, to model the evolution of these systems, this must be investigated to determine when the WD accumulates material.

2.3 Novae Eruptions

CVs are known for their sudden brightness changes, which are caused by novae eruptions. There exist different subcategories, which are classical novae, recurrent novae, and dwarf novae.

The classical novae occur when the WD primary accretes material at a rate where stable fusion is not feasible, which leads to a build-up until a runaway fusion process happens as the envelope of accreted material becomes hot enough. As a result, some or all of the envelope is expelled in a shell flash, depending on the strength, which is mainly linked to the accretion rate. Classical novae only erupt once, whereas recurrent novae do this periodically, usually every few decades, as the WD builds up material.

Dwarf novae, on the other hand, are the result of pile-up in the accretion disc, which happens due to a high mass transfer rate. The disk then flares up, expelling excess material, where some of it falls upon the WD, briefly increasing the accretion rate, causing an increase in luminosity. This increase in luminosity occurs over a couple of days, where-after the CV stays bright for roughly a week before declining. These outbursts often repeat after a few months. (Hellier, 2001)

The recurrent novae eruptions will be relevant in this thesis as they will determine whether the WD accretor is able to accumulate material or whether it will be lost. Therefore, the different accretion rate limits are investigated in order to determine when material is accumulated. Depending on the material that is being accreted, these limits can vary substantially, and this is important when AM CVns evolve. The goal in this thesis is to exhaust the donor of its hydrogen through accretion such that it becomes helium-rich, creating an AM CVn. However, this means that, throughout the evolution of these binaries, both hydrogen and helium can be accreted at different times, changing the limits for stable burning of material and how much material is accumulated on the WD primary. Thus, a prescription following Tauris et al. (2013) is adopted, where accretion of both hydrogen-rich and helium-rich material is accounted for.

2.3.1 Hydrogen Accumulation Efficiency

The objective is to define two accumulation efficiencies, one for hydrogen and one for helium η_H, η_{He}, which determines how much material is accumulated, in a continuous manner throughout the simulations. To determine what these efficiencies are, different ranges of mass transfer rates have to be considered depending on the hydrogen mass fraction of the accreted material and the WD mass. For hydrogen, the following limits are used to specify η_H:

- $\dot{M}_{cr}$, the upper limit of stable hydrogen burning,
- $\dot{M}_{edd}$, Eddington accretion limit,

- $\dot{M}_{st}$, lower limit for stable hydrogen burning,
- $\dot{M}_{accu}$, the lower limit at which the WD can still accumulate material.

Only above $\dot{M}_{accu}$ does the WD accumulate material, and unless the mass transfer rate is higher than $\dot{M}_{edd}$ or $\dot{M}_{cr}$, conservative mass transfer occurs. However, if the mass transfer rate is higher than these limits, the accumulation rate is limited to that of $\dot{M}_{edd}$ or $\dot{M}_{cr}$, depending on which is lower. The rest of the mass, which the WD receives, is lost due to winds (Hachisu and Kato, 2001). How the Eddington accretion limit is calculated has already been presented in Section 2.2.3. The other limits are calculated following (Hachisu and Kato, 2001; Hachisu et al., 1999) where

$$\dot{M}_{cr} = 5.3 \times 10^{-7} \frac{1.7 - X}{X} \left(\frac{M_1}{\mathrm{M}_\odot} - 0.4 \right) \mathrm{M}_\odot \mathrm{yr}^{-1}, \tag{2.3.1}$$

where X is the hydrogen abundance of the accreted material. From this the mass transfer rate at which stable hydrogen fusion occurs can be estimated to be $\dot{M}_{st} \approx 1/2\dot{M}_{cr}$. Below this limit weak novae flashes start to occur, where some material might be lost. However, following Hachisu et al. (1999) the WD is assumed to retain all material until it reaches

$$\dot{M}_{accu} = \frac{1}{8}\dot{M}_{cr}. \tag{2.3.2}$$

This might overestimate how much material the WD accumulates, but there is still a great deal of uncertainty surrounding the accumulation efficiency during these weak flashes. Therefore, the accumulation efficiency is set to $\eta_H = 1$ is for mass transfer rates between $\dot{M}_{cr}$ and $\dot{M}_{accu}$. Above $\dot{M}_{cr}$ it is set to be $\eta_H = \dot{M}_{cr}/|\dot{M}_2|$, with $\dot{M}_2$ being the mass transfer rate. Below $\dot{M}_{accu}$ the accumulation efficiency is set to $\eta_H = 0$, as all the material is lost in nova eruptions.

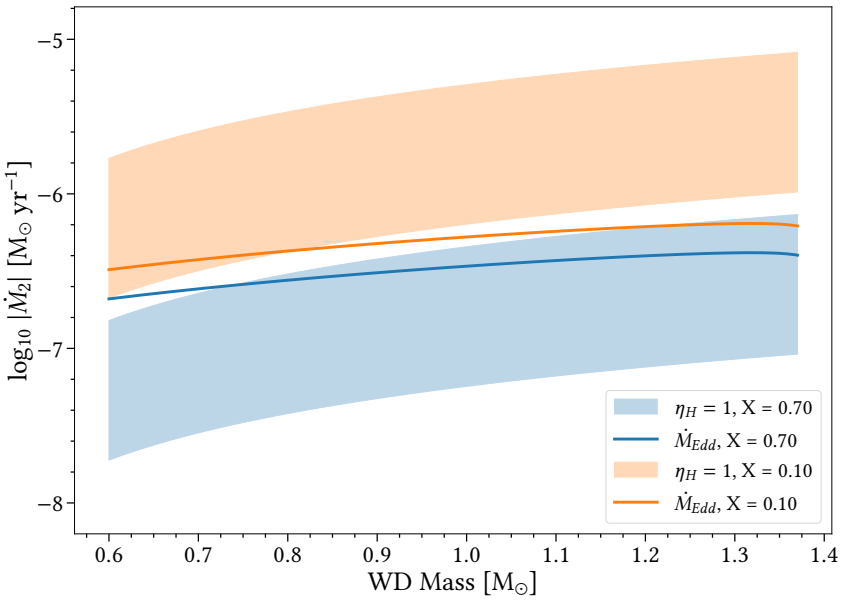

Figure 2.5: Mass transfer ranges where $\eta_H = 1$, for different WD masses and hydrogen abundances, X, of the accreted material. The Eddington accretion limits for the two abundances is also shown.

In Figure 2.5 areas for which $\eta_H = 1$ for $X = 0.70, 0.10$ is shown along with the Eddington accretion limits. A general tendency arises for lower values of X, where higher mass transfer rates are required for the WD to accumulate material through hydrogen fusion. However, the Eddington accretion limit does

not increase as fast for lower values of X. This does not mean that material is not accumulated for higher WD masses, but that wind mass loss is more significant.

These limits are not applicable for very low $X \sim 10^{-4}$, when the accretion material is almost purely helium, hence different limits must be defined to determine η_{He}.

2.3.2 Helium Accumulation Efficiency

For helium accretion the limits has been defined by Kato and Hachisu (1999, 2004). It is a more step-wise procedure as they have calculated the accretion efficiency for the specific WD masses: $[0.7, 0.8, 0.9, 1.0, 1.1, 1.2, 1.3, 1.35]$ $M_\odot$. Thus, the value of the accumulation efficiencies in between some of these masses are stepwise interpolated, such that different ranges could be defined in order to calculate η_{He}. The mass transfer ranges for the different WD masses and values for the accumulation efficiency can be seen in Table 2.1 below.

Mass Ranges $[M_\odot]$	**Mass Accumulation Efficiency**, η_{He}	**Accretion Rates** $[\log M_\odot \mathrm{yr}^{-1}]$
$M_1 < 0.8$	1	–
$0.8 \leq M_1 < 0.9$	1 $-0.35(\log \dot{M}_2 + 6.1)^2 + 1.02$	$-6.34 \leq \log \dot{M}_2$ $-6.5 < \log \dot{M}_2 < -6.34$
$0.9 \leq M_1 < 1.0$	1 $-0.35(\log \dot{M}_2 + 5.6)^2 + 1.07$	$-6.05 \leq \log \dot{M}_2$ $-6.88 < \log \dot{M}_2 < -6.05$
$1.0 \leq M_1 < 1.2$	1 $-0.35(\log \dot{M}_2 + 5.6)^2 + 1.01$	$-5.93 \leq \log \dot{M}_2$ $-6.92 < \log \dot{M}_2 < -5.93$
$1.2 \leq M_1 < 1.3$	1 $-0.54(\log \dot{M}_2 + 5.6)^2 + 1.01$ $0.54 \log \dot{M}_2 + 4.16$	$-5.76 \leq \log \dot{M}_2$ $-5.95 \leq \log \dot{M}_2 < -5.76$ $-7.06 < \log \dot{M}_2 < -5.95$
$1.3 \leq M_1 < 1.35$	1 $-0.175(\log \dot{M}_2 + 5.35)^2 + 1.03$	$-5.83 \leq \log \dot{M}_2$ $-7.35 < \log \dot{M}_2 < -5.83$
$1.35 \leq M_1$	1 $-0.115(\log \dot{M}_2 + 5.7)^2 + 1.01$	$-6.05 \leq \log \dot{M}_2$ $-7.4 < \log \dot{M}_2 < -6.05$

Table 2.1: Mass accumulation efficiencies for given WD masses and accretion rates. Taken from Kato and Hachisu (2004).

For WD masses $M_1 < 0.8$ $M_\odot$ all material is accumulated, only limited by the Eddington accretion limit, as no winds blow from the WD. However, once the WD has mass greater than this, winds start to blow and a lower limit for the mass transfer rate must be reached. This lover limit where $\eta_{He} > 0$ decreases as the mass becomes larger. This is because as the WD becomes larger, the nuclear burning rates become higher as a result of gravity, so it can accumulate mass at lower mass transfer rates. The limit where $\eta_{He} = 1$ first increases and then peaks for masses $1.2 \leq M_1 < 1.3$ $M_\odot$ before dropping again. This is because the winds also become stronger as the WD mass is increased, and for WD masses which are substantially high, the nuclear burning rates are stronger than those of the wind mass loss.

These limits have also been plotted in Figure 2.6, where the piecewise definitions for the WD mass ranges are apparent. The Eddington accretion limits are higher owing to the decrease in energy obtained from fusing helium instead of hydrogen (see Section 2.2.3).

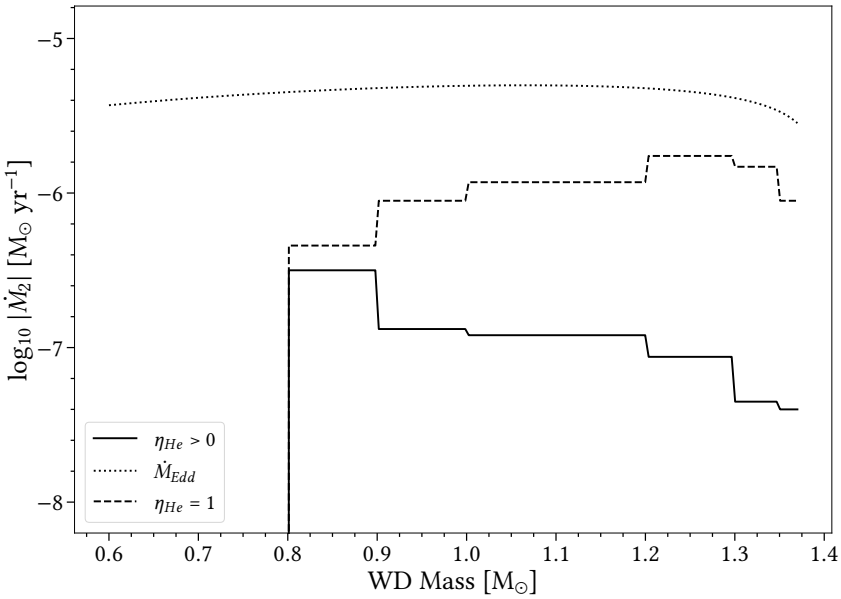

Figure 2.6: Mass transfer ranges where $\eta_{He} > 0$ and $\eta_{He} = 1$, for different WD masses. The Eddington accretion limits for helium-rich material is also shown.

It should be mentioned that the accumulation efficiency is highly sensitive to the composition and radius of the WD. As the WD fuse helium in the envelope, carbon and oxygen is mixed throughout it via convection. If the $C + O$ abundance in the envelope, for a 1.2 $M_\odot$ CO WD, is increased from 0.3 to 0.4, the accumulation efficiency, η_{He}, increases by 0.04–0.05. Furthermore, if smaller WD radii are assumed, η_{He} drops because the winds become stronger (Kato and Hachisu, 2004). However, these considerations are well beyond the scope of this thesis, but should be kept in mind when using these limits and accumulation efficiencies.

Now an expression for the long terms mass accumulation onto the WD can be defined as

$$\dot{M}_1 = \eta_H \eta_{He} |\dot{M}_2|. \tag{2.3.3}$$

Depending on which type of accretion occurs, either η_H or η_{He} is set to equal one, such that the appropriate accumulation efficiency is used. Helium accretion is assumed if $X < 10^{-4}$, where $\eta_H = 1$, if $X > 10^{-4}$ hydrogen accretion is assumed and $\eta_{He} = 1$.

Now that a framework of relevant theory for mass transfer and the binaries response to it has been presented, other effects which also affect the orbit will be elaborated. The following two sections will investigate the orbital angular momentum loss due to MB and GWR.

2.4 Magnetic Braking

Low mass main sequence stars, of mass $\leq 1.3\ M_\odot$, burn hydrogen in a central radiative region in the ZAMS phases. The outer regions are convective due to the presence of partially ionized hydrogen and helium making these regions opaque (Salaris and Cassisi, 2005). In higher mass stars the interior temperature increases allowing the CNO cycle to operate as the favorable burning reaction, becoming the dominant mechanism for energy production. This results in high energy concentration towards the center, causing the star to become convective (Salaris and Cassisi, 2005). This difference between lower mass and higher

mass stars is important when it comes to magnetic field generation in stars, which ultimately can lead to magnetic braking.

Within the outer convective zones of stars turbulent and helical down-flow of ionized material, shaped by the Coriolis force, regenerate and amplify the persistent large scale poloidal magnetic field. In stars with a radiative inner region another amplification mechanism exists. The radiative zone rotates uniformly compared to the convective zone, which experiences differential rotation. The shear between the uniformly rotating radiative zone and the differentially rotating convective zone twists and converts the field into a strong toroidal field at this shear line, at the equator (Miesch, 2005). As this toroidal field becomes stronger it eventually become unstable and can rise towards the surface as flux tubes. If the field become strong enough, these may rise to the surface and couple to the large scale poloidal field and amplify it (Miesch, 2005). This mechanism effectively converts rotational shear into magnetic energy. Thus the presence of this interface between a radiative and a convective zone, also called the tachocline, is important when it comes to strong, large scale and long term magnetic field generation in stars.

Material coupled to this magnetic field, which is lost from the binary in a wind, creates a torque called magnetic braking. The star losses spin angular momentum due to this torque, which is then restored though tidal friction at the cost of orbital angular momentum. This finally causes the orbital separation to decrease, further tightening the binary. It is therefore an important mechanism to consider in the creation of these compact binaries. In this thesis the convection and rotation boosted (CARB) magnetic braking model is used, however some comparisons to the Skumanich model will be made as its simplicity make it a widely used model in the literature.

2.4.1 CARB Magnetic Braking Model

In Van and Ivanova (2019a), which is the article behind the CARB magnetic braking model, the angular momentum loss due to mass loss at the Alfvén radius is given by,

$$\dot{J}_{mb} = -\frac{2}{3}\dot{M}_w \Omega r_a^2, \tag{2.4.1}$$

as derived by Weber and Davis (1967) for the Sun, under the assumption of spherical symmetry and isotropic wind mass loss. Here $\dot{M}_w$ is the wind mass loss, Ω is the rotation rate and r_a is the Alfvén radius. The radial Alfvénic Mach number, M_A, as defined by Weber and Davis (1967), is given by,

$$M_A^2 = \frac{4\pi\rho u^2}{B_r^2} \tag{2.4.2}$$

where ρ and u is the density and radial velocity component of the wind respectively. This per definition equates to one at the Alfvén radius. B_r is the radial component of the magnetic field strength, however assuming a simple radial magnetic field relation as done by Van and Ivanova (2019a) the magnetic field can be rewritten to $B_r = B_s R^2/r^2$, where B_s is the surface field strength and R is the radius of the star. Evaluating (2.4.2) at the Alfvén radius, and inserting the radial field strength, it rewrites to,

$$\left(\frac{r_a}{R}\right)^2 = \frac{B_s^2 R^2}{4\pi r_a^2 \rho_a u_a^2}. \tag{2.4.3}$$

Here ρ_a and u_a is the density and radial velocity of the wind at the Alfvén surface. Assuming spherical symmetry the Alfvén surface area can be written as $4\pi r_a^2$, and thus the total wind mass loss though the Alfvén surface is $\dot{M}_w = 4\pi r_a^2 \rho_a u_a$, reducing (2.4.3) to

$$\left(\frac{r_a}{R}\right)^2 = \frac{B_s^2 R^2}{\dot{M}_w u_a}. \tag{2.4.4}$$

The alfvén velocity can be written in terms of the surface escape velocity, $v_{esc} \equiv \sqrt{2GM/R}$, by considering energy conservation for a particle which escape the gravitational well,

$$\frac{1}{2}u_a^2 - \frac{GM}{r_a} = 0 \Rightarrow u_a = v_{esc}\left(\frac{R}{r_a}\right)^{1/2}. \tag{2.4.5}$$

In Van and Ivanova (2019a) it is then argued that rotation can have a non-negligible effect on the stellar wind, and thus needs to be included, based on the work of Matt et al. (2012). Based on the same work Réville et al. (2015) introduced a modified velocity which when relapsed with v_{esc} include this effect, and is thus used in the CARB model. Here this modified velocity, as presented in the appendix of Réville et al. (2015), is

$$v_{mod}^2 = v_{esc}^2 + \frac{2\Omega^2 R^2}{K_2^2}, \tag{2.4.6}$$

where $K_2 = 0.07$ is a constant found by Réville et al. (2015). Inserting (2.4.6) instead of v_{esc} into (2.4.4), squaring both sides and then replacing v_{esc} with v_{mod} yields,

$$\left(\frac{r_a}{R}\right)^3 = \frac{B_s^4 R^4}{\dot{M}_w^2 v_{esc}^2} \Rightarrow \left(\frac{r_a}{R}\right)^3 = \frac{B_s^4 R^4}{\dot{M}_w^2}\frac{1}{v_{esc}^2 + 2\Omega^2 R^2/K_2^2}. \tag{2.4.7}$$

This effectively augments the Alfvén radius to be smaller for faster spinning stars and in turn for tighter binaries which are tidally coupled, thus reducing the effect of magnetic braking. The final assumption adopted in the CARB model is the approximation that $B_s \propto \Omega\tau$, where τ is the convective turnover time. This can then be used to create a scaling relation based on estimated solar parameters such that,

$$B_s = B_{s,\odot}\frac{\Omega}{\Omega_\odot}\frac{\tau}{\tau_\odot}, \tag{2.4.8}$$

Where τ is calculated using the following integral,

$$\tau = \int_{r_b}^{R}\frac{1}{v_{conv}}\mathrm{d}r. \tag{2.4.9}$$

Here r_b is the bottom of the convective envelope and v_{conv} is the local convective velocity. Practically, this integral is evaluated numerically by summing over the mesh zone in `MESA` that satisfy the Schwarzschild criterion for convection on the form,

$$\left|\frac{\mathrm{d}\ln T}{\mathrm{d}\ln P}\right|_{ad} < \left|\frac{\mathrm{d}\ln T}{\mathrm{d}\ln P}\right|_{rad}, \tag{2.4.10}$$

and making sure that the zone is the envelope, by checking to see if the specific nuclear energy generation rate is less than 0.01 erg g^{-1} s^{-1}.

Inserting (2.4.8) into (2.4.7) then yields,

$$\left(\frac{r_a}{R}\right)^3 = \frac{R^4}{\dot{M}_w^2}\frac{1}{v_{esc}^2 + 2\Omega^2 R^2/K_2^2}B_{s,\odot}^4\left(\frac{\Omega}{\Omega_\odot}\right)^4\left(\frac{\tau}{\tau_\odot}\right)^4 \Rightarrow \tag{2.4.11}$$

$$r_a^2 = \frac{R^{14/3}}{\dot{M}_w^{4/3}}\left(v_{esc}^2 + 2\Omega^2 R^2/K_2^2\right)^{-2/3}B_{s,\odot}^{8/3}\left(\frac{\Omega}{\Omega_\odot}\right)^{8/3}\left(\frac{\tau}{\tau_\odot}\right)^{8/3}. \tag{2.4.12}$$

Applied to (2.4.1) then gives the final expression for the CARB magnetic braking model as presented in Van and Ivanova (2019a),

$$\dot{J}_{mb,CARB} = -\frac{2}{3}\frac{R^{14/3}}{\dot{M}_w^{1/3}}\left(v_{esc}^2 + 2\Omega^2 R^2/K_2^2\right)^{-2/3}\Omega_\odot B_{s,\odot}^{8/3}\left(\frac{\Omega}{\Omega_\odot}\right)^{11/3}\left(\frac{\tau}{\tau_\odot}\right)^{8/3}. \tag{2.4.13}$$

The solar parameters used is listed in Van and Ivanova (2019a) to be, $B_{s,\odot} = 1$ G, $\Omega_\odot \approx 3\times10^{-6}$ s^{-1} and $\tau_\odot = 2.8\times10^6$ s. This is the model used in the simulations of thesis, however since this is an deviation from the standard MB model (Skumanich). Therefore comparisons made to better visualize these differences have been made.

2.4.2 Comparison to Skumanich

The Skumanich magnetic braking model is given by Rappaport et al. (1983) as,

$$\dot{J}_{MB,sku} = -3.8 \times 10^{-30} M R_{\odot}^{4} \left(\frac{R}{R_{\odot}} \right)^{\gamma} \Omega^{3}, \tag{2.4.14}$$

where γ is a parametrization index which in Rappaport et al. (1983) is set to $[0, 1, 2, 3, 4]$ for different models they tested. One clear difference between the two models is the strong dependency on the convective turnover time in the CARB model, whereas the Skumanich model has none. This is also seen in Figure 2.7 which shows the orbital angular momentum loss as a function of time for a system with a donor mass of $M_2 = 1.0$ $M_{\odot}$, $Z = 0.02$, a white dwarf accretor of $M_1 = 0.8$ $M_{\odot}$ and an initial orbital period of $P = 3.0$ days. Here γ has been chosen to be 4. This system has been evolved using the CARB magnetic braking model and it is therefore this model which affects the dynamical process during each computational step. The Skumanich model have just been evaluated parallel at each timestep and plotted next to the CARB model, and has thus no influence on the evolution. This is done in order to better compare the strength of the orbital angular momentum loss of the two models, at different stages in the same evolutionary path. Evolving a system interdependently under each magnetic braking law, with the same initial parameters, could yield drastically different evolutionary tracks and thus complicating a direct comparison of the two models. In this case doing so the Skumanich model results in a divergent system during the first mass transfer phase, with a final period of 11.2 days at the end of the simulation while the CARB model results in an AM CVn system after an initial mass transfer phase. The detached period between the initial mass transfer phase and the AM CVn phase, indicated by the dashed lines in Figure 2.7, last for about 1.7 Gyr and is rather impactful on the CARB model. In this period the star degenerates and becomes almost completely radiative, reducing the convective envelope to only some convection at the very surface of the star. This then results in a significant smaller convective turnover time which then scales the CARB model substantially. This scaling is not seen in the Skumanich model where the only two dependent parameters that change during this phase is the period and the radius. Both the period and the radius decreases during this phase, which result in an increase and decrease of the overall orbital angular momentum loss, respectively. Thus the change is not as dramatic in the Skumanich model as it is in the CARB model. However, the strength of the scaling with respect to radius can be adjusted using the γ-parameter. Choosing for example a larger γ would yield smaller values for the magnetic braking as the radius continues to decrease. This would however lead to a weaker model in the beginning of the evolution, as discussed later in this section with respect to Figure 2.8. Another observation worth noting is the increase in magnetic braking with the CARB model as the degenerate donor initiates mass transfer again in the AM CVn phase. This happens as the donor develops a significant convective envelope, as a consequence of strong mass loss, and thus lengthening the convective turnover time. The CARB model is thus able to factor in different degrees of bloated WD donors which becomes AM CVns, also discussed in Belloni and Schreiber (2023).

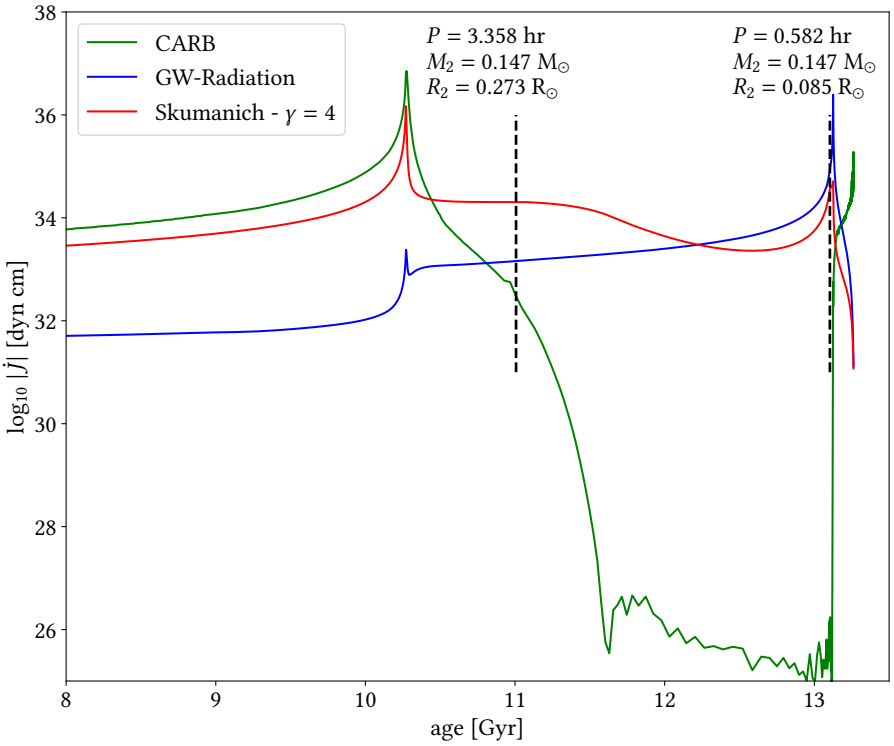

Figure 2.7: Plot showing the orbital angular momentum loss due to magnetic braking from the CARB and the Skumanich model, green and red respectively. The loss due to gravitational wave radiation is shown in green. The two dashed lines indicates the detached period between the inital mass transfer phase and the AM CVn phase. Simulation was made using a $M_2 = 1.0\ M_\odot$, $Z = 0.02$ donor, with a white dwarf accretor of $M_1 = 0.8\ M_\odot$ and an initial orbital period of $P = 3.0$ days. The system was evolved using the CARB magnetic braking model and the Skumanich model has been plotted parallel.

Figure 2.8 shows different parallel tracks for the complete evolution using γ values in the range $[0, 15]$ as a function of model number to better highlight areas with large changes in the system and thus forcing a smaller timestep for each model in these areas. For reference the 8 Gyrs starting point in Figure 2.7 is at model number 132 in Figure 2.8. It can be seen from Figure 2.8 that without implementing other scaling factors it becomes difficult to accommodate the assumption that the magnetic field scales with the convective envelope, without sacrificing the strength of the magnetic braking in the beginning. This loss of orbital angular momentum in the beginning is very important for the evolution of the system, given a set of starting parameters, as it determines how fast the initial mass transfer sets in, and thus how evolved the donor is, which in turn directs the response of the star due to the mass transfer. A $\gamma = 1.75$ leads to the same initial magnetic braking values for both CARB and Skumanich, however CARB overtakes again as the convective envelope grows. Furthermore, lowering γ in order to finetune the initial strength can lead to torques which are several orders of magnitude larger during the AM CVn phase, as evident from the orange line in Figure 2.8. The Skumanich model also leads to two points during the evolution where the magnetic braking is the same for all γ, where the radius is 1 $R_\odot$. This is also evident in (2.4.14). In this scenario, the radius of the donor becomes greater than 1 $R_\odot$ before the initial mass transfer phase initiates, and after losing some mass it becomes less that 1 $R_\odot$. This creates a small window where increasing γ will lead to stronger magnetic braking. Where in the rest of the evolution this will lead to a weakening of the magnetic braking.

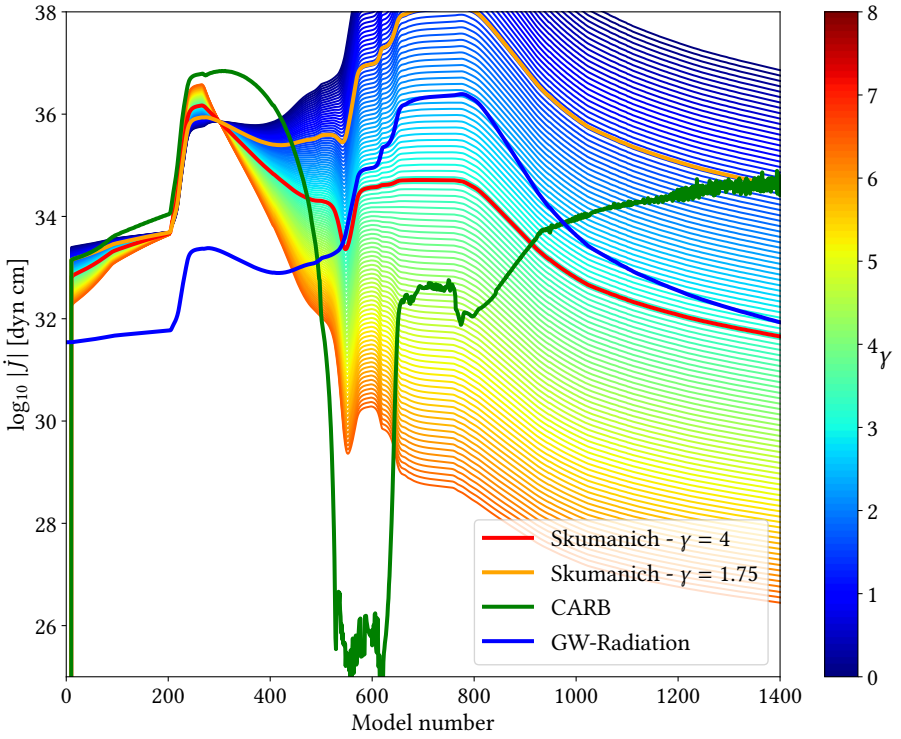

Figure 2.8: Plot showing the orbital angular momentum loss due to magnetic braking from the CARB and the Skumanich model. Further, the loss due to gravitational wave radiation is shown in green. The Skumanich model has been plotted 100 times using different values of γ between 0 and 8 as indicated by the color bar. The red and orange lines shows the Skumanich model using $\gamma = 4$ and $\gamma = 1.75$ respectively. Simulation was made using a $M_2 = 1.0\ M_\odot$, $Z = 0.02$ donor, with a white dwarf accretor of $M_1 = 0.8\ M_\odot$ and an initial orbital period of $P = 3.0$ days. Simulation was evolved using the CARB magnetic braking model and the Skumanich models has been plotted parallel.

The CARB model is an overall stronger magnetic braking prescription in the beginning of the evolution, where magnetic braking matters the most. This leads to a larger window of initial parameters that results in a compact binary, as will be discussed in chapter 4. Its high dependency on the convective turnover time also has its advantage as it better reflects the theory behind large-scale magnetic field generation in sun-like stars, which depends on the convective zone. Thus, this magnetic braking model has been used in the simulations within this thesis.

Another source of angular momentum loss is through GWR, which has a significant effect in compact binaries. Thus, this phenomenon is elaborated upon in the following section while also explaining the detectability of GWR from compact binaries with respect to LISA.

2.5 Gravitational Wave Radiation

The change in orbital energy due to gravitational radiation can be expressed as the negative value of the gravitational wave luminosity. Peters and Mathews (1963) derive an expression for the average energy radiated from a binary system, and thus the change in orbital energy to be,

$$\dot{E} = -L_{gw} = -\frac{32}{5}\frac{G^4}{c^5}\frac{M_1^2 M_2^2 M}{a^5} f(e). \tag{2.5.1}$$

Here $f(e)$ is an enhancement factor for eccentric systems given by,

$$f(e) = \frac{1 + (73/24)e^2 + (37/96)e^4}{(1-e^2)^{7/2}}, \tag{2.5.2}$$

which for circular systems is $f(0) = 1$. Note (2.5.1) is only valid given the "quadrupole approximation", which assumes that the dimensions of the system are much smaller than the wavelength of the gravitational wave,

$$a \ll \lambda_{gw}. \tag{2.5.3}$$

For circular orbits the frequency of the gravitational waves emitted is given by,

$$f_{gw} = 2f_{orb} = \frac{2}{P}, \tag{2.5.4}$$

as two waves are emitted per orbital period. Thus the wavelength of the gravitational wave is,

$$\lambda_{gw} = \frac{c}{f_{gw}} = \frac{c}{2f_{orb}} = c\frac{P}{2}. \tag{2.5.5}$$

Using Kepler's third law in (2.5.3), this sharp inequality can then be rewritten as,

$$c\frac{P}{2} \gg \left(\frac{P^2 G}{4\pi} M\right)^{1/3} \tag{2.5.6}$$

$$\frac{\pi c^3}{2G} P \gg M. \tag{2.5.7}$$

The constant fraction in front of the orbital period in (2.5.6) is of order 10^{38} g s^{-1}. Assuming the lowest known orbital period for an AM CVn (HM Cnc, see A.1) of $P \approx 321$ s, to try an break the inequality, constrains the systems to have a total mass $M \ll 10^8$ M$_\odot$. As these systems typically have a total mass of around 1 M$_\odot$ this approximation is very valid.

From the total orbital energy and the orbital angular momentum of a circular binary system given by,

$$E_{orb} = -\frac{GM_1M_2}{2a}, \quad J_{orb}^2 = \frac{Gm_1^2 m_2^2}{M} a, \tag{2.5.8}$$

the change in orbital angular momentum due to gravitational wave radiation can be derived. This is done by first inserting J^2 into the orbital energy equation and differentiating,

$$E_{orb} = -\frac{G^2 M_1^3 M_2^3}{2M}\frac{1}{L^2} \quad \Rightarrow \quad \dot{E} = \frac{G^2 M_1^3 M_2^3}{2M}\frac{\dot{J}_{gw}}{J^3} = \frac{GM_1M_2}{a}\frac{\dot{J}_{gw}}{J_{orb}}. \tag{2.5.9}$$

Combining (2.5.1) and (2.5.9) then gives the final expression,

$$\frac{\dot{J}_{gw}}{J_{orb}} = -\frac{32}{5}\frac{G^3 M_1 M_2 M}{c^5 a^4}. \tag{2.5.10}$$

This equation is also the standard prescription for orbital angular momentum loss used by `MESA` in this thesis.

To find an expression for the received gravitational strain amplitude, Press and Thorne (1972) provides an expression for the flux,

$$F_{gw} = \frac{c^3}{16\pi G}\langle \dot{h}_+^2 + \dot{h}_\times^2 \rangle, \tag{2.5.11}$$

where $\langle \dot{h}_+^2 + \dot{h}_\times^2 \rangle$ is the time average of the derivatives squared for the "plus" and "cross" polarization amplitudes, respectively. Then adopting the same assumption as in Douglass and Braginsky (1979), for continuous gravitation radiation, stating isotropic radiation and that the flux falls of as the distance squared yield,

$$F_{gw} = \frac{L_{gw}}{4\pi d^2} = \frac{c^3}{16\pi G}\langle \dot{h}_+^2 + \dot{h}_\times^2 \rangle \quad \Rightarrow \quad \langle \dot{h}_+^2 + \dot{h}_\times^2 \rangle = \frac{4L_{gw}G}{c^3 d^2}. \tag{2.5.12}$$

In Douglass and Braginsky (1979) the distance d is presented as the distance from the source to the detector. However, this distance may be modified in cosmologically red-shifted environments, thus often denoted as the luminosity distance, d_L; the apparent distance to the source. For these AM CVns to be detectable, as shown later in this section, they must be within our galaxy, thus cosmological red-shift has no effect. The final effect stems from the line of sight velocity, which also has no effect as v_r/c never becomes meaningful except in very extreme environments like near the center of the galaxy. However, detecting these theoretical AM CVn systems becomes problematic due to both distance and galactic noise, as also discussed later in this section. Thus it is assumed that $d \approx d_L$.

The two polarizations amplitudes depends on the inclination angle of the observed binary, here the two components can be written as,

$$h_+(t) = h\frac{1+\cos^2(i)}{2}\cos(\omega_{gw}t) \tag{2.5.13}$$

$$h_\times(t) = h\cos(i)\sin(\omega_{gw}t), \tag{2.5.14}$$

adopting the monochromatic expression from Maggiore (2008). Here i is the inclination angle, $\omega_{gw} = 2\pi f_{gw}$ is the angular frequency and h is the amplitude parameter defined such the two polarizations are of equal amplitude for face-on binaries. These expressions thus take into account that when the orbit is edge-on the received gravitational signal is linearly polarized, and only h_+ contributes.When the binary is face-on the signal is circular polarized, and both h_+ and $h_\times$ is received. These two types of polarizations can be seen in Figure 2.9 B and A respectively.

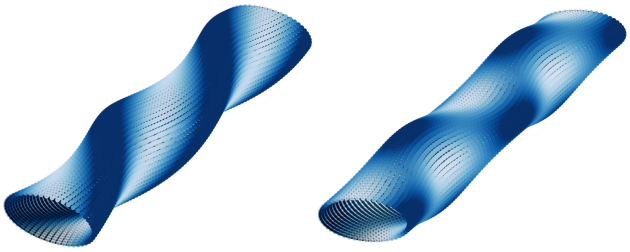

Figure 2.9: Graphical illustration of gravitational waves influence test particles placed in a circle. (A) shows a circular polarized wave, expected from a face on circular binary, and (B) shows a linear polarized wave expected from a edge-on binary. Both waves show two periods.

Differentiation and squaring of both components in (2.5.13) leads to,

$$\dot{h}_+^2 = \left[h\frac{1+\cos^2(i)}{2}\right]^2 \omega_{gw}^2 \sin^2(\omega_{gw}t), \tag{2.5.15}$$

$$\dot{h}_\times^2 = [h\cos(i)]^2 \omega_{gw}^2 \cos^2(\omega_{gw}t). \tag{2.5.16}$$

The time average of both $\sin^2$ and $\cos^2$ yield 1/2, thus the sum reduces to,

$$\langle \dot{h}_+^2 + \dot{h}_\times^2 \rangle = h^2 \omega_{gw}^2 \left[\frac{1 + \cos^4(i) + 6\cos^2(i)}{8} \right] = h^2 \omega_{gw}^2 (g(i))^2, \tag{2.5.17}$$

where $g(i)$ is a function modifying the amplitude based on the inclination angel yielding values in the interval $[1, \sqrt{2}/4]$, thus for face-on binaries the amplitude is h and for edge-on binaries it is $\approx 0.35h$. Assuming face-on binaries, as these yield the strongest signal and is thus more plausible to detect, and inserting (2.5.17) into (2.5.12) then yields,

$$h = \sqrt{\frac{16\pi G F_{gw}}{c^3 \omega_{gw}^2}} = \sqrt{\frac{4G}{\pi c^3 f_{gw}^2} \frac{L_{gw}}{4\pi d^2}} = \sqrt{\frac{G L_{gw}}{\pi^2 c^3 f_{gw}^2 d^2}}. \tag{2.5.18}$$

Inserting the Luminosity from (2.5.1) yields,

$$h = \sqrt{\frac{32}{5}} \sqrt{\frac{G^5}{\pi^2 c^8 f_{gw}^2 d^2} \frac{M_1^2 M_2^2 M}{a^5}}. \tag{2.5.19}$$

Using Kepler's third law to replace the orbital separation and $P = 2/f_{gw}$ yields,

$$h = \sqrt{\frac{32}{5}} \sqrt{\frac{G^5}{c^8 d^2} \frac{\pi^{4/3} f_{gw}^{4/3} M_1^2 M_2^2}{G^{5/3} M^{2/3}}}. \tag{2.5.20}$$

Collecting all mass variables into one variable, the chirp mass, $\mathcal{M}$, then gives the final expression for the strain,

$$h = \sqrt{\frac{32}{5}} \sqrt{\frac{G^{10/3}}{c^8 d^2} \frac{\pi^{4/3} f_{gw}^{4/3} M_1^2 M_2^2 M}{M^{5/3}}} = \sqrt{\frac{32}{5}} \frac{\pi^{2/3} G^{5/3} f_{gw}^{2/3}}{c^4 d} \mathcal{M}^{5/3}, \tag{2.5.21}$$

where,

$$\mathcal{M} = \frac{(M_1 M_2)^{3/5}}{(M_1 + M_2)^{1/5}}. \tag{2.5.22}$$

The characteristic strain, which is the stain measured over many periods of the orbit to increase the signal-to-noise, is given as (Tauris and van den Heuvel, 2023),

$$h_c = \sqrt{N} h, \tag{2.5.23}$$

where $N = f_{gw} T$ with T being the observation time. For LISA the proposed nominal mission time is 4 years (Amaro-Seoane et al., 2017). The characteristic strain can then be compared to the sensitivity curve for LISA which is the curve determining the baseline signal noise amplitudes with respect to frequency. The sources should therefore have higher characteristic strain amplitudes than those given by this sensitivity curve, in order to be able to distinguish the signal from the noise. This makes it a useful tool for assessing if a system is be detectable. These sensitivity curves shown in Figure 2.10 have been generated from Robson et al. (2019) using the associated `Python` code downloaded from Cornish (2019). The curves presented are using the sky-averaged signal-to-noise ratio. This can of course be misleading as the sensitivity may vary across the sky. However, as the observation time increases this sensitivity increases overall, also in noisy areas. As an example the contribution from the galactic confusion noise, depicted as the bumps where the dotted, dashed and dash dotted lines are in Figure 2.10, is stronger when the antenna points in the direction of the galactic center and weaker when pointed away from it, as discussed in detail in Robson et al. (2019).

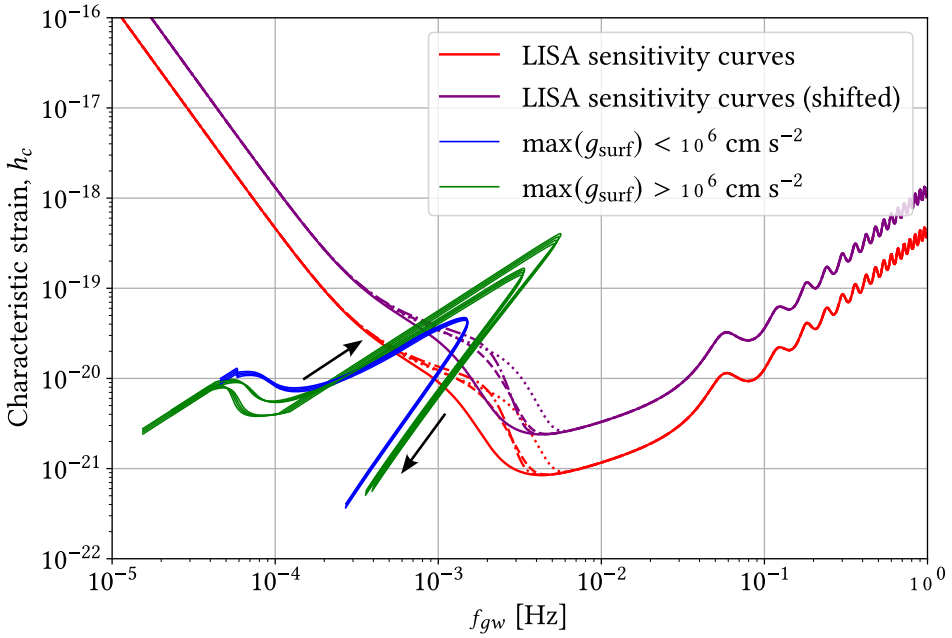

Figure 2.10: The sensitivity curve for LISA for observation time $T = [0.5, 1, 2, 4]$ years for the dotted, dash dotted, dashed and the full red and purple lines respectively. The purple lines is shifted on the y axis by 0.45, further explanation in main text. The blue and green lines shows the evolutionary track for selected systems which go past the sensitivity assuming a distance $d = 1$ kpc and an observation time of $T = 4$ years. The color indicates if the system becomes a white dwarf with respect to the surface gravity. The black arrows indicate the direction of the evolution.

Figure 2.10 shows a selected handful of systems which ends up with $h_c >$ LISA sensitivity curve. The systems plotted all have donor masses of $M_2 = 1.25$ $M_\odot$. The accretor mass varies in the range $M_1 = [0.85, 1]$ $M_\odot$ and the post-CE period varies in the range $P_0 = [0.5, 1.5]$ days. The shifted purple lines represent the sensitive curves for which the calculated strain amplitude, for edge-on binary, needs to exceed in order to be detectable. In reality for edge-on binaries, the strain is shifted down on the log scale by $\log_{10}(\sqrt{2}/4) \approx -0.45$, however for illustrative purposes the purple lines are shifted up instead. The distance is assumed to be $d = 1$ kpc. If the distance is greater, the track move down and becomes less detectable. For a change in characteristic strain on the log scale of -1, the more luminous systems becomes barely detectable, but this would also imply an increase in distance of 10 kpc, which is past the center of the Milky Way, making detecting the systems otherwise difficult due to galactic noise. In Figure 2.10 the observation time is chosen to be $T = 4$ years for the evolutionary tracks. However, after only 6 months some of the very luminous systems are expected to be resolvable from noise. In Figure 2.10 this corresponds to a shift on the log scale of $\log_{10}(\sqrt{1/8}) \approx -0.45$, thus still placing the peaks of the green tracks above both the purple and red sensitivity curves.

This finalizes the physics behind gravitational wave radiation, its influence on the orbit of binaries, and the detectability of the systems within the gravitational wave spectrum. However, this only applies under the assumptions that the binary is circular, the gravitational wavelength is much smaller than the orbital separation, the gravitational wave amplitude fall off as the distance squared, and that the wave is monochromatic.

All relevant theory has now been investigated. In the next chapter, the observational data used to compare with our simulations will be presented. Furthermore, a section about the MESA specifics is included to explain the relevant simulation parameters.

Chapter 3

Observational Data and Simulation Specifics

3.1 Observational Data

To evaluate the results of the simulations, observational data are necessary. Therefore, relevant systems have been picked out, which have estimated parameters other than orbital period, such as: mass of donor, mass of WD accretor, mass transfer rate and radius of the donor. Both AM CVn systems and evolved CVs have been selected in order to give a more representative subset of systems which follow the evolution considered in this thesis. A list of the considered AM CVn and CV systems can be seen in Table A.1 and A.2 respectively.

3.1.1 AM CVns

Our main source for comparison systems is Ritter and Kolb (2003). It is a detailed cataloger with a wide range of semi-detached and detached cataclysmic binaries and low mass X-ray binaries (LMXBs). They define a cataclysmic binary as a system with a WD, or WD precursor primary, and a low mass star as the secondary, the secondary may be evolved as for AM CVns. The subtype of a given system is also available for those that have been classified, one is the AM CVn type. This allows us to distinguish the relevant systems from the huge number of systems and extract relevant parameters from the database, which are the period and masses. For the purpose of our thesis, the semi-detached cataclysmic dataset is used both to get an initial set of AM CVn systems and CVs where mass transfer is ongoing.

As stated previously, we would like more parameters and have thus found other sources which estimate these. For AM CVns, the primary source for this information is Solheim (2010); and references therein, where mass transfer rates and some masses have been extracted. Additionally, a system which is not in the database of Ritter and Kolb (2003), named SDSS J092638.71+362402.4 (J0926+3624), was added. This was also done using the mass transfer rates found by Ramsay et al. (2018); Fontaine et al. (2011), where 4 new systems were added. In Belloni and Schreiber (2023) they used observational data for 8 AM CVns, which had estimated radii. These were taken from van Roestel et al. (2022), and has also been added to our dataset.

The methods which have been used to determine the different parameters of the systems will not be elaborated as it is beyond the scope of this thesis. However, the potential uncertainty of some of these parameters should be mentioned. The orbital periods are well known and have been estimated with high precision; this is also the reason why no uncertainties have been stated. However, some of the mass transfer rates stated in Table A.1 have been specifically selected by us, since there was a multiple of different estimations for this parameter. As a rule of thumb the lower values were selected, but some of the other estimations were also poorly constrained, hence the other estimate was used. Four systems, named J1908+3940, HP Lib, GP Com and V396 Hya had a multiple of different estimated mass transfer rates, the alternative mass transfer rates are,

$$[(6.6 \pm 3.1) \times 10^{-7}, (5.5 \pm 1.9) \times 10^{-9}, < 4.3 \times 10^{-12}, \sim 10^{-11}] \ \mathrm{M}_{\odot} \ \mathrm{yr}^{-1},$$

respectively (Solheim, 2010; Ramsay et al., 2018). Most of the alterative, estimated mass transfer rates agree somewhat, but for J1908+3940 they differ by a factor ~ 100. In Ramsay et al. (2018) they do mention that the mass transfer rates for some systems are higher than predicted by other models, which might be due to the donors having larger radii than expected. However, they assume that the disc is in a steady state and that the primary has a mass of $0.80 \pm 0.10\ M_{\odot}$. These assumptions might lead to substantial discrepancies, as it could be in a high state meaning that most of the light, which is received, stems from the accretion disc (Fontaine et al., 2011). Furthermore, Ramsay et al. (2018) used the spectral energy distribution (SED) to infer a mass transfer rate, whereas Fontaine et al. (2011) used a non-local thermodynamic equilibrium accretion disc fit. Thus, it seems reasonable to use the mass transfer rate of Fontaine et al. (2011) as they are able to better account for the high state accretion disc.

For the masses and radii, the best estimates are given for eclipsing systems, where high-speed photometry is used (Green et al., 2018). However, not all of our chosen systems are eclipsing, but estimating the masses is still possible in some cases. For example, the masses of HM Cnc are determined by using the direct impact model to constrain them, in terms of the observed phase shape of the photometry measurements (Barros et al., 2007). Some systems had a multiple of reported masses for either the donor or the WD, but unlike for the mass transfer rates, there were not too large discrepancies and estimates with uncertainties were prioritized. Only donor radii of eclipsing systems have been considered (van Roestel et al., 2022).

3.1.2 Evolved CVs

For the CV population, two categories were chosen, evolved CVs and CVs with secondaries that are progenitors of extremely low mass white dwarfs (ELM WDs). For the prior, systems which have estimated masses and radii were chosen following Belloni and Schreiber (2023). This left us with 9 systems, that have evolved donors. The ELMs are systems which are in a transition phase towards an AM CVn. In El-Badry et al. (2021) 21 systems which currently have mass transfer or recently became detached are investigated. Conveniently, they have estimated the masses and radii using the SEDs for all the systems, which is convenient for our purpose. This gives us a good sample of systems to compare with in terms of the potential detached phase that some of our systems go through when evolving towards an AM CVn.

In order to investigate potential biases in our chosen observational data, different plots have been made for some of the parameters. The distribution of the orbital periods for the observational data can be seen in Figure 3.1a, where it is clearly seen that we have an abundance of systems with orbital periods of $P \lesssim 1$ hrs, these are the AM CVns. The evolved CVs have orbital periods which are more spread out, but the main bulk between 3 hrs$< P <$ 5 hrs is dominated by the ELMs. A few systems also occupy the period gap 2 hrs$\lesssim P \lesssim$ 3 hrs, these are ELMs. We have 54 AM CVn systems compared to 30 evolved CVs where 21 of these are ELMs.

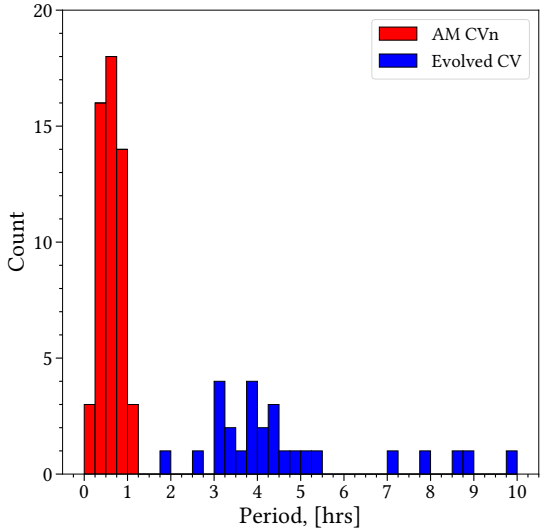

(a) Histogram showing the distribution of orbital periods of the selected systems.

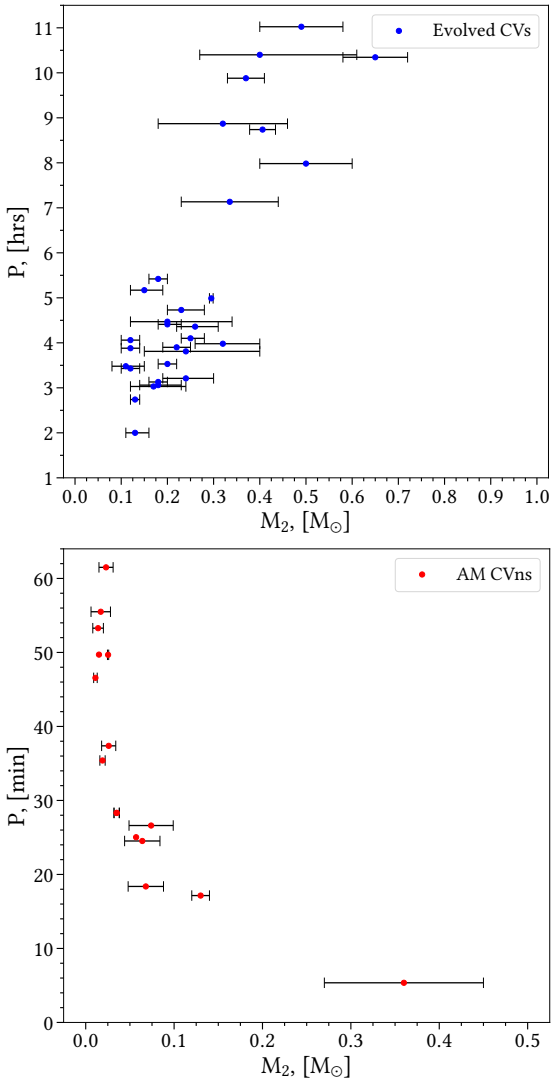

(b) Distribution of donor masses in terms of orbital period. AM CVns has been separated from the evolved CVs in accordance with orbital period. Note the different ranges of the axes.

Figure 3.1: Plots showing the distribution of orbital period and donor mass for both AM CVns and evolved CVs. Note that not all the AM CVns systems in the data has an estimated donor mass, hence not all can be plottet in the bottom right.

To the right in Figure 3.1 the period is plotted in terms of the donor masses for both the evolved CVs and the AM CVns. A general tendency for the evolved CVs is that as the donor gets less massive, so does the orbital period. This is in agreement with the expected evolution of CVs, where the orbital period shrinks as it experiences mass transfer. The opposite trend is seen for the AM CVns, as the masses of the donors become more massive, the orbital periods decrease. However, since these donors are expected to be degenerate objects, this is also in good agreement with the evolutionary scenarios because the radius is inversely proportional to the mass for degenerate WDs. This allows the binary to reach lower orbital periods.

Another interesting effect can be shown for the masses and radii of the donors. In Figure 3.2, these two parameters have been plotted. It is seen that some of the donors are bloated, meaning they have a radius which is larger than what is expected for a normal main sequence star. The approximate mass-

radius relation for main sequence stars, $R \approx (M_2/\mathrm{M}_\odot)^{0.8}$, is shown, thus systems where the donor has a radius greater than that given by this relation are bloated.

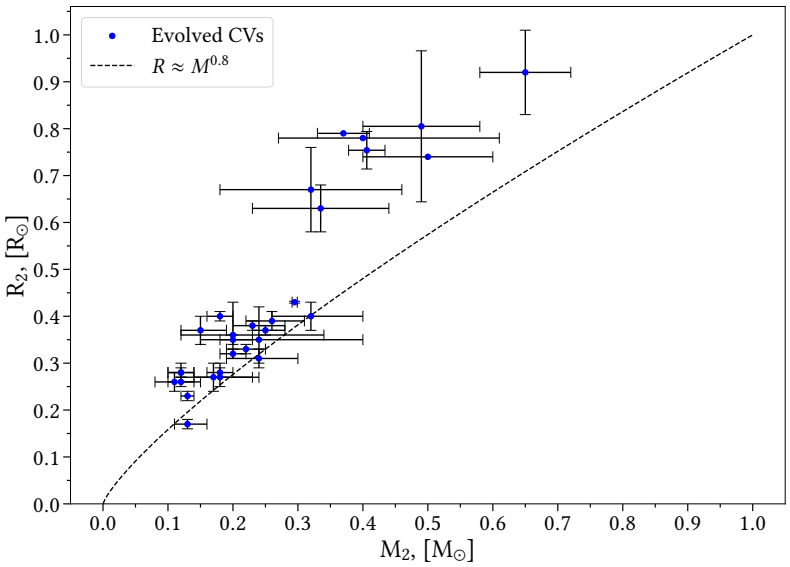

Figure 3.2: Radii of the donor stars in terms of their masses. The approximate mass-radius relationship for main sequence stars has also been plotted to emphasize the bloated nature of the donors in some of the evolved CVs.

This is an effect caused by mass transfer, if the donor loses mass faster than the time it takes for it to settle back into thermal equilibrium, it stays somewhat expanded (Knigge et al., 2011). The systems which follow this relation (some of the ELMs) might therefore be on the verge of ending mass transfer or do not experience it. This is exactly the case for some of the ELMs (El-Badry et al., 2021).
Additional plots for the different parameters can be seen in Appendix A.

Now that the comparison data has been presented, the framework for the simulation setup will be elaborated. Both the different effects, we implement in terms of the binary stellar evolution, but also that of the donor star.

3.2 Simulation Specifics

The numerical simulation done in this thesis is made using the `MESA` code version 24.08.1 Paxton et al. (2011, 2013, 2018, 2019, 2015); Jermyn et al. (2023). Some settings has been changes from the default values in `MESA` to better accommodate our simulations. Some are already presented in the theoretical sections such as magnetic braking and the Eddington accretion limit. If something is not specifically presented in the following the default in `MESA-24.08.1` is used.

3.2.1 Binary Parameters

As presented in section 2.3 the accretion onto the WD needs to be modified depending on the mass and the available material from mass transfer. This is handled in the `extras_binary_start_step` by calculating η_H and η_{He}, as describe in section 2.3 and then equating $\beta = 1 - \eta_{He}\eta_H$. Thus, mass not accumulated is lost in a wind near the accretor. Furthermore, the Eddington accretion limit presented in

Section 2.2.3 is handled using the `use_other_mdot_edd` routine and the described model is thus written into the `mdot_edd_routine` in the `run_binary_extras.f90`, thereby modifying $\dot{M}_{edd}$. In much the same manner, the CARB magnetic braking model has been implemented using the `use_other_jdot_mb` routine where the code associated with Van and Ivanova (2019a) (available from Van and Ivanova (2019b)), is implemented. However, this code has been slightly modified since it was made for an older version, and newer version of MESA has controls implemented for when to apply magnetic braking based on the present fractions of the convective envelope and convective core of the donor. From these settings only the minimum allowed mass fraction of the convective envelope, `jdot_mb_min_qconv_env`, has been change to 0 from the default values of 10^{-6}. This is done due to the CARB model already taking the convective envelope into account through the convective turnover time. Due to the assumption that the system is tidally locked angular momentum loss due to spin-orbit coupling (tidal torques) has been switched off. This sort of angular momentum loss is also already being taken care of implicitly by the magnetic braking.

Lastly with respect to the binary controls, some timestep parameters and tolerances have been changed to relax the models a bit in periods of large mass, separation, and angular momentum changes. This would otherwise lead to premature termination due to computational errors.

3.2.2 Donor Parameters

This section highlights the physical schemes and parameters which are changed, with respect to the donor star, within our simulations compared to the default MESA-24.08.1 code. Some timestep parameters and tolerances have also been change here, in order to relax or constrain the models, however as these do not change the overall physical assumptions, they are not included in this section.

Metallicity and Opacity. The donor stars in the different models all have sun-like metallicities of $Z = 0.02$ using the type 2 opacity table. For low temperatures the `Freedman11` table is used. This table is based on Freedman et al. (2008) and was specifically made to incorporate ultra-cool dwarfs and extrasolar planets, and goes as low as 75 K. Since AM CVn donors are expected to become very cold, helium-rich, planet-like remnants, this table is used to better capture the opacities related to this late-stage phase.

Equations Of State. MESA uses a blend of included equations of state (EOS). All available equation of state prescriptions has been included in the simulations, as these are valid in different ranges of temperature, pressure and composition and thus better coverage is ensured. The EOSs included are the CMS (Chabrier et al. (2019)), Skye (Jermyn et al. (2021)), PC (Potekhin and Chabrier (2010)), FreeEOS (Irwin (2008)), OPAL/SCVH (Rogers and Nayfonov (2002); Saumon et al. (1995) and HELM (Timmes and Swesty (2000)) equations of state. The blending occurs in areas with overlap between multiple EOSs, such that moving from one equation of state to another happens smoothly. Since the donor is expected to become increasingly degenerate during its evolution the default energy option has been change from `dedt` to `eps_grav` as the latter leads to lower error in entropy and are thus less likely to create unphysical behavior at the cost of potentially larger errors in the total energy conservation, as explained in the MESA documentation.

Mixing Length Theory and Atmosphere Boundary Conditions. The default mixing length theory (MLT) in MESA, that being the `TDC` model from Kuhfuss (1986), assumes optically thick material and is not valid in very low optical depth regions. In order to include convection in the optically thin regions, as well, the `Henyey` model, from Henyey et al. (1965), is adopted. This model provides extensions to the MLT

in order to work in optically thin regions, as well. This is appropriate for these systems which evolve into degenerate donors where the convective envelope becomes very shallow, yet still has an effect on the turnover time and thus on the angular momentum loss through the CARB magnetic braking model. These differences between MLTs are reviewed more in depth in Joyce and Tayar (2023). The default mixing length $\alpha = 2$ is used. For the atmospheric boundary conditions, the `varying` opacity option is used. This is done in order to better capture the boundary conditions in the later degenerate stages, as this option evaluates the local temperature and pressure, varying the opacity throughout the atmosphere. Contrary to the default `fixed` option which uses a uniform opacity, thereby avoiding errors due to steep gradients.

Wind Mass Loss. Wind mass loss has been included using the standard `Reimers` scheme implemented in `MESA` following Reimers (1975), to account for mass loss which can influence the orbital angular momentum loss through magnetic braking. The Reimers scaling factor has been set to the typical value of 0.5 as explained in the `MESA` documentation. This values is also consistent with the median reported by McDonald and Zijlstra (2015) of $0.477^{+0.050}_{-0.062}$, based on a study of 56 Galactic globular clusters across a wide range of metallicities. Although they found this value to be independent of metallicity.

Nuclear Network. To more accurately track the nuclear burning in the higher mass donors, where the CNO-cycle dominates hydrogen burning, the nuclear network is changed to `cno_extras.net`, which includes more isotopes than the basic network for better abundance tracking. This increased number of isotopes also leads to changes within the diffusion representative settings, which tracks the redistribution of these isotopes of similar atomic mass number over time. The default species that are tracked are H-1, He-3, He-4, O-16 and Fe-56. If any other isotopes are present these will then be binned into the isotope with the atomic mass number equal to or larger than said isotope, with the exception of isotopes heavier than Fe-56, these are all binned into Fe-56 to create a cap. To account for the isotopes in the CNO-cycle this list is expanded with C-12, C-13, N-14. Furthermore, Ne-20, Mg-24 is also included, for completion, as these are part of the `basic`-network, however these are not expected to become relevant for the mass range in this thesis, although some isotopes included in the `cno_extras.net` will be binned into these and thus diffuse in the star as if they all have atomic number 20 and 24 respectively, all to ease calculations.

3.2.3 Accretor Parameters

The WD accretor is treated as a point mass in our simulations. This approximation is justified as the WD's radius remain significantly smaller than the orbital separation in the majority of the evolution, and the response to accretion is handled separately. Using using (2.2.24) for the WDs radius, at minimum separations the ratio between the orbital separation and the accretor radius was found to be $R_1/a \sim 0.1$, thus at least approaching non-negligible regimes. Nevertheless, for computationally simplicity, and because the donors evolution is the main focus, we adopt the point mass approximation rather than evolving both stars.

Thus, the initial settings and parameters have been presented. The following sections contain the result of our simulations, starting with a general presentation of our initial grid search. This is then followed by a more in-depth analysis of the results and comparisons with observational data.

Chapter 4

Simulation Results

4.1 Grid Search Results

An initial grid of 270 systems using different donor mass, accretor mass, and post-CE orbital period is used. This grid is set up in the following way,

$$M_{1,0} = [0.6, 1]\ \mathrm{M}_\odot \text{ in steps of } 0.05\ \mathrm{M}_\odot, \tag{4.1.1}$$

$$M_{2,0} = [1, 1.5]\ \mathrm{M}_\odot \text{ in steps of } 0.125\ \mathrm{M}_\odot, \tag{4.1.2}$$

$$P_0 = [0.5, 3] \text{ days in steps of } 0.5 \text{ days}. \tag{4.1.3}$$

Later on a finer grid is made to better highlight features for systems which becomes AM CVns. This is discussed in section 4.3.

4.1.1 Helium Core Mass

The initial grid of post-CE parameters is as presented in (4.1.1), (4.1.2), (4.1.3). The simulations were terminated if they reached a max age of 14 Gyr which is roughly a Hubble time. Furthermore, if the donor mass reached a minimum of 0.02 $\mathrm{M}_\odot$ the simulation was terminated as well, because only subtle changes happened between that point and a Hubble time. However, this is changed later to investigate what happens in the later stages of evolution for the systems that reach the AM CVn phase. Figure 4.1 shows the evolution of the He-core mass for these track as a function of age. The red track are systems which do not peak over the sensitivity curve for LISA, assuming 4 year of observation and face-on binaries at a distance of 1 kpc. These tracks can be divided into 3 categories; systems that never develop a He-core, systems that develop a He-core not big enough to become detectable in the compact binary phase, and finally systems that develop a large He-core but never becomes a compact binary within a Hubble time.

The latter can be further divided into two sub-categories. Some of the tracks would, if the max age was extended slightly, become AM CVns, while the systems with larger He-core masses require a larger initial orbital separation for them to be able to develop. This will then lead to a larger orbital separation after the initial mass transfer phase. Once the system becomes detached the star degenerates and becomes a white dwarf. Here magnetic braking has little to no effect, thus gravitational wave radiation is the only factor which can potentially tighten the orbit enough to initiate a secondary mass transfer phase. However, if the orbital separation is too larger once these system become detached, i will take a very long time before the second mass transfer phase is reached. This can be seen by rearranging (2.5.8) and differentiating with respect to time yield,

$$\dot{a} = \frac{GM_1M_2}{2E_{orb}^2}\dot{E}_{orb}. \tag{4.1.4}$$

Inserting (2.5.1), as the change in orbital period happens due to gravitational wave radiation, yield,

$$\dot{a} = -\frac{64}{5}\frac{G^3}{c^5}\frac{M_1M_2M}{a^3}, \tag{4.1.5}$$

taking the definite integral of the inverse with respect to the orbital separation yield the time from detachment to Roche lobe overflow again,

$$t_{RL} = \int_{a_0}^{a_{RL}} \frac{1}{\dot{a}} \mathrm{d}a = \frac{5}{256} \frac{c^5}{G^3} \frac{1}{M_1 M_2 M} \left(a_0^4 - a_{RL}^4\right), \tag{4.1.6}$$

where a_0 is the orbital separation at detachment and a_{RL} is the orbital separation when Roche lobe overflow initiates again. Thus the systems become highly dependable on the orbital separation at detachment. As seen from Figure 4.1 these higher mass white dwarfs all lie in the mass range of approximately $[0.165, 0.21]$ $\mathrm{M}_\odot$. Assuming accretor masses in the range $M_2 = [0.6, 1]$ $\mathrm{M}_\odot$ and then combining (2.2.2) and (2.2.24) yield orbital separations at the secondary mass transfer phase in the range $a_{RL} \sim [0.65, 0.88]$ $\mathrm{R}_\odot$. At detachment close to all of these higher mass He-core systems have $a_0 > 2.5$ $\mathrm{R}_\odot$, however even assuming an equality here to minimize would yield $t_{RL} \geq 22.8$ Gyrs. Thus the systems never evolve into AM CVns within a Hubble time, even without counting the time it takes the core to develop. The red tracks which have $a_0 < 2.5$ $\mathrm{R}_\odot$ include these edge cases where they nearly become AM CVns within a Hubble time, but remain undetectable. An example of this can be seen by looking at the 14 Gyrs gridline in Figure 4.1 where the track with the lowest He-core mass there is green. This indicates that the system has become just tight enough to peak over the sensitivity curve for LISA, however the systems never reach the point where the secondary mass transfer phase is initiated before termination due to it reaching the max age of 14 Gyrs.

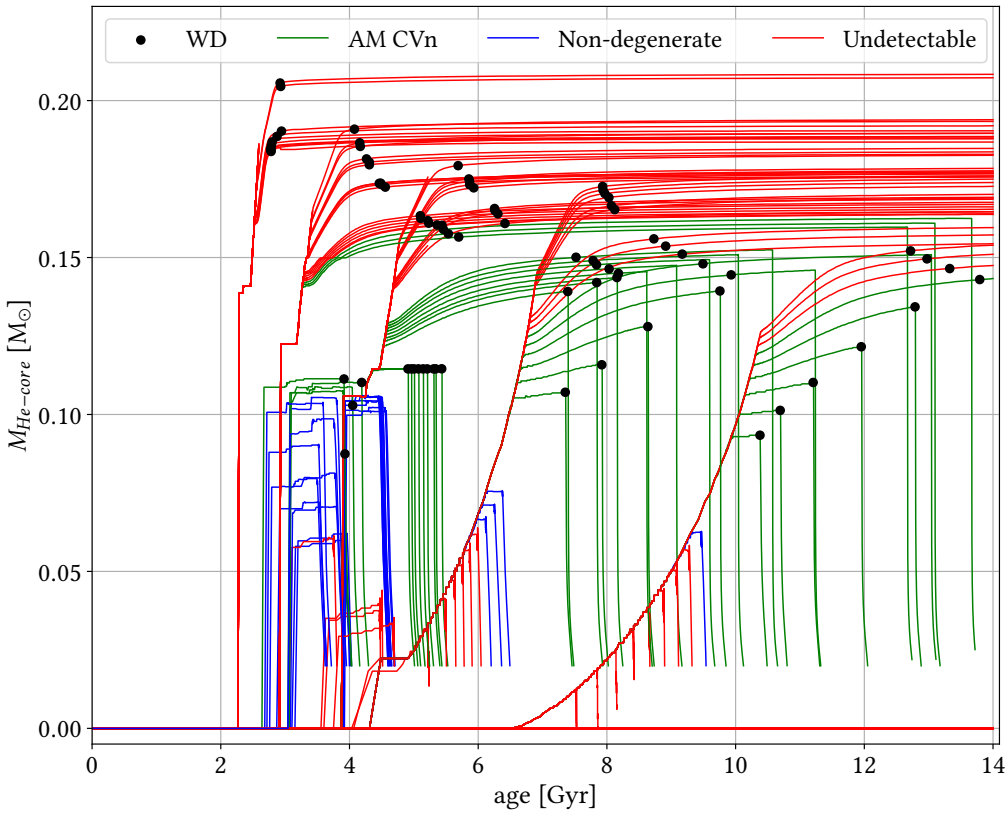

Figure 4.1: Simulated tracks for the He-core mass of the initial 270 systems as a function of age. The red lines shows systems which do not become strong enough sources in the gravitational wave spectrum to peak over the LISA sensitivity curve after 4 years of detection assuming a face-on binary at a distance of 1 kpc. The green lines show tracks for systems which both degenerates and becomes compact enough to emit detectable gravitational waves. The blue lines shows tracks for systems which do not completely degenerate, however still meet the above mentioned criteria for being detectable. The black dots show where the donor becomes a white dwarf as the surface gravity reach $g_{\mathrm{surf}} > 10^6$ cm s^{-2}.

The red tracks which do develop a low mass He-core but do not become GW sources share the fact that they do not degenerate completely with the blue tracks. These blue tracks just barley peaks over the sensitivity curve and are thus probably not detectable in the GW spectrum. However, it does suggest that a smooth transition exists between these semi-degenerate compact binaries and AM CVns. This is also evident from some of the lower He-core mass green tracks which at some point in their evolution gets $g_{\rm surf} > 10^6$ cm s^{-2}. For some of these systems this happens right before the core starts losing mass via mass transfer. This suggests that they have some residual hydrogen in the envelope which needs to be stripped before the core is exposed, and by extension suggests that a smooth evolutionary transition exists between ELMs and AM CVns. For systems that become AM CVns and degenerates during the detached phase, there seems to be a sweet-spot in the He-core masses in the range $[0.125, 0.16]$ M$_\odot$. If including systems that become compact during the secondary mass transfer phase, the range becomes about $[0.075, 0.16]$ M$_\odot$

Lastly, some splitting is visible in the tracks due to the initial parameters $M_{1,0}$, $M_{2,0}$ and the initial orbital period P_0. The results of these parameters are shown in Figure 4.2 which is a plot similar to Figure 4.1 but color graded according to the initial parameters. The initial major splitting happens due to the initial donor mass as seen in Figure 4.2A. These tracks are then further bifurcated by the initial orbital period as seen in Figure 4.2B which then concludes with an even finer bifurcation with respect to the accretor mass in Figure 4.2C. Change in the initial orbital period will of course have a direct consequence on the initial orbital separation as $a^3 \propto P^2$. Thus, it influences how evolved the donor can become before magnetic braking has had time to tighten the orbit and the initial mass transfer phase is initiated. This is important for the rest of the evolution as highlighted previously. The accretor has the same consequence, although more subtle. Increasing the accretor mass will increase the orbital separation for a fixed period as $a^3 \propto (M_1+M_2)$. However, it will also decrease the Roche lobe radius through (2.2.2), and it will therefore both delay and urge the time it takes for the initial mass transfer to initiate, resulting in finer splitting. The major splitting due to the donor mass happens as the He-core evolution is strongly dependent on the initial mass.

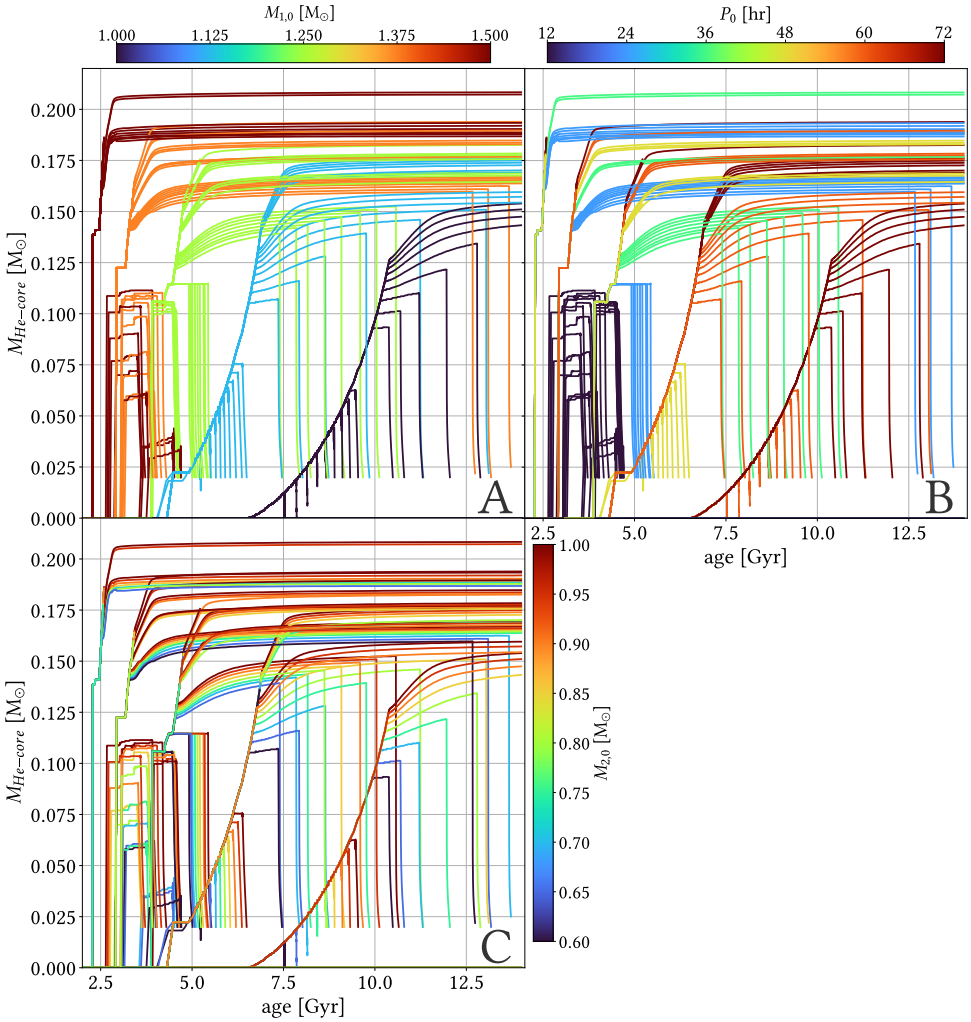

Figure 4.2: Plots showing the evolution of the He-core mass for the initial grid search with respect to time. In A the tracks are colored according to the initial donor mass, B is colored according to the initial orbital period and C is colored according to the initial accretor mass.

4.1.2 Strain Evolution

Figure 4.3 shows a plot of the strain evolution for the 270 grid systems. The tracks are color graded according to the maximum He-core mass each donor gets during its evolution. The brown systems on the plot represent systems which do not develop a He-core and thus becomes brown dwarfs after the initial mass transfer phase. These also never reach the secondary mass transfer phase and originate from the lower end of the donor masses chosen (1 $M_\odot$ and 1.125 $M_\odot$) with shorter orbital periods. As a result, these donors initiate mass transfer before developing a He-core and loose enough mass for hydrogen burning to slow down significantly, preventing the formation of a helium core. The importance of a developed He-core, when it comes to detectability in the GW spectrum, is further highlighted here. As can be seen in Figure 4.3 the more massive the He-core becomes during its evolution the higher the characteristic strain, with systems reaching ~100 times stronger strain amplitudes than the shifted LISA sensitivity curve for edge-on binaries. These are systems which have a very tight orbit with $f_{gw} \sim 6 \times 10^{-3}$ Hz corresponding to an orbital period of $P \approx 5.5$ min. However, as previously mentioned with respect to Figure 4.1, this He-core mass "rule of thumb", only works up to a limit, where for the larger He-core masses the systems detach and GW radiation is not strong enough to bring the orbit in. These systems are the darker blue

tracks, ending their evolution at around $f_{gw} \sim 2 \times 10^{-5}$ Hz with a period of $P \approx 28$ hrs. In the same area some systems seems to curl around a gain a higher GW frequency. These stem from the previously mentioned edge cases, where if given a bit more time, they would end up as compact binaries. The systems which become detectable all lie in the range of max He-core masses of about $[0.075, 0.16]$ $M_\odot$, although the lower limit is only for very near face-on binaries, as these just barely peak over the sensitivity curve for LISA at 1 kpc. The peak systems have a max He-core mass above 0.125 $M_\odot$.

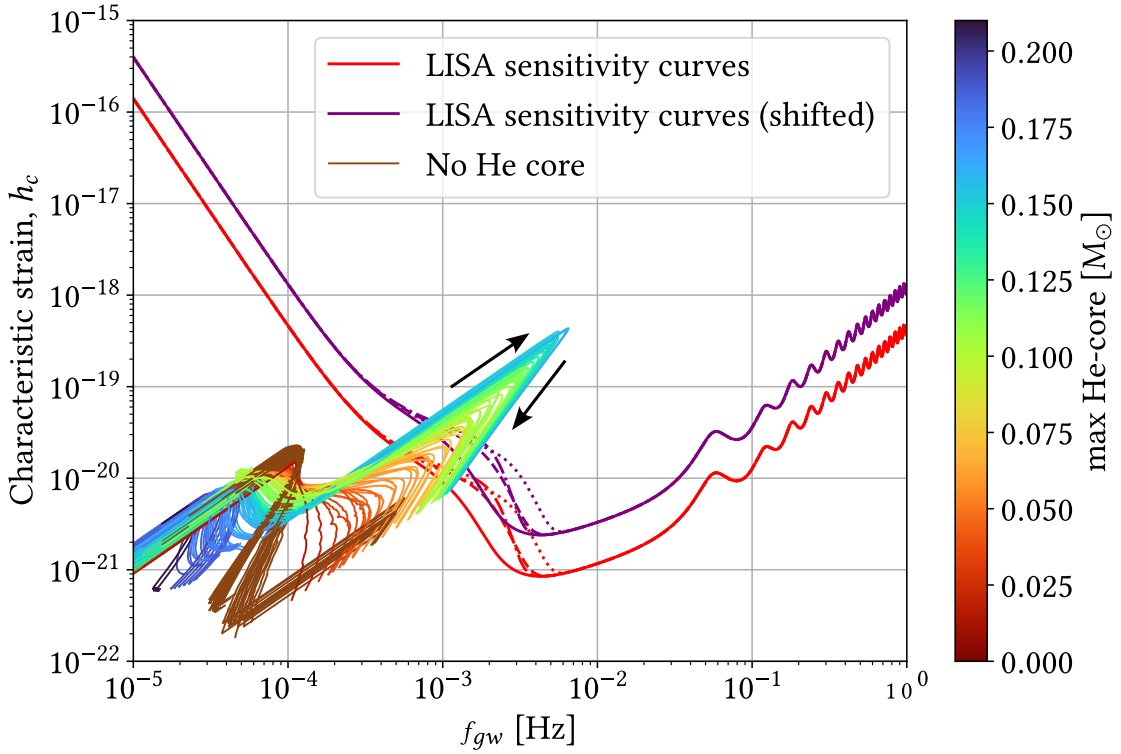

Figure 4.3: Plot showing the characteristic strain amplitude evolution of the initial grid systems. Tracks are color graded with respect to the maximum He-core mass the donor reach during the evolution. The brown tracks represents donors which do not develop a helium core. The strain amplitude is calculated assuming 4 years of observation time and face-on binaries. The sensitivity curves for LISA have been made in accordance with those of Figure 2.10.

4.1.3 HR - Evolution

The evolution of the donors from the initial grid on an Hertzsprung–Russell (HR) diagram is shown in Figure 4.4. Here the tracks are color graded according to the He-core mass during it's evolution thus highlighting similar features as in Figure 4.1 as to where the initial core development happens and later where the core starts loosing mass due to the secondary mass transfer phase. The black plus signs on the plot shows where the the surface gravity, g, becomes larger than 10^6 cm s^{-1}, marking the point were `MESA` considers the donor to have entered the white dwarf cooling track. Furthermore, $\sim$ 1000 white dwarfs from the Montreal White Dwarf Database (MWDD), (Dufour et al., 2017), has been plotted in gray for reference within the HR diagram. Only the reported values from the MWDD are shown, as uncertainties are mostly not provided by the database. Out of these, only the ones with estimated masses, and a luminosity lower than 0.1 $L_\odot$ has been included in the plot as these was most comparable to our evolutionary tracks. Although, in general they are still more massive than what our simulations yield, with a mean of 0.610 $M_\odot$ and a minimum and maximum mass of 0.096 $M_\odot$ and 1.32 $M_\odot$, respectively. Thus

they have smaller radii and therefore lies lower on the cooling track. In order to highlight the nature of the cooling tracks, the dashed black lines have been plotted, which represent the black body cooling lines given by,

$$L = 4\pi R^2 \sigma T^4, \tag{4.1.7}$$

where $\sigma \approx 5.670 \times 10^{-5}$ erg cm^{-2} s^{-1} K^{-4} is the Stefan–Boltzmann constant. The dashed lines, from lowest to highest in the HR diagram, have been made assuming radii of $R = [0.005, 0.01, 0.02, 0.04]$ $R_\odot$. As previously mentioned only the systems which develops a He-core with a mass in the range of about $[0.125, 0.16]$ $M_\odot$ becomes strongly detectable AM CVns in the GW spectrum, even for edge-on binaries. In Figure 4.4 these systems are the tracks which becomes blue before curving down onto the cooling track and later becomes green as the now exposed core has become a degenerate object which is losing mass in the secondary mass transfer phase. The red tracks are the previously mentioned systems which never develop a He-core and thus never become compact binaries. The purple track represent the higher mass He-cores, and thus higher mass white dwarf, which never reach the secondary mass transfer phase.

Some of these systems also undergo hydrogen shell flashes after the initial mass transfer phase. As the donor becomes more compact its surface temperature rises until it becomes hot enough to ignite the hydrogen in its envelope. This ignition causes a spike in energy production which result in a expansion of the star's radius which consequently causes the star to become brighter. This cycle repeats a couple of times over a short period of time causing this looping pattern on the HR diagram. This behavior can also be seen in Figure 4.5, where an example of one of these systems is plotted. Here the power generated by each fusion process is shown in a Kippenhahn diagram, all with respect to the model number to better highlight the features associated with this phenomena, as it happens on a short timescale. For reference, the two peaks in CNO are 40 Myrs apart. Here, the two peaks in energy production right before the radius increase is clearly seen.

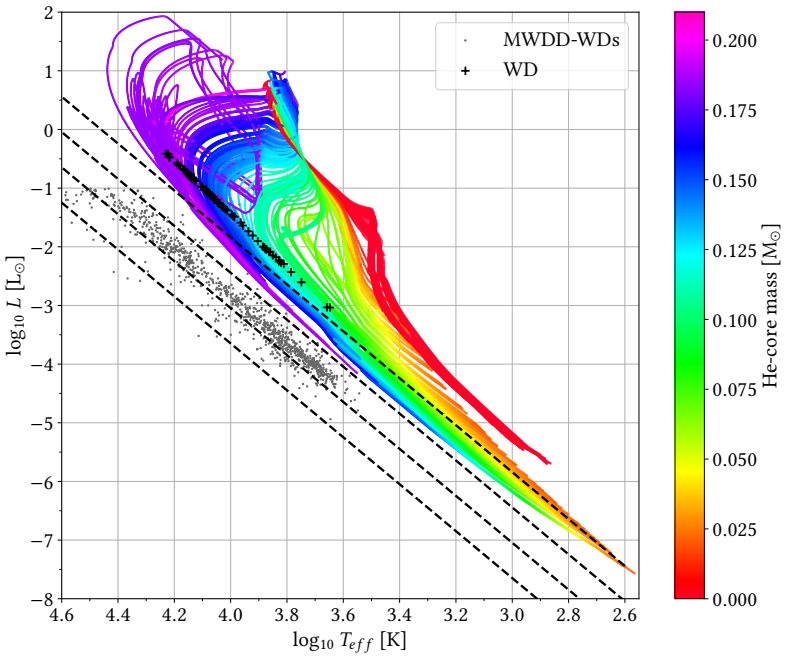

Figure 4.4: HR diagram of the initial grid search color graded according the the He-core mass. The black plus sign symbolizes where the surface gravity for the donor of the individual track becomes larger than 10^6 cm s^{-2}. The dashed lines are the black body cooling lines for $R = [0.005, 0.01, 0.02, 0.04]$ $R_\odot$. The gray dots are white dwarf taken form Dufour et al. (2017). Further explanation in main text.

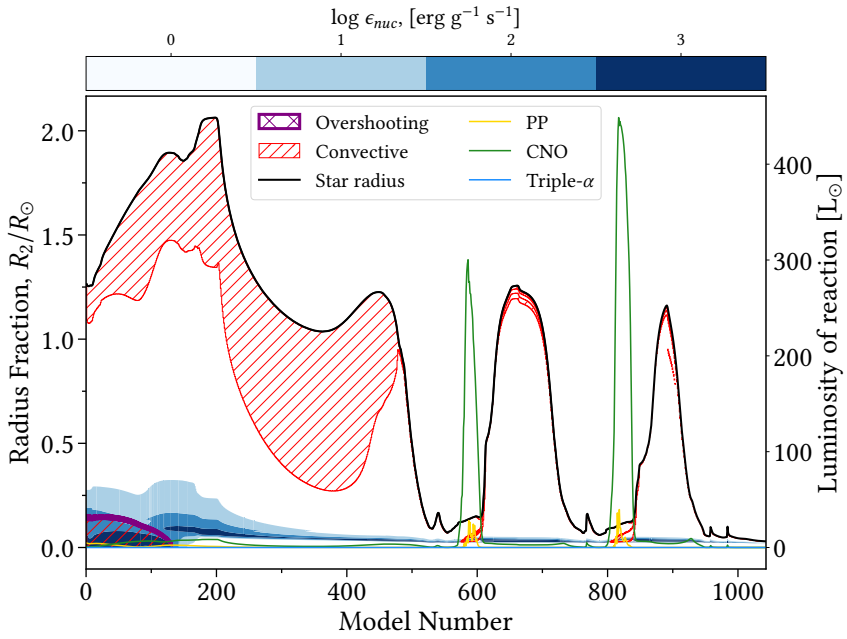

Figure 4.5: Power of fusion reactions plotted on top of a Kippenhahn diagram, with respect to model number of a system which undergo hydrogen shell flashes. The starting parameters for this systems is; $M_{2,0} = 1.5$ M$_\odot$, $M_{1,0} = 0.9$ M$_\odot$ and $P_0 = 1.0$ day.

Figure 4.6 shows similar plots like Figure 4.4 using different color mappings. Here Figure 4.6A is color graded according to the surface gravity, g, highlighting similar features as in Figure 4.4 where the more massive and thus more compact WD donors are located deeper in the cooling track on the HR diagram due to the inverse mass-radius relation. Figure 4.6B is colored according to the surface hydrogen fraction. The red area here shows where the fraction becomes approximately zero and thus where the accreted material is dominated by helium. Thus, within this red region we expect to find AM CVns, given accretion. This area will be discussed in greater resolution later, when comparing our data to observations. Figure 4.6C shows the mass transfer rate from the donor to the vicinity of the accretor. Here, detached periods are shown in brown. This also highlights the systems which develop high He-core masses and have this detached period, where the larger ones never initiate the secondary mass transfer phase. Some systems never completely detach either, although the mass transfer rate becomes about 100 times lower than during the main mass transfer phases. The location of these two main mass transfer phases is highlighted in blue with mass transfer rates around 10^{-7} M$_\odot$ yr^{-1}. Here the AM CVn phase can be inferred to be between the two highest black body cooling lines at around a T_{eff} between $10^{3.6}$ K and 10^3 K. Here, the donor has a high surface gravity, $g \approx 10^{6.5}$ cm s^{-2}, as seen in Figure 4.6A and has little to no hydrogen on the surface. Furthermore, the orbital period, as seen in Figure 4.6D, is lower than 1 hr in this area and goes as low as around 6 min for the more compact donors. Figure 4.6D also draws attention to systems which grow significantly in period during the initial mass transfer phase, most easily seen for the system which does not develop a He-core. For the rest of the systems, the period shrinks gradually or has a rapid decrease as can be seen for the more compact donors around $T_{eff} = 10^{3.9}$ K and $L = 10^{-2}$ L$_\odot$. This period evolution will be discussed in the next section.

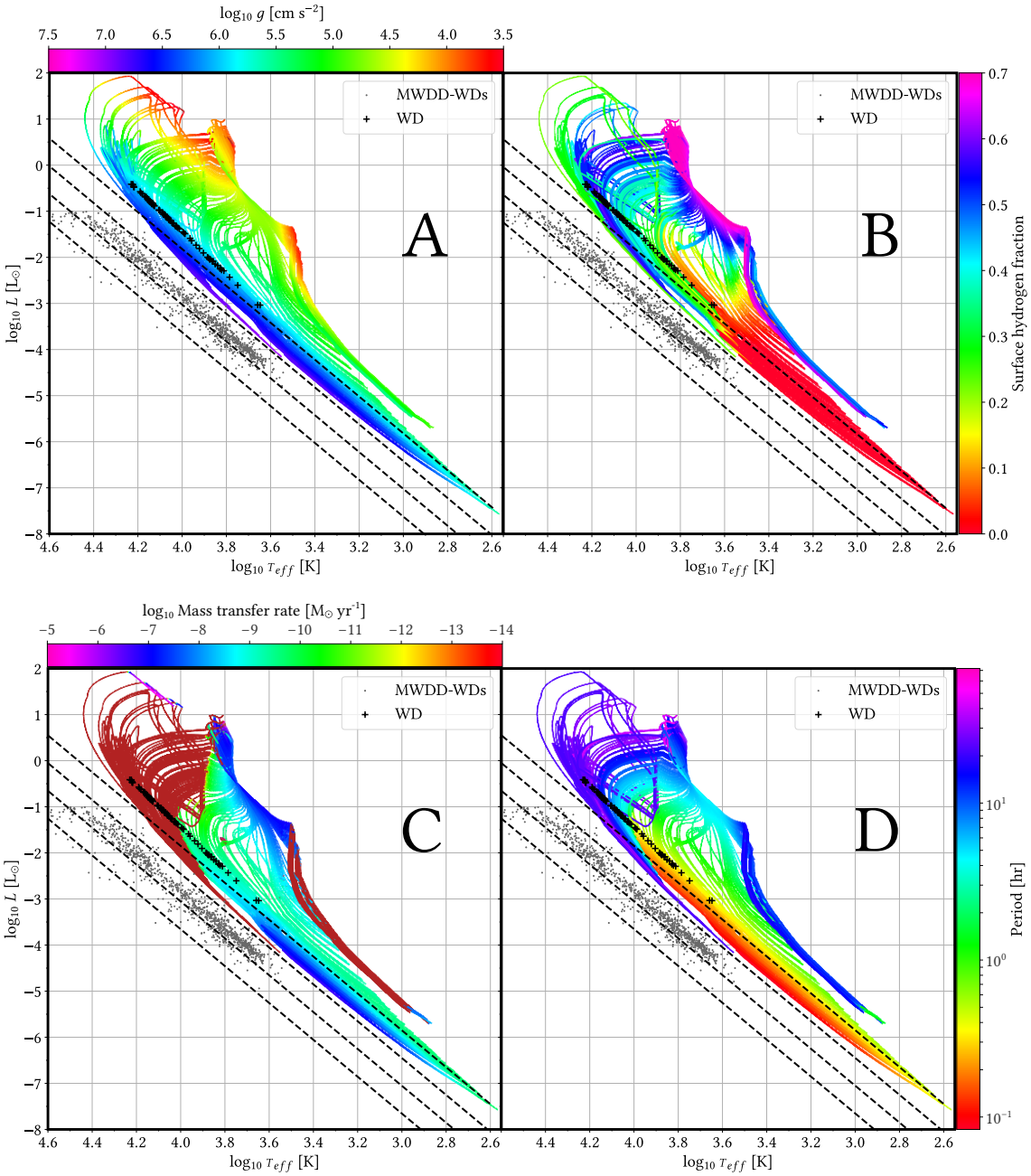

Figure 4.6: HR diagrams of the initial grid search color graded according surface gravity (A), surface hydrogen fraction (B), mass transfer rate (C) and orbital period (D). The black plus sign symbolizes where the surface gravity for the donor of the individual track becomes larger than 10^6 cm s^{-2}. The dashed lines are the black body cooling lines for $R = [0.005, 0.01, 0.02, 0.04]$ R$_\odot$. The gray dots are white dwarf taken form Dufour et al. (2017). Further explanation in main text.

4.2 Diverging, Intermediate and Converging Systems

In terms of the period evolution, we have 3 different types of systems; diverging, intermediate and converging. The first is systems which obtains a greater orbital period than they initially started off with. Intermediate systems end up with roughly the same period as they started out with, and converging systems evolve towards shorter periods and eventually reach a period minimum, before it starts to increase again. Examples of these evolutionary tracks can be seen in Figure 4.7, with the blue track being diverging, the orange intermediate and the green converging.

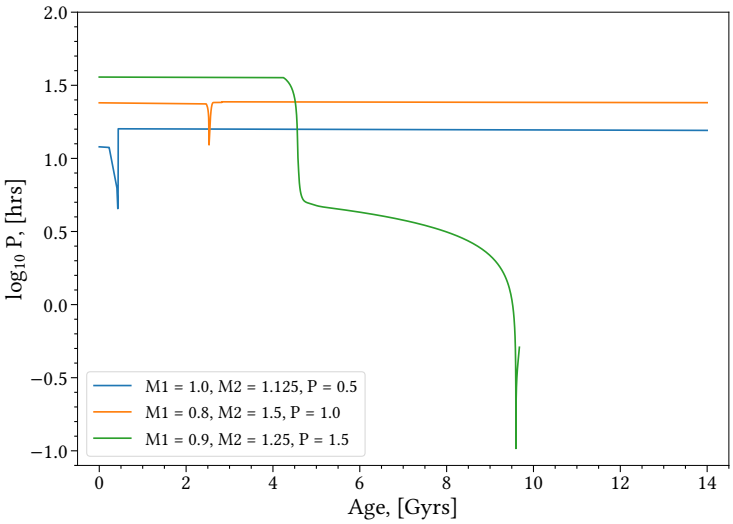

Figure 4.7: The period evolution of 3 selected systems. One which is diverging (blue), another where the period of the system stays roughly the same (orange), and lastly on which is converging (green).

In order to gain insight as to why these systems evolve as they do, we investigate the structure of the donors and see how these evolve. A powerful tool for this is Kippenhahn diagrams. Three of which can be seen in Figure 4.8. They give valuable information about the nuclear burning regions and energy transfer zones such as convective regions. Note that in the areas which have not been marked by a hatched region, the star has radiative energy transfer. This only applies within the boundary of the star, which is given by the black line. Furthermore, it is helpful to plot the structure of the donor in terms of the model number. This allows for better resolution, as more models and smaller timestep are used whenever large changes happen in our simulations.

In Figure 4.8 it is immediately apparent that the diverging and intermediate systems do not experience a secondary mass transfer phase and are detached following the initial mass transfer. These initial mass transfer phases are related to the two sharp drops in the period in Figure 4.7. However, the converging system experiences a secondary mass transfer phase, following a detached phase, where only the helium core is left, thus we have an AM CVn.

Furthermore, it can be seen that the donor in the diverging system becomes fully convective towards the end of mass transfer, but only has a convective envelope at the start of the evolution. The core is also slightly convective in the beginning, but it quickly becomes radiative. In the intermediate and converging systems, the donors core remains convective for longer. This is because they have a larger initial mass and thus the CNO cycle becomes prominent. Only once shell burning starts, does the cores become radiative, as is also evident from Figure 4.8. This takes approximately 2 Gyrs and 4 Gyrs for the intermediate and converging system respectively (see Figure B.2). The size of the convective envelope of the intermediate system is seen to increase during mass transfer. This has a dramatic effect on MB as the model scales with the convective turnover time. To better highlight this effect, the orbital angular momentum losses, due to the different mechanisms, are plotted in Figure 4.9.

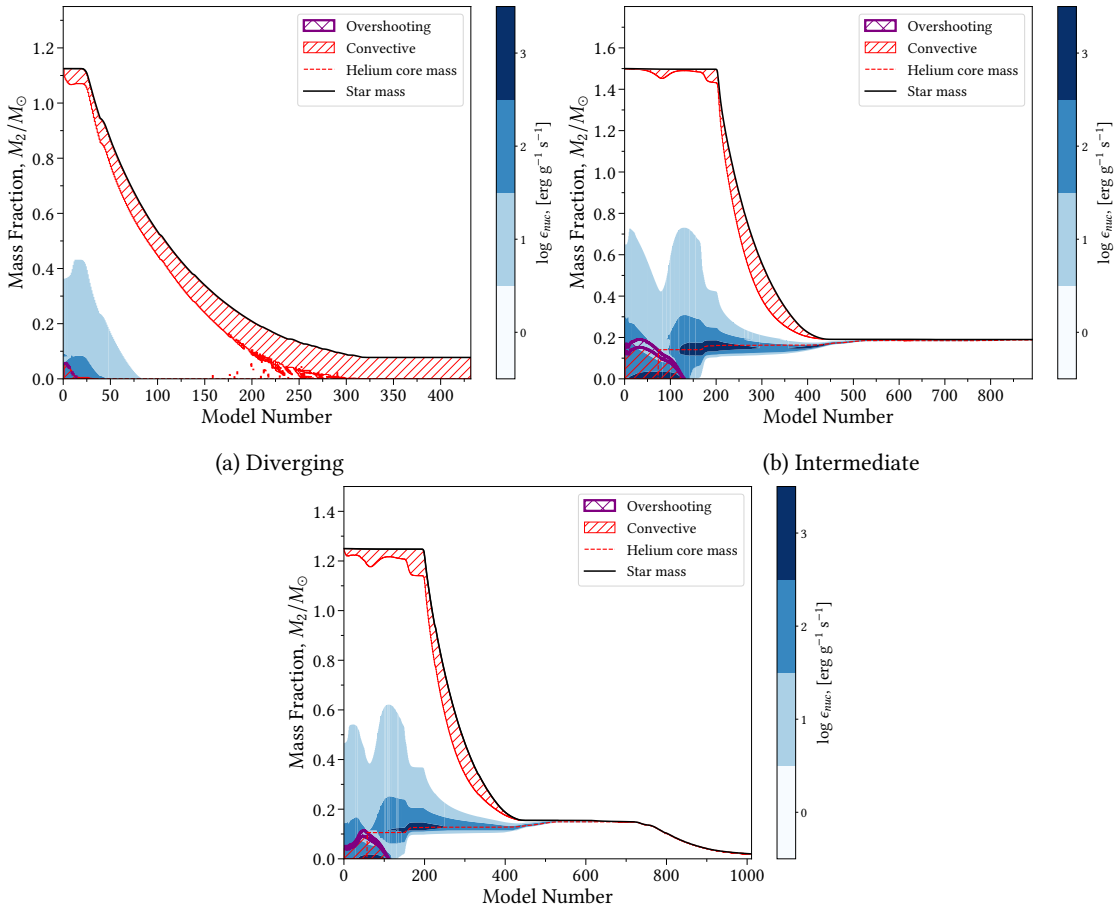

(a) Diverging

(b) Intermediate

(c) Converging

Figure 4.8: Kippenhahn diagrams showing the structure of the star in terms of mass fraction and model number, for the diverging (top left), intermediate (top right) and converging system (bottom).The blue areas are the burning regions of the star. A color scale is seen to the right corresponding to the logarithm of the energy generation from fusion processes.

Figure 4.9 shows the evolution of these systems with respect to the orbital angular momentum loss due to $\dot{J}_{mb}$ (blue), $\dot{J}_{ml}$ (green) and $\dot{J}_{gwr}$ (orange). In all systems MB does not turn on at the start, which is explained by the initial convective core, as previously discussed. For the divergent system, in Figure 4.9a, orbital angular momentum loss due to MB is completely lost, at around model number 330, and it is therefore not able to maintain its high mass transfer rate, as seen from the sudden drop in $\dot{J}_{ml}$. At this point the donor is very low mass, compared to the accretor, which results in the system evolving in accordance with system with very low mass ratios in Figure 2.4, thus widening the orbit. This loss of MB is due to the loss of a radiative core as shown in the Figure 4.8a. The Kippenhahn diagram also explains the dramatic discontinuities in MB, due to the star becoming fully convective in a slightly unsystematic way. The convergent system in Figure 4.8c has a clear detached phase as seen from the low stretch in angular momentum loss due to MB and ML, while $|\dot{J}_{gwr}|$ increases, indicating that the orbit is tightening. The intermediate system in Figure 4.8b does not show the same pattern in angular momentum loss due to GWR. However, a clear increases in both $\dot{J}_{mb}$ and $\dot{J}_{ml}$ can be seen around model number 690. This can be explained by a sudden hydrogen shell flash when investigating the Kippenhahn diagram with respect to the radius (see Figure 4.10).

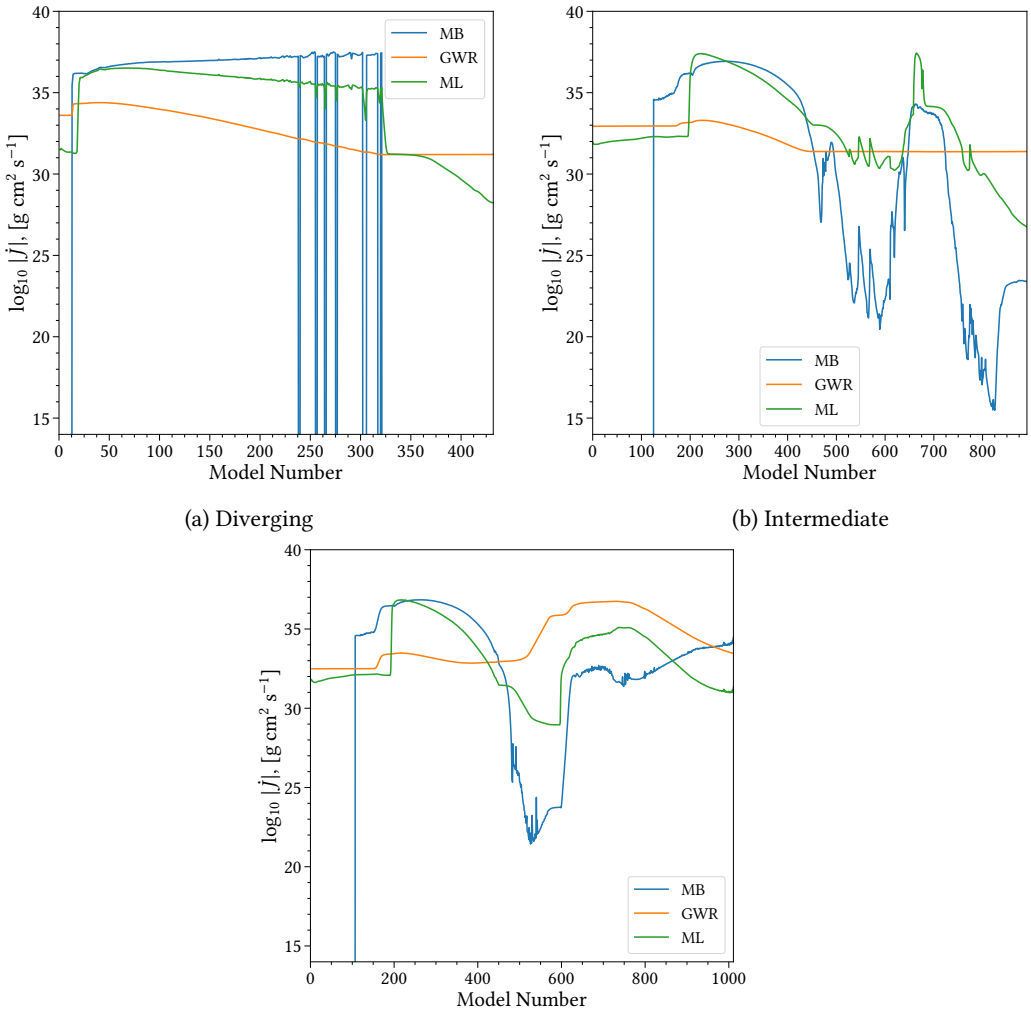

(a) Diverging

(b) Intermediate

(c) Converging

Figure 4.9: The angular momentum loss caused by MB, GWR and ML, for the diverging (top left), intermediate (top right) and converging system (bottom).

Finally, we also present the Kippenhahn diagrams showing the radius evolution of the donors throughout the evolution of these systems seen in Figure 4.10. For comparison sake we have also plotted the Kippenhahn diagrams for these systems in terms of age, they can be seen in Figure B.3. For the converging system in Figure 4.10c, a small convective envelope is still present when only the helium core is left, which is also the reason why the MB is so weak during this phase. The reason why it increases again is that the second mass transfer phase causes the donor to gain a larger convective envelope. This is seen around model number 900–1000. For the diverging system in Figure 4.10a, it can be seen that its radius shrinks as the core burning becomes weaker, and afterwards it increases until mass transfer comes to a halt, causing the donor to shrink. Furthermore, the unsystematic convective zones are more clearly seen here, causing the sudden discontinuities in MB. For the intermediate (Figure 4.10b) and converging systems, the radii shrinks more dramatically, than for the diverging system, as the donor loses mass. When mass transfer stops, the stars contract as they stop hydrogen burning and only the helium core is left (see Figure 4.8). The reason why mass transfer is possible even though the radii shrink is due to MB, as the donor contract, the binary is also brought closer together. This is especially relevant for the converging system, where the radius of the donor does not increase towards the end of mass transfer. The reason why the radius of the donor in the intermediate system increases again, is related to the deep convective

envelope it obtains around model number 350. An interesting feature is also seen for the intermediate system where a flare up in the radius occurs due to a shell flash (see also Section 4.1.3). Here, a small convective envelope is formed causing the peak in MB in Figure 4.9b. This also brings the system slightly together and, along with the sudden expansion in radius, this causes an increase in mass transfer, as seen from the peak in $\dot{J}_{ml}$.

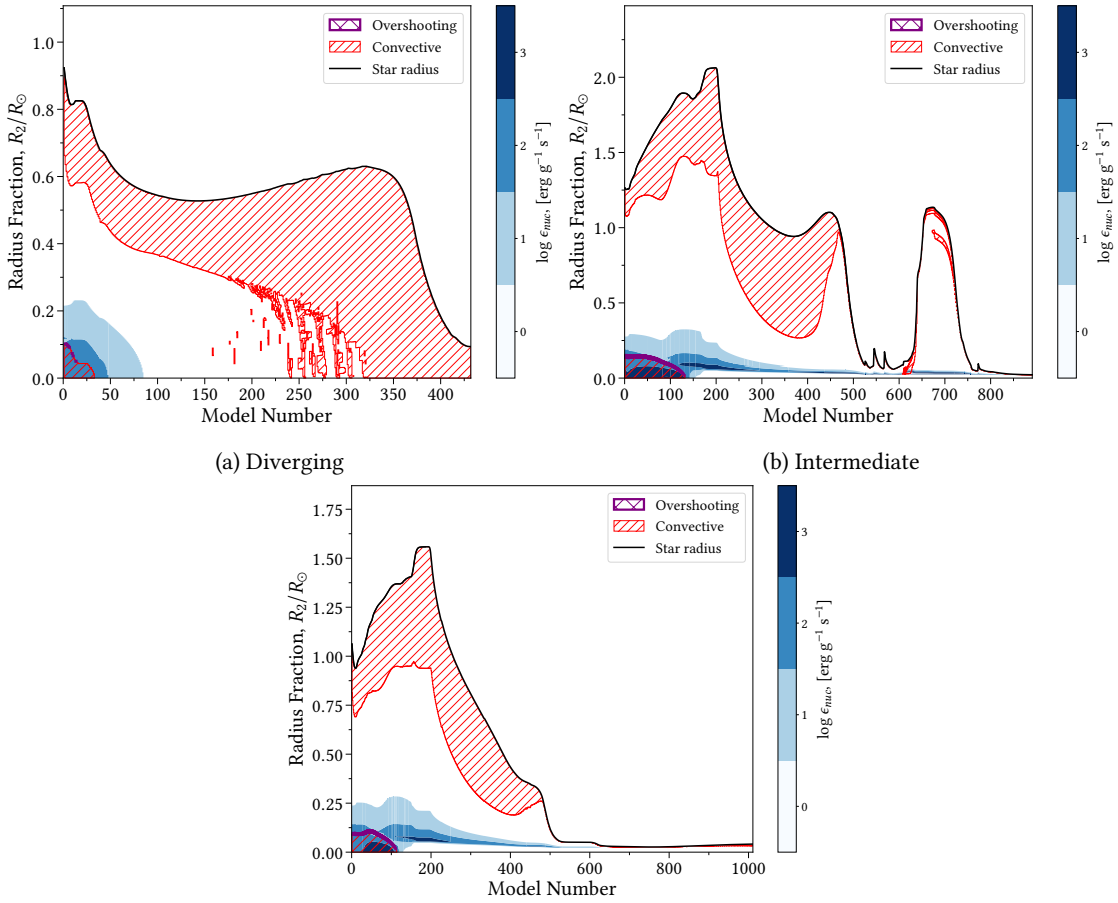

(a) Diverging

(b) Intermediate

(c) Converging

Figure 4.10: Kippenhahn diagrams showing the structure of the star in terms of radius fraction and model number, for the diverging (top left), intermediate (top right) and converging system (bottom). The blue areas are the burning regions of the star. A color scale is seen to the right corresponding to the logarithm of the energy generation from fusion processes.

In summary, diverging systems diverge as they do not experience enough MB to counteract the expansion of the orbit caused by mass loss (see Section 2.2.2). The reason why this system do not attain substantial MB is because the donor does not develop a helium core before mass transfer starts, which leads to it becoming fully convective. The intermediate system attains substantial MB, but the donor evolved too quickly creating a larger He-core. Hence, when it had been stripped down to this He-core the larger mass lead to a larger orbital separation, which in turn means that the system could not be brought close enough together to initiate mass transfer again within 14 Gyrs. This is also seen when comparing $\dot{J}_{gwr}$ in Figure 4.9b to Figure 4.9c, where it is two orders of magnitude lower for the intermediate system compared to the converging system, in the detached phases. The intermediate system becomes detached after the hydrogen shell flash. The converging system here attains a radiative core and convective envelope for a good amount of time before mass transfer, making MB possible for a longer duration (see Figure 4.8).

Thus, MB is able to substantially shorten the period of the system which is clearly seen in Figure 4.7.

As is also evident from this analysis, the initial periods and masses have a huge influence on how these systems evolve. They determine how the donor in our simulated systems evolves, and thus whether they become diverging, intermediate, or converging. We are mostly interested in the converging systems, as it is these which become AM CVns. Therefore, we want to know which initial condition favors this outcome.

4.3 Fine Grid Results

In order to better visualize the consequences of the initial parameter choices, a finer grid search is made within the ranges of the initial grid, which evolve into AM CVns. These simulations are also simulated further down to a minimum mass of 0.005 $M_\odot$, to to gain more information about the AM CVn phase. Here, three sets of simulations are made where either $M_{1,0}$, $M_{2,0}$ or P_0 is varied and the rest kept constant. In Figure 4.11, $M_{1,0} = 0.7$ $M_\odot$ and $P_0 = 1.0$ days are kept constant while $M_{2,0} \in [1.2, 1.4]$ $M_\odot$ is the variable. The plot is color graded according to the initial donor mass $M_{2,0}$, and the black arrows indicate the direction of the evolution, starting from the right with the higher periods in the initial mass transfer phase. As previously inferred in Section 4.1, these higher mass donor stars have better prerequisites for developing a higher mass He-core and thus a detached phase which then potentially leads to a tight AM CVn, if the system initiates mass transfer again. This is also seen in Figure 4.11 where the red and green tracks, $M_{2,0} \sim [1.2, 1.3]$ $M_\odot$, never becomes detached, as opposed to the pink and purple tracks, $M_{2,0} \sim [1.375, 1.4]$ $M_\odot$ which are systems that never initiate the secondary mass transfer phase. Of the systems, which becomes AM CVns, this conclusion, that a higher mass donor leads to a tighter AM CVn, is also seen. These lead to the lowest orbital period in the secondary mass transfer phase stemming from a donor mass of $M_{2,0} = 1.35$ $M_\odot$ and the slowest having an initial donor mass of $M_{2,0} = 1.2$ $M_\odot$.

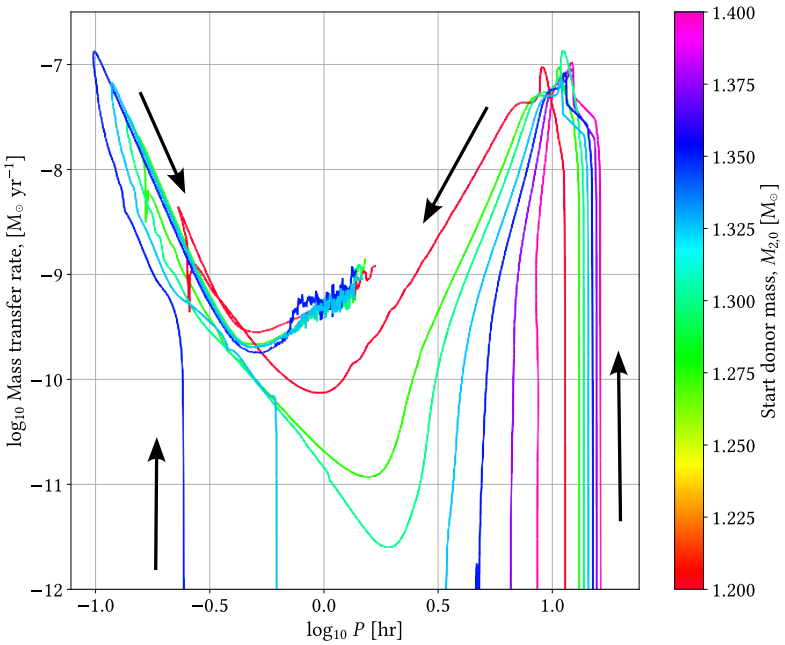

Figure 4.11: Evolutionary track showing mass transfer rate as a function of period for varying $M_{2,0}$ in the range $[1.2, 1.4]$ $M_\odot$. $M_{1,0} = 0.7$ $M_\odot$ and $P_0 = 1.0$ days. Black arrows indicate the direction of the evolution on the plot, starting from the longest periods. The lines are color graded according to the initial donor mass.

In Figure 4.12 similar tracks as to Figure 4.11 have been plotted with respect to a varied period in A and a varied accretor mass in B. Both A and B have an initial donor mass $M_{2,0} = 1.25$ $M_\odot$. In A the period is varied in the range $P_0 \in [0.5, 1.5]$ days and the accretor mass is kept at $M_{1,0} = 1.0$ $M_\odot$ whereas in B the initial period is kept at $P_0 = 1.0$ days and the accretor mass is varied in the range $M_{1,0} \in [0.85, 1.0]$ $M_\odot$. Figure 4.12A shows that increasing the initial orbital period yield more compact AM CVns, where for $P_0 > 1.2$ days the binary gains a detached phase. This again hints at systems which are allowed to develop a larger He-core becoming more well defined and detectable AM CVns, as the larger period results in a later initial mass transfer phase. The same argument can be used for Figure 4.12B where as the more compact AM CVns stem from higher accretor masses. As the initial period and initial donor mass is kept constant in these runs, a higher initial accretor mass results in a longer initial orbital separation and thus giving the donor more time to evolve before the initial mass transfer phase starts, as previously seen in Figure 4.2.

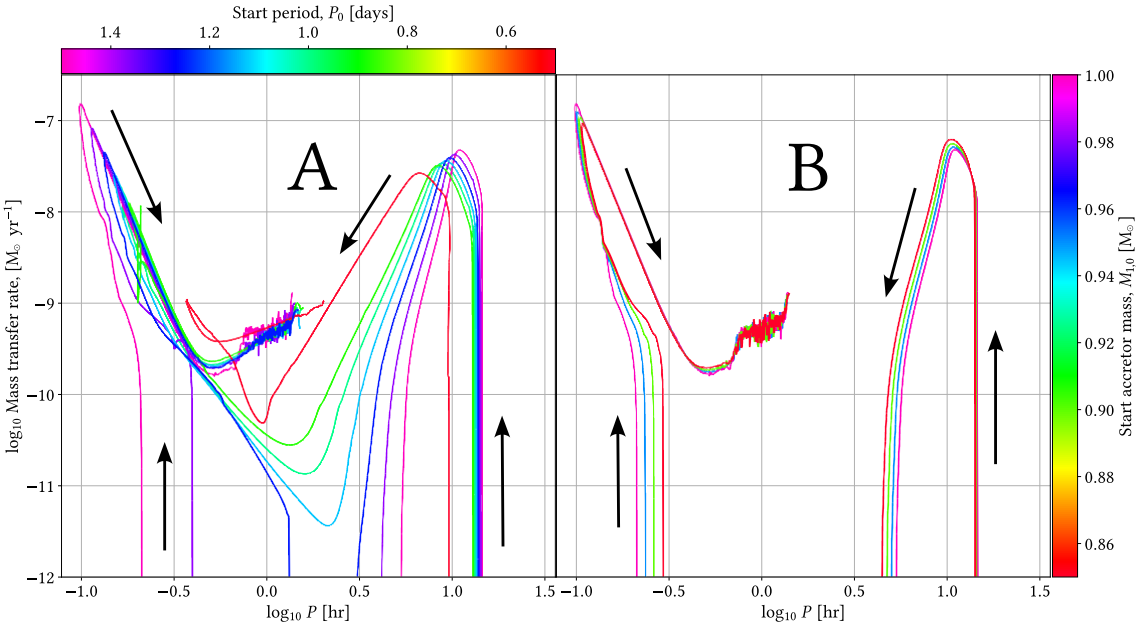

Figure 4.12: Evolutionary track showing mass transfer rate as a function of period for varying P_0 in the range $[0.5, 1.5]$ days for plot A and varying $M_{1,0}$ in the range $[0.85, 1.0]$ $M_\odot$ for plot B. $M_{2,0} = 1.25$ $M_\odot$ in both A and B. $M_{1,0} = 1.0$ in A and $P_0 = 1.0$ days in B. Black arrows indicate the direction of the evolution on the plot, starting from the longest periods. The lines are color graded according to the initial period in A and initial accretor mass in B.

This dependency on initial orbital separation can be seen in Figure 4.13 where by combining Figure 4.12A and B, and color grading according to a_0 it can be seen that the lager a_0 the more compact the AM CVn becomes. Here, the initial orbital separation is in the range $a_0 \in [3.475, 7.23]$ $R_\odot$, whereas the 4 systems from Figure 4.12B contributes with the longest separations form 7.06 $R_\odot$ to 7.23 $R_\odot$. This example also highlights the sweet spots in initial parameters which results in donors which evolve in a suitable time frame. In this example, we find the sweet spot for donors of mass $M_{2,0} = 1.25$ $M_\odot$. As previously mentioned, a donor mass which is too high leads to high He-core masses which never initiate the secondary mass transfer phase, as opposed to the donor masses that are too low which may take too long to evolve. Thus, this window of initial orbital separations is highly dependent on the initial donor mass, as the donor's nuclear evolution must align with the timescale of the orbital decay via angular momentum loss. For which the most important contributor before and during the initial mass transfer phase is magnetic braking. In extension, this further highlights the importance of choice of magnetic braking

models. For a weaker model the sweet spot for succesfully producing AM CVns becomes narrower, as the initial post-CE binary needs to be closer together in order to align orbital decay with the donor's nuclear evolution. However, as magnetic braking scales strongly with the donors rotation rate, the acceleration of the orbital decay in these narrower synchronized binaries is also greater, making the post-CE period with approximately steady magnetic braking shorter. This in turn makes the initial parameter space for systems which becomes AM CVns smaller as the nuclear evolution might take to long for smaller mass donor stars for a weaker magnetic breaking model.

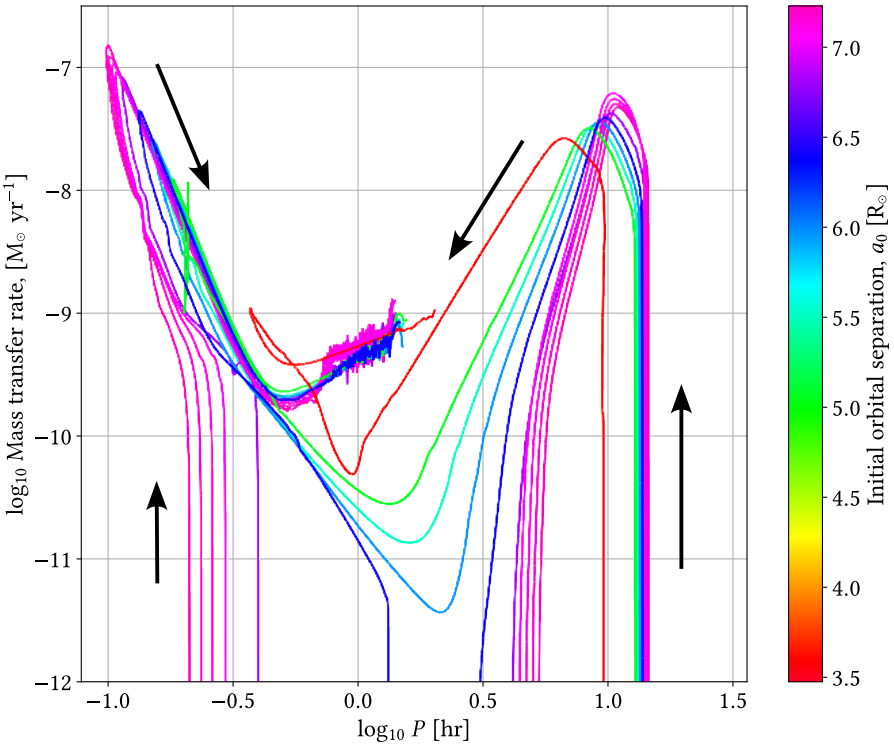

Figure 4.13: Evolutionary track showing mass transfer rate as a function of period for varying a_0 in the range $[3.475, 7.23]$ $R_\odot$, by combining Figure 4.12A and B. $M_{2,0} = 1.25$ $M_\odot$. Black arrows indicate the direction of the evolution on the plot, starting from the longest periods. The lines are color graded according to the initial donor mass.

4.4 Comparison With Observational Data

To validate our simulations we have gathered some observed systems to compare with (see Section 3). However, not all of our simulated systems end up as potential AM CVn candidates, therefore we have chosen a conservative limit for the minimum period of $P < 2$ hrs, for the systems we like to compare with the observed systems. This range has been chosen as AM CVns have periods ranging from 5 to 65 minutes (Solheim, 2010).

Some of the most important aspects of classifying AM CVns are the hydrogen abundance in their spectra, as their spectra are dominated by helium and thus we expect low hydrogen abundances. Furthermore, surface gravity is a valuable parameter as it gives us measure of how compact the donor is. In Figure 4.14 we have plotted how the masses of the donors in our different systems evolve with orbital period, and what the surface hydrogen fraction and surface gravity are along these tracks.

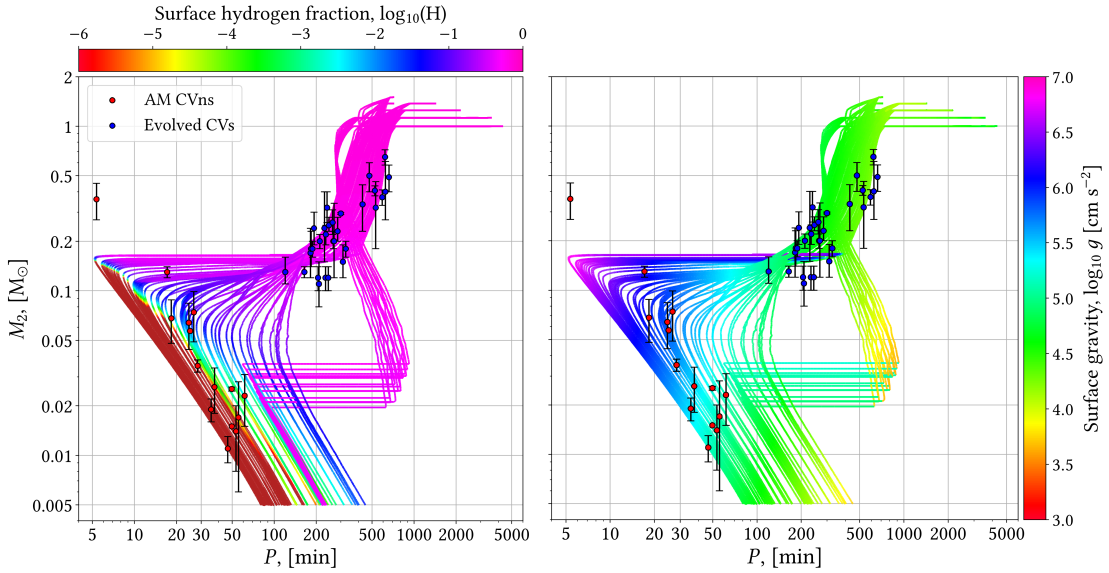

Figure 4.14: The donor mass in terms of the period of our simulations, which reach periods $P < 2$ hrs. Two color scales have been used, one for the surface hydrogen abundance (left) and one for the surface gravity (right) of the donor. The observational data for the AM CVns and evolved CVs has been plotted as red and blue dots respectively, along with known errors. The brown color indicate a surface hydrogen fractions lower than 10^{-6}.

All the tracks start in the upper right corner and initially evolve towards shorter periods, some during mass transfer as we see that the mass decreases along with the period. The systems with lines that become horizontal have a detached phase, where only the period decreases, as can be seen to the right in Figure 4.14, this gives the donor time to contract and become more compact. The higher mass donors which enters this phase becomes degenerate, as indicated by the surface gravity. Once these systems reach their period minimum, they exhaust all of their hydrogen and become He WDs. A group of systems to the right in these plots have increasing periods as the initial mass transfer takes place, but they later become detached before reaching their period minimum. However, these systems do not have a substantial fraction of their hydrogen stripped as seen to the left in Figure 4.14. Although these systems also attain higher surface gravity during their detached phase, they do not exceed $g \simeq 10^6$ cm s^{-2}, where MESA assumes the donor to be in the WD cooling sequence. In fact, these systems become brown dwarfs, which are stripped down to planet-like objects.

Some of the systems that do not become fully detached, also get all their hydrogen stripped, but they

also do not attain surface gravities exceeding $g \simeq 10^6$ cm s^{-2}. However, some attain values near this limit, hence we see these systems as semi-degenerate He stars.

In terms of the observed systems we are able to reproduce all but one of the AM CVns, but another also lies in a region for which the surface hydrogen fraction is above ~ 0.1, these systems are HM Cnc and the AM CVn respectively. The most like explanation as to we are not able to reproduce HM Cnc is that it might be formed via another formation channel, mainly the double WD channel, as the mass of the donor is quite large compared to our evolutionary tracks following the CV formation channel (Solheim, 2010). In terms of the AM CVn itself, this might also be the case as it is expected to have a He star donor (Solheim, 2010), but yet again we are not able obtain He star masses suitable for the period of this system, thus this system might be formed through the He star channel following a second CE.

We are also able to reproduce all the observed CV systems (see Figure B.4 in Appendix B), although some of them do not intersect the systems, which obtains a minimum period below two hours. Thus, we can say that these systems do not become AM CVns, following our evolutionary tracks. This is due to too much mass transfer; they do not evolve a helium core of substantial size to be able to obtain periods suitable for the AM CVn classification.

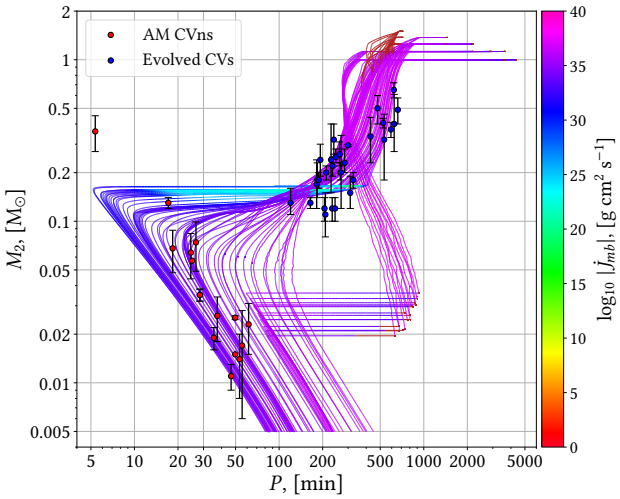

Figure 4.15: The donor mass in terms of the period of our simulations, which reach periods $P < 2$ hrs. The color scale shows the magnetic braking throughout the systems evolution. The observational data for the AM CVns and evolved CVs has been plotted as red and blue dots respectively, along with known errors.

An interesting feature in these systems is the MB throughout the evolution. Looking at Figure 4.15 we see that even though the donor becomes compact or He star, MB still has a significant effect. In the detached systems where the donors become compact objects, it drastically decreases in this phase before increasing again. Not much is known about the dynamo which produces magnetic fields in WDs, but it has been proposed that it is produced as the WD cools (Schreiber et al., 2021). Therefore, we wish to investigate the influence of turning off MB once the donors surface gravity exceeds 10^6 cm s^2 and becomes compact. We have made another set of simulations in which we do this, leading to 3 subsets of simulated evolutionary tracks. Two in which the surface gravity exceeds 10^6 cm s^2 and MB is turned off or kept on, after this point. The last is systems in which the surface gravity of the donor never exceeds 10^6 cm s^2. The following data will be presented in a manner that reflects this.

We also have other data for the observed systems that can be used to compare with our simulation data. Ideally, we would like to be able to reproduce the observed data with respect to all known parameters, to conclude that we are for sure able to reproduce it with our simulations. Plotting the radii of the

donors with respect to their masses, for the systems where the surface gravity of the donor never exceeds 10^6 cm s^2, gives Figure 4.16. Interestingly, we can see that the donors in these systems also become degenerate as the radius starts to increase in response to mass loss. Furthermore, we clearly see that some of these systems are also able to reproduce the observed systems, both with respect to radius and mass, but also in terms of the expected surface hydrogen fraction. However, there is one AM CVn system which we are not able to reproduce with these tracks, slightly under $R_2 \sim 0.05$ at $M_2 \sim 0.02$ and named J0407-0007, thus we move on to the compact systems.

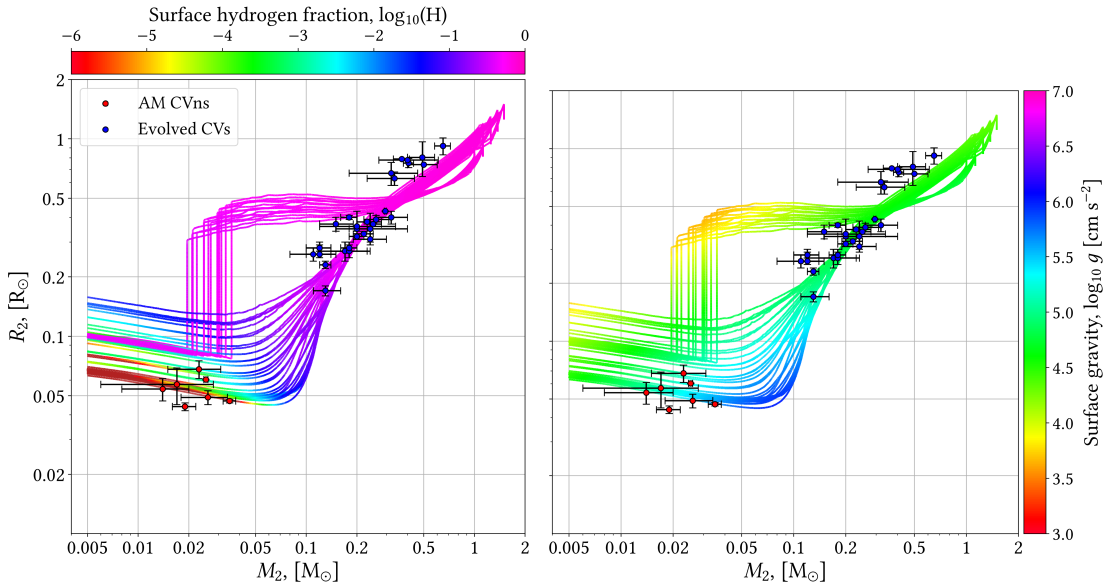

Figure 4.16: The donor radius in terms of its mass for our simulations, which reach periods $P < 2$ hrs, and the surface gravity of the donor never exceeds 10^6 cm s^2. Two color scales have been used, one for the surface hydrogen abundance (left) and one for the surface gravity (right) of the donor. The observational data for the AM CVns and evolved CVs has been plotted as red and blue dots respectively, along with known errors. The brown color indicate a surface hydrogen fractions lower than 10^{-6}.

In Figure 4.17 and Figure 4.18 we have plotted these systems in terms of surface hydrogen fraction and surface gravity, respectively. Now we can reproduce J0407-0007, but can no longer reproduce two other AM CVns, named J0003+1404 and J1637+4917, which we where able to in Figure 4.16. However, this ends up being a quite nice result as we can say that J0407-0007 most likely has a WD donor, whereas J0003+1404 and J1637+4917 most likely have helium star donors, considering the surface hydrogen fraction and the surface gravity.

Looking at the previous discussed figures (Figure 4.16,Figure 4.17 and Figure 4.18) in is seen that we are able to reproduce most of the evolved CVs. There are also some that we do not intersect at all, with our simulations, for example a few with donor masses of just above 0.1 M$_\odot$. We also do not intersect these later in Section 4.4.1.

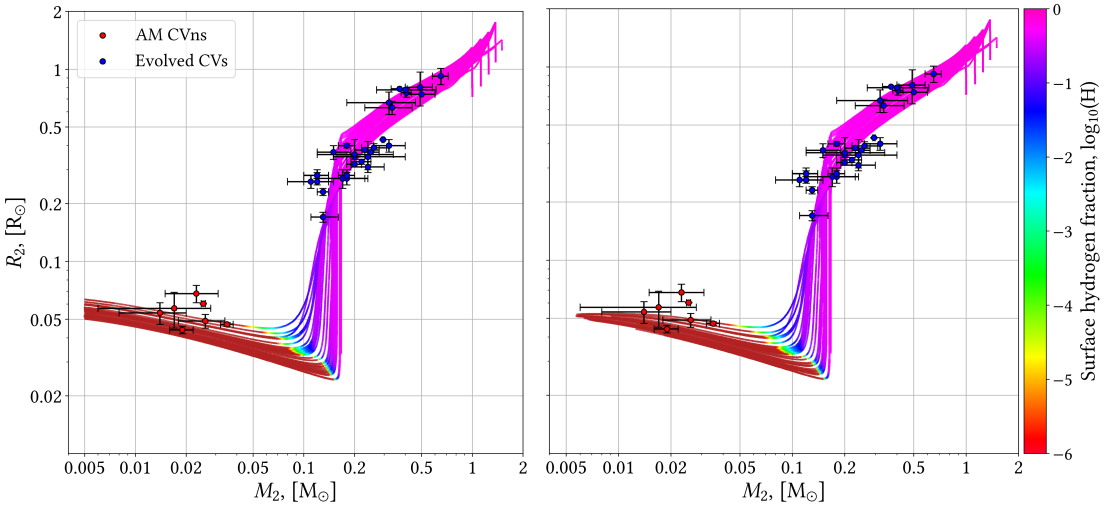

Figure 4.17: The donor radius in terms of its mass for our simulations, which reach periods $P < 2$ hrs and the donor exceeds a surface gravity of 10^6 cm s^2. The color scale is the surface hydrogen abundance of the donor. Note two sets of simulation is shown, one where MB is allowing during the compact phase (left), and one where MB is turned off once the donor reaches this phase (right). The observational data for the AM CVns and evolved CVs has been plotted as red and blue dots respectively, along with known errors. The brown color indicate a surface hydrogen fractions lower than 10^{-6}.

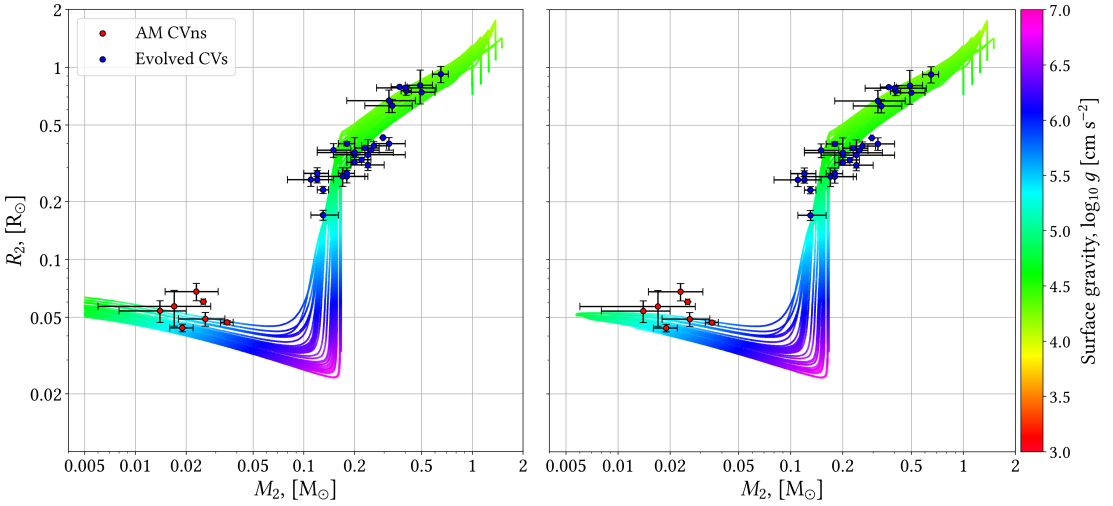

Figure 4.18: The donor radius in terms of its mass for, which reach periods $P < 2$ hrs and the donor exceeds a surface gravity of 10^6 cm s^2. The color scale is the surface gravity of the donor throughout the systems evolution. Note two sets of simulation is shown, one where MB is allowing during the compact phase (left), and one where MB is turned off once the donor reaches this phase (right). The observational data for the AM CVns and evolved CVs has been plotted as red and blue dots respectively, along with known errors.

It does not seem that there is any difference in the evolution between the systems of Figure 4.17 and Figure 4.18 up until the surface gravity exceeds 10^6 cm s^2. In the systems where MB is not allowed once this limit has been exceeded, all the compact donors seem to converge towards the same radii as their mass decreases. In order to investigate this further we look at the mass transfer rates, following period minimum in the next section.

4.4.1 Mass Transfer Rates of Observed AM CVns

In Figure 4.19 we have plotted the mass transfer rates with respect to orbital period, to give a brief overview of how all the systems behave during the final stages of mass transfer. The color scale defines the normalized time since the system reached a period of 200 minutes. It is calculated as

$$T_N = \frac{t - t_{P<200}}{t_{max} - t_{P<200}}, \tag{4.4.1}$$

where t_{max} is the max age of the system before the simulation is terminated and $t_{P<200}$ is the age of the system when it first reached a period of 200 minutes. This allows us to better determine the direction that the tracks have in the plot, as for increasing values of the age, t, the color changes. Furthermore, the mass transfer simulation data have been smoothed using a median and Gaussian filter from `SciPy`, to improve clarity and better distinguish the different tracks from each other (this is explained in greater detail in Appendix C).

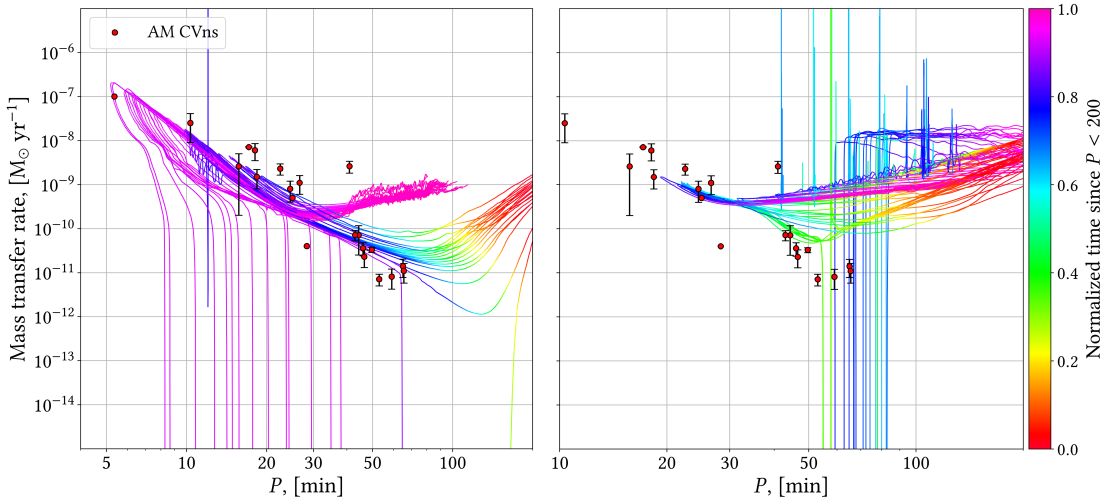

Figure 4.19: The mass transfer in terms of the orbital period of our simulated systems, which reach periods $P < 2$ hrs, where the donor exceeds a surface gravity of 10^6 cm s^2 (left) and those where it did not (right). The color scale is the normalized time since the orbital period reached a value under 200 minutes (see text for explanation). A median and gaussian filter has been used to smooth the data to remove simulation noise. The observational data for the AM CVns has been plotted as red dots, along with known errors.

In the left plot in Figure 4.19 we have the systems in which the surface gravity of the donor exceeds 10^6 cm s^2. Here we see that the system with the shortest periods is those that have been detached. Some systems have not been through a detached phase and first reach a period under 200 min to the right in the figure, as highlighted by the red color. These systems do not attain as low periods as those that have been detached, but end up in the same area. In terms of the observed AM CVns, we are able to intersect their mass transfer rates, however as is evident Figure 4.14 we should intersect them at a phase where their orbital periods are increasing in terms of the donor mass. Having this in mind, we see that the only able to reproduce a few systems in terms of their mass transfer rates as most of the systems which we intersect with our tracks here are decreasing in period.

The right plot in Figure 4.19 shows the tracks of all the other systems, in which the surface gravity of the donor never exceeds 10^6 cm s^2. Curiously, a single system can be seen coming from the right, spike in mass transfer, and become detached very briefly before mass transfer continues again (light green lines to the right of the blue ones). This is most likely a numerical fluke, but it could also have been triggered by a sudden increase in the radius leading to the mass-transfer spike, which would be dynamically unstable.

Here we also have two different families of systems, some that have been detached and ones that have not. However, unlike the detached systems which have a compact donor, these immediately evolve towards longer periods as soon as they initiate their secondary mass transfer phase. To emphasize this we have plotted Figure 4.20, for these low degeneracy donors, which has a color scale with respect to the relevant mass transfer rates. One clearly sees that the binary becomes detached, and once the orbital period has shrunk substantially, mass transfer starts again, but the mass transfer rate remains constant, as is also evident in Figure 4.19.

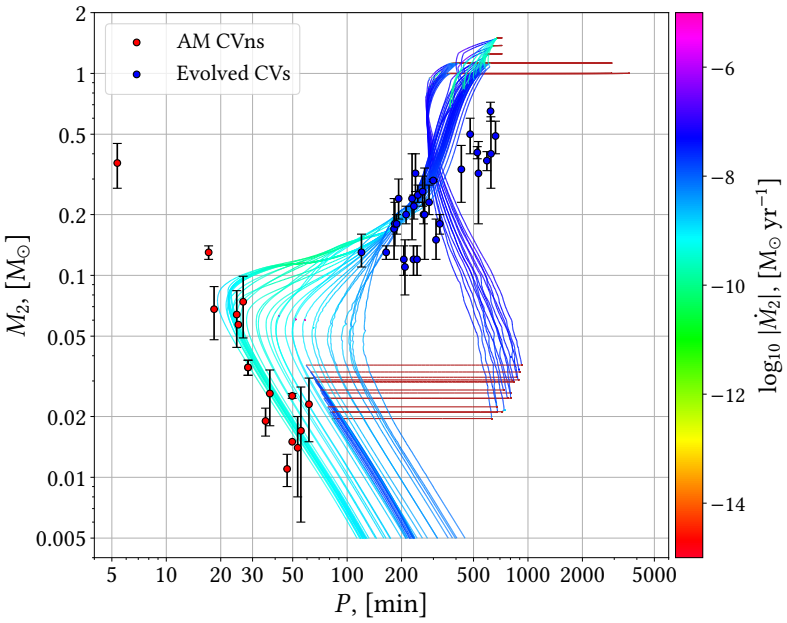

Figure 4.20: The donor mass in terms of the period of our simulations, which reach periods $P < 2$ hrs, but where the donor never exceeds a surface gravity of 10^6 cm s^2. The color scale shows the mass transfer rates throughout the systems evolution. The observational data for the AM CVns and evolved CVs has been plotted as red and blue dots respectively, along with known errors. The brown color indicate a mass transfer rates lower than 10^{-15} M$_\odot$ yr^{-1}.

The systems which have had continuous mass transfer reach lower orbital periods, but they do not converge towards the same end point as the systems with compact donors. From Figure 4.21, showing the mass transfer rates of the systems where surface gravity of the donor never exceeds 10^6 cm s^2, we see that the reason why the system with continuous mass transfer and non-compact donors reach lower orbital periods is because they have been able to form helium cores, and in turn allowing the donor to become more compact as the hydrogen is stripped from it. Comparing once again to the parameters of the observed systems, we are only able to reproduce three of them, considering the orbital period should be increasing. We are also able to reproduce these 3 systems with the tracks for compact donors.

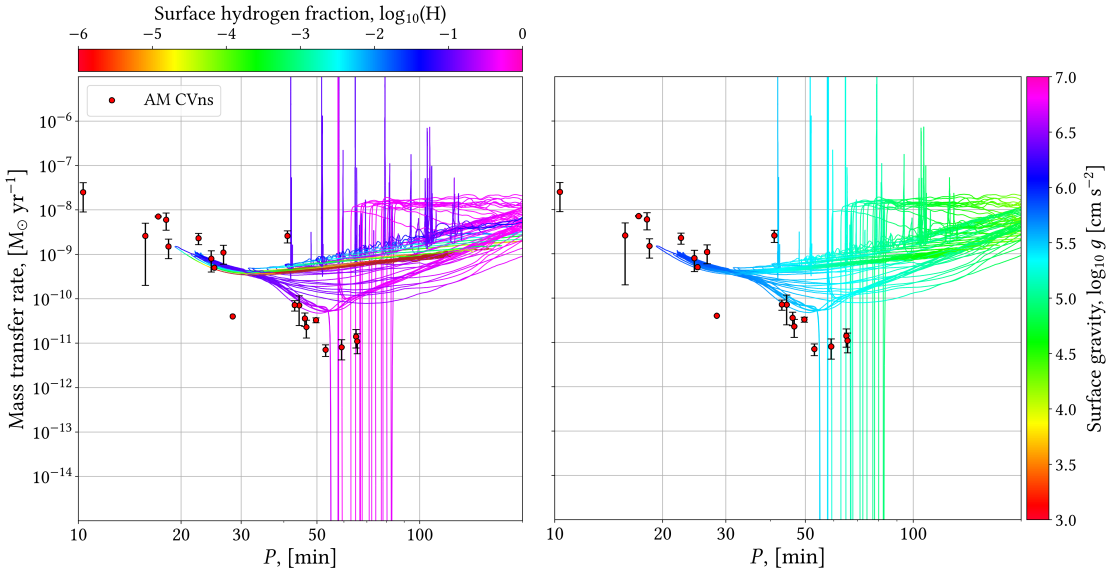

Figure 4.21: The mass transfer in terms of the orbital period of our simulated systems, which reach periods $P < 2$ hrs, but where the donor never exceeds a surface gravity of 10^6 cm s^2. Two color scales have been used, one for the surface hydrogen abundance (left) and one for the surface gravity (right) of the donor. A median and gaussian filter has been used to smooth the data to remove simulation noise. The observational data for the AM CVns has been plotted as red dots, along with known errors. The brown color indicate a surface hydrogen fractions lower than 10^{-6}.

Now we investigate the systems in which the surface gravity of the donor exceeds 10^6 cm s^2, and compare the tracks where we have MB afterwards, to those in which we turn it off. Looking at Figure 4.22, we can see the values of the angular momentum lost due to MB throughout the mass transfer and period evolution. Note that MB is, in fact, turned off in the red part of the tracks in the right panel, but in order to gain better resolution in terms of the color scale, a cutoff was made at $\log |\dot{J}_{MB}| = 20$. We clearly see the effects of turning off MB once we have a WD, our tracks now continue down, and the mass transfer rates continue to decrease as the period increase, whereas the mass transfer rate increases for the systems that still have MB.

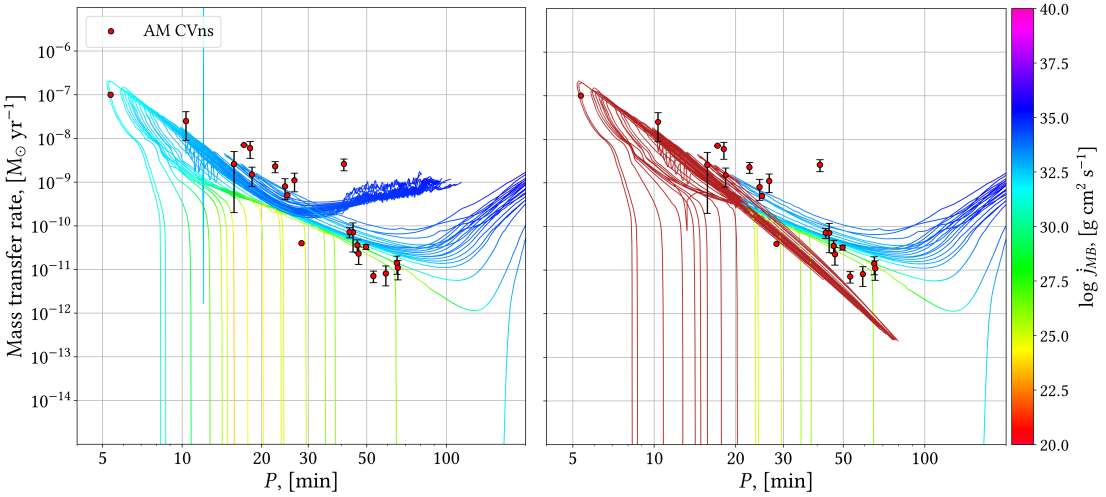

Figure 4.22: The mass transfer in terms of the orbital period of our simulated systems, which reach periods $P < 2$ hrs and the donor exceeds a surface gravity of 10^6 cm s^2. The color scale shows the magnetic braking throughout the systems evolution. Note two sets of simulation is shown, one where MB is allowing during the compact phase (left), and one where MB is turned off once the donor reaches this phase (right). A median and gaussian filter has been used to smooth the data to remove simulation noise. The observational data for the AM CVns has been plotted as red dots, along with known errors. The brown color indicate $|\dot{J}_{mb}|$ lower than 10^{20} g cm^2 s^{-1}.

From the left panel in Figure 4.23, we see that as the donor becomes less compact, the MB increases. This might be caused by an increase in radius because as the degenerate donor loses mass, it expands.

In terms of the observed systems, we are only able to reproduce one more system near $P \sim 30min$ and $\dot{M} \sim 5^{-11}$, named KL Dra, when turning off MB. This system has no uncertainties listed, which makes this result weaker, as the parameters of this system might be poorly estimated. However, we get tracks which get closer to the vicinity of points with lower mass transfer rates and periods around $\sim$ 50 min, while the period is increasing as well. This seems to be more reasonable than the mass transfer rate caused by the MB in the compact phase of the other systems. A solution which is some middle point between these two cases seem to be preferably, as it would allow us to reproduce the system with lower mass transfer rates and periods around $\sim$ 50 min.

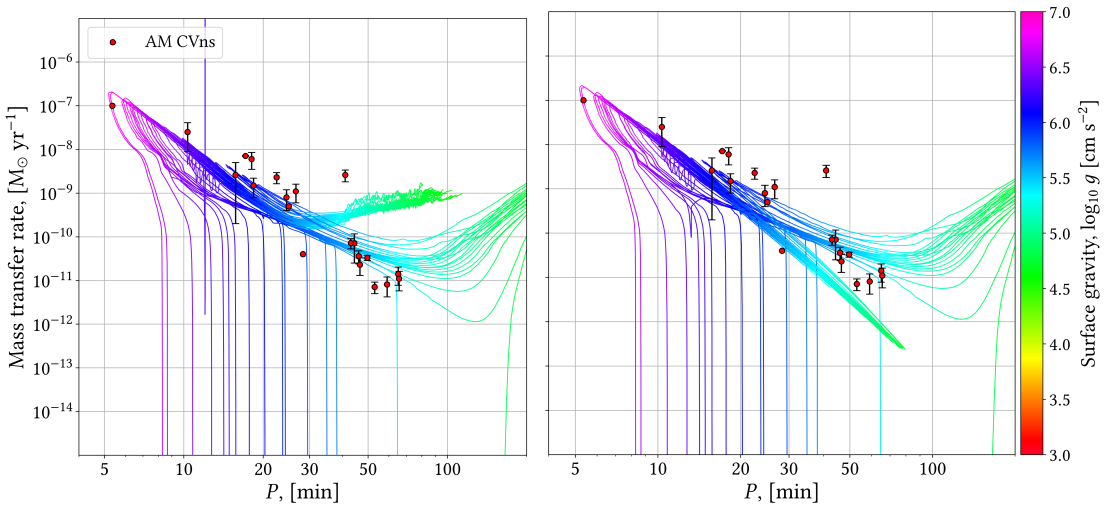

Figure 4.23: The mass transfer in terms of the orbital period of our simulated systems, which reach periods $P < 2$ hrs and the donor exceeds a surface gravity of 10^6 cm s^2. The color scale shows the surface gravity of the donor. Note two sets of simulation is shown, one where MB is allowing during the the compact phase (left), and one where MB is turned off once the donor reaches this phase (right). A median and gaussian filter has been used to smooth the data to remove simulation noise. The observational data for the AM CVns has been plotted as red dots, along with known errors.

Another relevant aspect we can use for comparison with our simulated systems is the expected gravitational wave signal of the observed systems. We can find the characteristic strain for some of the observed systems, where the distance and masses are known, as well as the period. This will be explored in the next section.

4.4.2 Strain Evolution

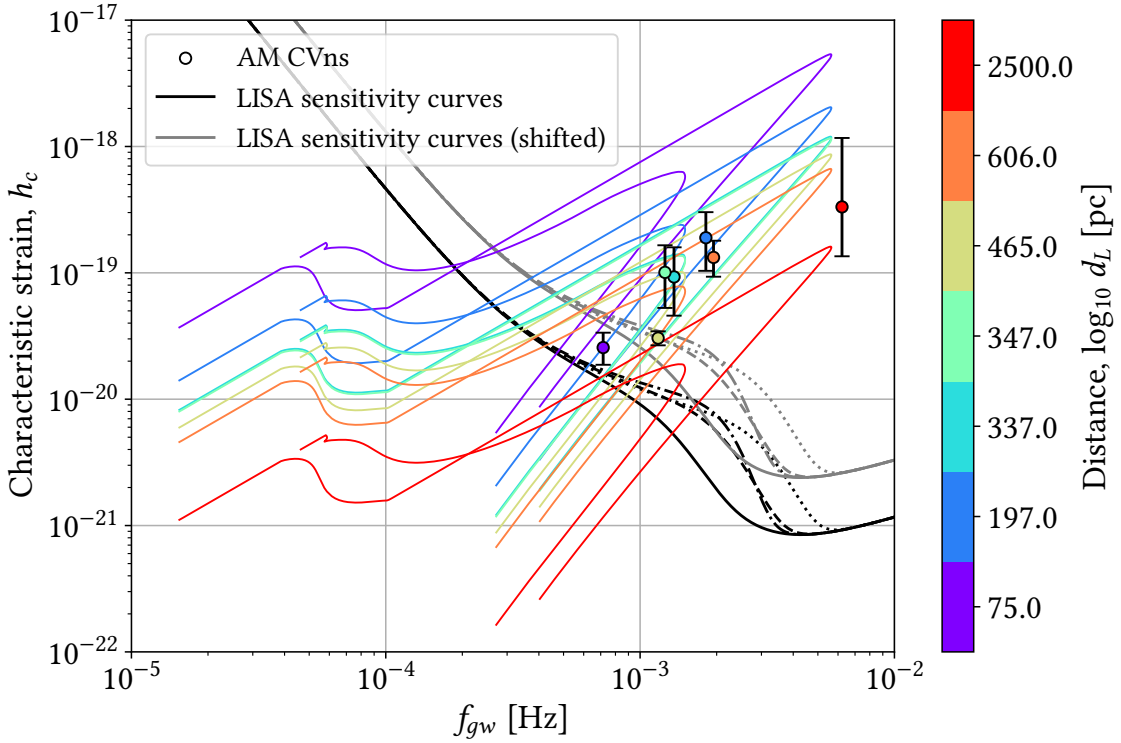

Figure 4.24: Characteristic strain evolution with respect to gravitational wave frequency color graded according to distance. 7 data points for AM CVns for which the distance is estimated is included. The error bars represent the min and max error in characteristic strain using the uncertainties in masses and distance, when given. The tracks which share a color with a data point are generated using that data points distance. The systems plotted are: GP Com, HP Lib, CR Boo, V803 Cen, J0926+3624, AM CVn and HM Cnc. The associated distances are $d_L = [75, 197, 337, 347, 465, 606, 2500]$ pc in the same order as the names. The black line is the sensitivity curve for LISA after 4 yrs to 0.5 yrs for the solid to the dotted line as done in Section 2.5. whereas the gray line is shifted to represent detectability for edge-on binaries in the same manner.

Figure 4.24 shows the strain evolution for two of our simulated systems which results in relatively high and low characteristic strain amplitudes in the compact binary phase. The initial accretor and donor masses for the tracks are $M_{1,0} = 1.0\ M_\odot$ and $M_{2,0} = 1.25\ M_\odot$ respectively. The initial periods are $P_0 = 1.5$ days and $P_0 = 0.5$ days for the tracks with the highest and lowest peak, respectively. Each set of tracks have been plotted assuming the distance gathered from the observational data points with the same color, thus the highest purple tracks should be comparable to the purple data point, that being GP Com at a estimated distance of 75 pc, under the assumption that it have formed though the CV channel. The AM CVns plotted is GP Com, HP Lib, CR Boo, V803 Cen, J0926+3624, AM CVn and HM Cnc. The associated distances from the data are $d_L = [75, 197, 337, 347, 465, 606, 2500]$ pc in the same order as the names. The consequence of a greater distance is that the tracks are shifted downwards and has lower h_c, thus the order of the tracks from highest to lowest h_c in Figure 4.24, is associated to the presented list of d_L, which is sorted from closest to farthest system. A clear outlier here is again the HM Cnc system (red data point) which seam to have a slightly higher total mass at a lower orbital period than what our simulations can produce. AM CVn (orange data point and tracks) seems to be place neatly between the two evolutionary tracks, however as previously discussed, this system do not seem to fit our donor evolutions. Thus cation should be made when comparing it to these tracks. As the rest of the data point seems to fit the assumed CV

evolution (as seen in the previous two sections), the tracks shown in Figure 4.24 might be more reasonable for these systems. As the strain amplitude is not at the highest of what our simulated track can produce, the inclination angle plays a greater role as to their detectability. J0926+3624 (that being the sand colored data point and tracks in Figure 4.24) is an eclipsing binary as discussed by Copperwheat et al. (2011), thus the inclination angle is high ($i = 82.6 \pm 0.3$ deg). Therefore, when determining the detectability of this system the light gray sensitivity curves should be considered. Thus the gravitational wave signal from this system is not expected to be resolvable from the galactic noise. Some of the other systems which have estimates for the inclination angle is AM CVn, HP Lib, CR Boo, and V803 Cen, which is given by Roelofs et al. (2007) to be $i = [43 \pm 2, 26-34, 30, 12-15]$ deg, in the same order. These are the orange, blue, light blue and mint green data point, respectively. Here the most inclined system is AM CVn, however this system also has a fairly strong theoretical strain amplitude with a h_c more than 10 times stronger than the shifted sensitivity curve, after 4 years of observation. Thus it is most likely to be resolvable and show up as a LISA source. The same arguments can be made for HP Lib (the blue data point) which lie next to AM CVn in Figure 4.24 but with a smaller inclination angle and a higher theoretical strain amplitude. CR Boo (light blue) and V803 Cen (mint green) lie closer to the sensitivity curves and are thus more prone to not being detectable. As the sensitivity curve provided is a sky-averaged sensitivity, the location might play a more significant role here as directional noise could be more prominent in some areas. However, with respect to the sky-averaged curve these theoretical signals is at least 10 times stronger than the sensitivity curve, even for CR Boo with the estimated inclination angle of $i = 30$ deg, modifying the face-on strain amplitude by $\approx 0.87h$, (see (2.5.17)), thus placing its shifted sensitivity curve slightly above the black face-on sensitivity curve. The last data point to be discussed is GP Com (purple) which lies right between the black and gray sensitivity curves, thus it is most likely not detectable. Moreover, no inclination angle for this system has been found and was also omitted in Roelofs et al. (2007), further shrouding its detectability from a theoretical perspective. Though, as discussed in Roelofs et al. (2007), it is expected to have had a much shorter orbital period in the past, based on the fact that the current accretion rate is low when compared to the accretors' temperature, which is most likely set by accretion induced heating. Thus it is expected to be in the late stages of the AM CVn phase which also matches its placement on Figure 4.24 with respect to our simulated purple tracks.

Chapter 5

Conclusion

Throughout this thesis an analysis of AM CVn systems as potential LISA sources has been made. The evolutionary scenarios resulting in AM CVn binaries was first elaborated. Relevant physics including mass transfer, novae eruptions, magnetic braking and gravitational wave radiation was presented to grant the reader an overview of all the different effects, which play a prominent role in the evolution of these systems.

Emphasis was put on the CV evolutionary scenario, were AM CVns are formed from a binary system of a white dwarf and a low mass main sequence star, which follows from the common envelope phase. The consequences of mass transfer were investigated to determine the binaries response. For the novae eruptions two accumulation efficiencies were defined, depending on whether the accreted material was hydrogen-rich or helium-rich, to decide whether the white dwarf accretor accumulated material. The convection and rotation boosted (CARB) magnetic braking prescription was elaborated along with a section comparing it with the Skumanich magnetic braking prescription. Furthermore, the strain amplitude of the gravitational wave signal and the LISA sensitivity curves were included to evaluate the gravitational signal received from these binaries.

In order to simulate the full evolution from CV binary to AM CVn systems `MESA` was utilized. In this thesis version 24.08.1 of `MESA` was used, and modified to include the CARB magnetic braking model, nova eruption physics for the accretor and finally specific Eddington accretion limits for a white dwarf accretor. As `MESA` is a general purpose stellar evolution code, these tight binaries proved difficult to simulate without relaxing some parameters, which controls the tolerances for each timestep. Otherwise simulations would terminate once the AM CVn phase was reached, due to computational errors. To evaluate our simulations, we found observational data for AM CVn systems to use as benchmarks, and evolved CV systems. The latter were included such that we could determine whether we also were able to reproduce these, which is required following our assumed evolution.

The choice in magnetic braking prescription was very impactful in terms of the evolution of the systems. Using the CARB prescription we were able to successfully evolve AM CVns without the issues of fine-tuning which was the case when using the Skumanich prescription. Different sweet spots of parameters were found which produced AM CVns within 14 Gyrs. Mainly, donor masses around 1.25 $M_\odot$ yielded AM CVns, but other configurations were also possible. The donor mass had the largest influence because it determines the how fast a He-core could be formed. The He-core mass at the onset of mass transfer was a crucial factor in the destiny of the simulated systems. If the He-core got too big it would result in a orbital separation, at the end of this mass transfer phase, which was to large for the binary to initiate secondary mass transfer within 14 Gyrs. If the He-core was to small or did not form at all, we did not end up with an AM CVn, because of a high surface hydrogen fraction. Furthermore, the initial orbital separation was found to be the deciding factor in controlling how large the He-core was allowed to become, given a specific donor mass. Hence different configurations determined by the orbital period and accretor mass, which influenced the orbital separation, were favorable. As an example the sweet spot in

post common envelope orbital separations for a donor mass of 1.25 $M_\odot$ was found to be [3.475, 7.23] $R_\odot$.

By comparing our simulations with observational data we were able to reproduce almost all AM CVns and evolved CVs in terms of donor mass, period and radius. A notable system which we were not able to reproduce was HM Cnc. Compared to our simulations the mass and orbital period of the donor seemed to high and short, respectively. However, that could be due to it being formed through the double white dwarf channel, for which higher mass donors are expected. Another notable system which proved difficult to justify with our simulations was the original AM CVn. Although it fits nicely within our evolutionary tracks with respect to mass and orbital period, our simulated systems had higher surface hydrogen fractions, of above 0.1, in this area. Indicating that accretion here would yield hydrogen in the spectra and thus not be true AM CVns. Thus this system might also have evolved through a different evolution channel as it is most definitely an AM CVn. Some of the evolved CVs also seem to be on the track to becoming AM CVns, while others could be disregarded, following our simulated evolution. For the AM CVns the mass transfer rates were a lot harder to reproduce. However, there are also more uncertainties surrounding this parameter.

It was discovered that magnetic braking was still prominent even tho the donor had become a compact object, with a surface gravity exceeding 10^6 cm s^2. This caused the mass transfer rate to increase again after period minimum as the binary system was tightened. Because of the uncertainties surrounding the generation of magnetic fields in white dwarfs we made additional simulations where magnetic braking was turned off as soon as the surface gravity of the donor exceeded 10^6 cm s^2. By doing this the mass transfer rates fell in accordance with an increasing period and we were able to reproduce one more observed system, named KL Dra. However, the lack of uncertainties in the mass transfer rate for this system weakened this result as it might have been poorly estimated. We were however not able to reproduce a huge collection of systems with periods around 50 minutes and mass transfer rates of 10^{-11}–10^{-11} $M_\odot$ yr^{-1}, which were reproduced in terms of the donor mass and orbital period, even when turning off magnetic braking. It does seem like a mechanism is needed to pull the binary slightly closer together such that these systems can be intersected. The CARB magnetic braking is too strong such that we overshoot the mass transfer rates and in turning off magnetic braking, we undershoot the mass transfer rates. Thus another prescription is needed for compact donors in order to reproduce these systems.

7 systems with estimates for both mass components and distance was found in the literature. That being GP Com, HP Lib, CR Boo, V803 Cen, J0926+3624, AM CVn and HM Cnc. Of these 7 systems only GP Com, J0926+3624 and HM Cnc did not have estimated inclination angles. Thus we where able to plot the characteristic strain amplitude for these systems, with a better estimate for the 4 with reported inclination angles. Out of these systems we expect all except GP Com and J0926+3624 to show up as LISA sources as the strain amplitude found was at least 10 times greater than that of the sensitivity curve. With HM Cnc having 100 times the strain amplitude, even assuming its a edge-on binary which produce a weaker gravitational wave signal. Furthermore, these systems all line up well with our simulated tracks, adjusted for distance, except HM Cnc which high mass and short orbital period shifts it towards a stronger gravitational signal than our simulated systems. For CR Boo and V803 Cen the signal is slightly closer to the sensitivity curve, so their detectability is a bit more obscured as their location might play a larger role when it comes to galactic background noise. However, with respect to the sky-average sensitivity curve, they are at least 10 times stronger in signal. A final note on detectability is that we expect that once LISA is operational, many more AM CVns will show up. Many of our simulated system, which yielded AM CVns, becomes strongly detectable during their evolution. Assuming a distance of 1 kpc the most luminous simulated systems yield characteristic strain amplitudes up to 300 times that of the sensitivity

curve, assuming face-on binaries.

5.1 Outlook

Using the MESA code and inlists from the simulations in this thesis, more aspect of magnetic braking could have been inspected. Different magnetic field prescription could have been implemented for the compact donors following the initial mass transfer phase. This would allow us to fine tune the resulting magnetic braking in the later stages of the AM CVns evolution, potentially allowing us to reproduce the huge collection of observed systems with periods around 50 minutes and mass transfer rates of 10^{-11}–10^{-11} $M_\odot$ yr^{-1}.

The viability of the CARB model as a universal model could also be tested, as it is a stronger model compared to the standard Skumanich model. This could be done by trying to reproduce known wide-orbit millisecond pulsars, which require both a mass transfer phase to spin-up the neutron star, and a subsequent widening of the orbit. If the CARB model is to strong, these systems should be difficult to reproduce, as it will keep them close.

Bibliography

Amaro-Seoane, P., Audley, H., Babak, S., Baker, J., Barausse, E., Bender, P., Berti, E., et al. (2017). Laser Interferometer Space Antenna. *arXiv e-prints*, page arXiv:1702.00786.

Ashley, R. P., Marsh, T. R., Breedt, E., Gänsicke, B. T., Pala, A. F., Toloza, O., Chote, P., et al. (2020). V1460 Her: a fast spinning white dwarf accreting from an evolved donor star. *Monthly Notices of the Royal Astronomical*, 499(1):149–160.

Barros, S. C. C., Marsh, T. R., Dhillon, V. S., Groot, P. J., Littlefair, S., Nelemans, G., Roelofs, G., et al. (2007). Ultracam photometry of the ultracompact binaries v407 vul and hm cnc. *Monthly Notices of the Royal Astronomical Society*, 374(4):1334–1346.

Belloni, D. and Schreiber, M. R. (2023). Reversing the verdict: Cataclysmic variables could be the dominant progenitors of am cvn binaries after all. *Astrophysical & Astrophysics*, 678:A34.

Beuermann, K., Breitenstein, P., and Schwab, E. (2022). J1832.4-1627, the first eclipsing stream-fed intermediate polar. *Astronomy and Astrophysics*, 657:A101.

Chabrier, G., Mazevet, S., and Soubiran, F. (2019). A New Equation of State for Dense Hydrogen-Helium Mixtures. *The Astrophysical Journal*, 872(1):51.

Copperwheat, C. M., Marsh, T. R., Littlefair, S. P., Dhillon, V. S., Ramsay, G., Drake, A. J., Gänsicke, B. T., and others (2011). SDSS J0926+3624: the shortest period eclipsing binary star. *Monthly Notices of the Royal Astronomical*, 410(2):1113–1129.

Cornish, N. (2019). Lisa sensitivity. `https://github.com/eXtremeGravityInstitute/LISA_Sensitivity`. Accessed: 11 May, 2025.

Douglass, D. H. and Braginsky, V. B. (1979). Gravitational-radiation experiments. In *General Relativity: an Einstein Centenary Survey*, pages 90–137. Cambridge University Press.

Dufour, P., Blouin, S., Coutu, S., Fortin-Archambault, M., Thibeault, C., Bergeron, P., and Fontaine, G. (2017). The Montreal White Dwarf Database: A Tool for the Community. In Tremblay, P. E., Gaensicke, B., and Marsh, T., editors, *20th European White Dwarf Workshop*, volume 509 of *Astronomical Society of the Pacific Conference Series*, page 3. Downloaded: 19 May, 2025.

Echevarría, J., Michel, R., Costero, R., and Zharikov, S. (2007). Determination of the basic parameters of the dwarf nova EY Cygni. *Astronomy and Astrophysics*, 462(3):1069–1080.

Echevarría, J., Smith, R. C., Costero, R., Zharikov, S., and Michel, R. (2008). High-dispersion absorption-line spectroscopy of AE Aqr. *Monthly Notices of the Royal Astronomical*, 387(4):1563–1574.

Eggleton, P. P. (1983). Aproximations to the radii of Roche lobes. *The Astrophysical Journal*, 268:368–369.

El-Badry, K., Rix, H.-W., Quataert, E., Kupfer, T., and Shen, K. J. (2021). Birth of the ELMs: a ZTF survey for evolved cataclysmic variables turning into extremely low-mass white dwarfs. *Monthly Notices of the Royal Astronomical*, 508(3):4106–4139.

ESA (2025). Lisa factsheet. `https://www.esa.int/Science_Exploration/Space_Science/LISA/LISA_factsheet`. Accessed: 26 May, 2025.

Esposito, P., Israel, G. L., Dall'Osso, S., and Covino, S. (2014). Swift X-ray and ultraviolet observations of the shortest orbital period double-degenerate system RX J0806.3+1527 (HM Cnc). *Astronomy and Astrophysics*, 561:A117.

Fontaine, G., Brassard, P., Green, E. M., Charpinet, S., Dufour, P., Hubeny, I., Steeghs, D., et al. (2011). Discovery of a New AM CVn System with the Kepler Satellite. *The Astrophysical Journal*, 726(2):92.

Freedman, R. S., Marley, M. S., and Lodders, K. (2008). Line and Mean Opacities for Ultracool Dwarfs and Extrasolar Planets. *Astrophysical Journal Supplement*, 174(2):504–513.

Gomez, S., Torres, M. A. P., Jonker, P. G., Kostrzewa-Rutkowska, Z., van Grunsven, T. F. J., Udalski, A., Hynes, R. I., et al. (2021). Dynamical modelling of CXOGBS J175553.2-281633: a 10 h long orbital period cataclysmic variable. *Monthly Notices of the Royal Astronomical*, 502(1):48–59.

Green, M. J., Marsh, T. R., Steeghs, D. T. H., Kupfer, T., Ashley, R. P., Bloemen, S., Breedt, E., et al. (2018). High-speed photometry of gaia14aae: an eclipsing am cvn that challenges formation models. *Monthly Notices of the Royal Astronomical Society*, 476(2):1663–1679.

Hachisu, I. and Kato, M. (2001). Recurrent Novae as a Progenitor System of Type Ia Supernovae. I. RS Ophiuchi Subclass: Systems with a Red Giant Companion. *The Astrophysical Journal*, 558(1):323–350.

Hachisu, I., Kato, M., and Nomoto, K. (1999). A Wide Symbiotic Channel to Type IA Supernovae. *The Astrophysical Journal*, 522(1):487–503.

Hellier, C. (2001). *Cataclysmic Variable Stars-how and why they vary*. Springer Science & Business Media.

Henyey, L., Vardya, M. S., and Bodenheimer, P. (1965). Studies in Stellar Evolution. III. The Calculation of Model Envelopes. *The Astrophysical Journal*, 142:841.

Irwin, A. W. (2008). FreeEOS. `https://freeeos.sourceforge.net/`. version 2.2.1.

Ivanova, N., Justham, S., Chen, X., De Marco, O., Fryer, C. L., Gaburov, E., Ge, H., et al. (2013). Common envelope evolution: where we stand and how we can move forward. *The Astronomy and Astrophysics Review*, 21(1).

Jermyn, A. S., Bauer, E. B., Schwab, J., Farmer, R., Ball, W. H., Bellinger, E. P., Dotter, A., et al. (2023). Modules for Experiments in Stellar Astrophysics (MESA): Time-dependent Convection, Energy Conservation, Automatic Differentiation, and Infrastructure. *Astrophysical Journal Supplement*, 265(1):15.

Jermyn, A. S., Schwab, J., Bauer, E., Timmes, F. X., and Potekhin, A. Y. (2021). Skye: A Differentiable Equation of State. *The Astrophysical Journal*, 913(1):72.

Joyce, M. and Tayar, J. (2023). A Review of the Mixing Length Theory of Convection in 1D Stellar Modeling. *Galaxies*, 11(3):75.

Kato, M. and Hachisu, I. (1999). A New Estimation of Mass Accumulation Efficiency in Helium Shell Flashestoward Type IA Supernova Explosions. *The Astrophysical Journal Letters*, 513(1):L41–L44.

Kato, M. and Hachisu, I. (2004). Mass Accumulation Efficiency in Helium Shell Flashes for Various White Dwarf Masses. *The Astrophysical Journal Letters*, 613(2):L129–L132.

Knigge, C., Baraffe, I., and Patterson, J. (2011). The Evolution of Cataclysmic Variables as Revealed by Their Donor Stars. *Astrophysical Journal Supplement*, 194(2):28.

Kuhfuss, R. (1986). A model for time-dependent turbulent convection. *Astronomy and Astrophysics*, 160(1):116–120.

Livio, M. (1994). Topics in the theory of cataclysmic variables and X-ray binaries. In *Saas-Fee Advanced Course 22: Interacting Binaries*, pages 135–262.

Maggiore, M. (2008). Applications. In *Gravitational Waves: Volume 1 - Theory and Experiments*, pages 167–236. Oxford University Press.

Martynov, D. V., Hall, E. D., Abbott, B. P., Abbott, R., Abbott, T. D., Adams, C., Adhikari, R. X., and others (2016). Sensitivity of the advanced ligo detectors at the beginning of gravitational wave astronomy. *Physical Review D*, 93(11):112004.

Matt, S. P., Pinzón, G., Greene, T. P., and Pudritz, R. E. (2012). Spin Evolution of Accreting Young Stars. II. Effect of Accretion-powered Stellar Winds. *The Astrophysical Journal*, 745(1):101.

McDonald, I. and Zijlstra, A. A. (2015). Mass-loss on the red giant branch: the value and metallicity dependence of reimers' η in globular clusters. *Monthly Notices of the Royal Astronomical Society*, 448(1):502–521.

Miesch, M. S. (2005). Large-Scale Dynamics of the Convection Zone and Tachocline. *Living Reviews in Solar Physics*, 2(1):1.

Nauenberg, M. (1972). Analytic Approximations to the Mass-Radius Relation and Energy of Zero-Temperature Stars. *The Astrophysical Journal*, 175:417.

Paczynski, B. (1976). Common Envelope Binaries. In Eggleton, P., Mitton, S., and Whelan, J., editors, *Structure and Evolution of Close Binary Systems*, volume 73 of *IAU Symposium*, page 75.

Paxton, B., Bildsten, L., Dotter, A., Herwig, F., Lesaffre, P., and Timmes, F. (2011). Modules for Experiments in Stellar Astrophysics (MESA). *Astrophysical Journal Supplement*, 192(1):3.

Paxton, B., Cantiello, M., Arras, P., Bildsten, L., Brown, E. F., Dotter, A., Mankovich, C., et al. (2013). Modules for Experiments in Stellar Astrophysics (MESA): Planets, Oscillations, Rotation, and Massive Stars. *Astrophysical Journal Supplement*, 208(1):4.

Paxton, B., Marchant, P., Schwab, J., Bauer, E. B., Bildsten, L., Cantiello, M., Dessart, L., et al. (2015). Modules for Experiments in Stellar Astrophysics (MESA): Binaries, Pulsations, and Explosions. *Astrophysical Journal Supplement*, 220(1):15.

Paxton, B., Schwab, J., Bauer, E. B., Bildsten, L., Blinnikov, S., Duffell, P., Farmer, R., et al. (2018). Modules for Experiments in Stellar Astrophysics (MESA): Convective Boundaries, Element Diffusion, and Massive Star Explosions. *Astrophysical Journal Supplement*, 234(2):34.

Paxton, B., Smolec, R., Schwab, J., Gautschy, A., Bildsten, L., Cantiello, M., Dotter, A., et al. (2019). Modules for Experiments in Stellar Astrophysics (MESA): Pulsating Variable Stars, Rotation, Convective Boundaries, and Energy Conservation. *Astrophysical Journal Supplement*, 243(1):10.

Peters, P. C. and Mathews, J. (1963). Gravitational radiation from point masses in a keplerian orbit. *Phys. Rev.*, 131:435–440.

Potekhin, A. Y. and Chabrier, G. (2010). Thermodynamic Functions of Dense Plasmas: Analytic Approximations for Astrophysical Applications. *Contributions to Plasma Physics*, 50(1):82–87.

Press, W. H. and Thorne, K. S. (1972). Gravitational-Wave Astronomy. *Annual Review of Astronomy and Astrophysics*, 10:335.

Ramsay, G., Green, M. J., Marsh, T. R., Kupfer, T., Breedt, E., Korol, V., Groot, P. J., et al. (2018). Physical properties of AM CVn stars: New insights from Gaia DR2. *Astronomy and Astrophysics*, 620:A141.

Rappaport, S., Verbunt, F., and Joss, P. C. (1983). A new technique for calculations of binary stellar evolution application to magnetic braking. *The Astrophysical Journal*, 275:713–731.

Reardon, D. J., Zic, A., Shannon, R. M., Hobbs, G. B., Bailes, M., Di Marco, V., Kapur, A., and others (2023). Search for an Isotropic Gravitational-wave Background with the Parkes Pulsar Timing Array. *The Astrophysical Journal Letters*, 951(1):L6.

Reimers, D. (1975). Circumstellar envelopes and mass loss of red giant stars. In *Problems in Stellar Atmospheres and Envelopes*, pages 229–256. Springer Berlin Heidelberg, Berlin, Heidelberg.

Réville, V., Brun, A. S., Matt, S. P., Strugarek, A., and Pinto, R. F. (2015). The Effect of Magnetic Topology on Thermally Driven Wind: Toward a General Formulation of the Braking Law. *The Astrophysical Journal*, 798(2):116.

Ritter, H. (1988). Turning on and off mass transfer in cataclysmic binaries. *Astronomy and Astrophysics*, 202:93–100.

Ritter, H. and Kolb, U. (2003). Catalogue of cataclysmic binaries, low-mass X-ray binaries and related objects (Seventh edition). *Astronomy and Astrophysics*, 404:301–303.

Robson, T., Cornish, N. J., and Liu, C. (2019). The construction and use of LISA sensitivity curves. *Classical and Quantum Gravity*, 36(10):105011.

Rodríguez-Gil, P., Torres, M. A. P., Gänsicke, B. T., Muñoz-Darias, T., Steeghs, D., Schwarz, R., Rau, A., and Hagen, H. J. (2009). An evolved donor star in the long-period cataclysmic variable HS 0218+3229. *Astronomy and Astrophysics*, 496(3):805–812.

Roelofs, G. H. A., Groot, P. J., Benedict, G. F., McArthur, B. E., Steeghs, D., Morales-Rueda, L., Marsh, T. R., and Nelemans, G. (2007). Hubble Space Telescope Parallaxes of AM CVn Stars and Astrophysical Consequences. *The Astrophysical Journal*, 666(2):1174–1188.

Rogers, F. J. and Nayfonov, A. (2002). Updated and Expanded OPAL Equation-of-State Tables: Implications for Helioseismology. *The Astrophysical Journal*, 576(2):1064–1074.

Salaris, M. and Cassisi, S. (2005). *The Hydrogen Burning Phase*, chapter 5, pages 117–159. John Wiley & Sons, Ltd.

Saumon, D., Chabrier, G., and van Horn, H. M. (1995). An Equation of State for Low-Mass Stars and Giant Planets. *Astrophysical Journal Supplement*, 99:713.

Schneider, F. R. N., Lau, M. Y. M., and Roepke, F. K. (2025). Stellar mergers and common-envelope evolution.

Schreiber, M. R., Belloni, D., Gänsicke, B. T., Parsons, S. G., and Zorotovic, M. (2021). The origin and evolution of magnetic white dwarfs in close binary stars. *Nature Astronomy*, 5:648–654.

Shapiro, S. L. and Teukolsky, S. A. (1983). *Black holes, white dwarfs and neutron stars. The physics of compact objects*. WILEY-VCH Verlag GmbH & Co. KGaA, Weinheim.

Sokolovsky, K. V., Strader, J., Swihart, S. J., Aydi, E., Bahramian, A., Chomiuk, L., Heinke, C. O., et al. (2022). 1RXH J082623.6−505741: A new long-period cataclysmic variable with an evolved donor and a low mass-transfer rate. *The Astrophysical Journal*, 934(2):142.

Solheim, J. E. (2010). AM CVn Stars: Status and Challenges. *Astronomical Society of the Pacific, Publications*, 122(896):1133.

Staude, A., Schwope, A. D., and Schwarz, R. (2001). System parameters of the long-period polar V1309 Ori. *Astronomy and Astrophysics*, 374:588–598.

Tauris, T. M., Sanyal, D., Yoon, S. C., and Langer, N. (2013). Evolution towards and beyond accretion-induced collapse of massive white dwarfs and formation of millisecond pulsars. *Astronomy and Astrophysics*, 558:A39.

Tauris, T. M. and van den Heuvel, E. P. J. (2023). *Physics of Binary Star Evolution. From Stars to X-ray Binaries and Gravitational Wave Sources*. Princeton University Press.

Timmes, F. X. and Swesty, F. D. (2000). The Accuracy, Consistency, and Speed of an Electron-Positron Equation of State Based on Table Interpolation of the Helmholtz Free Energy. *Astrophysical Journal Supplement*, 126(2):501–516.

Van, K. X. and Ivanova, N. (2019a). Evolving LMXBs: CARB Magnetic Braking. *The Astrophysical Journal Letters*, 886(2):L31.

Van, K. X. and Ivanova, N. (2019b). Evolving lmxbs: Carb magnetic braking. `https://doi.org/10.5281/zenodo.3647683`. Accessed: 12 May, 2025.

van Roestel, J., Kupfer, T., Green, M. J., Wong, T. L. S., Bildsten, L., Burdge, K., Prince, T., et al. (2022). Discovery and characterization of five new eclipsing AM CVn systems. *Monthly Notices of the Royal Astronomical*, 512(4):5440–5461.

Warner, B. (1995). The am canum venaticorum stars. *Astrophysics and Space Science*, 225:249–270.

Weber, E. J. and Davis, Jr., L. (1967). The Angular Momentum of the Solar Wind. *The Astrophysical Journal*, 148:217–227.

Yu, Z., Thorstensen, J. R., Rappaport, S., Mann, A., Jacobs, T., Nelson, L., Gänsicke, B. T., et al. (2019). A 9-h cv with one outburst in 4 yr of kepler data. *Monthly Notices of the Royal Astronomical Society*, 489(1):1023–1036.

Appendix A

Observational Data

Name	P [hrs]	M_1 [$M_\odot$]	M_2 [$M_\odot$]	R_2 [$R_\odot$]	$\dot{M}$ [$M_\odot yr^{-1}$]	d [pc]	Ref.
HM Cnc	0.089304	0.75 ± 0.15	0.36 ± 0.09	–	$\sim 10^{-7}$	2500 ± 1500	1, 2, 6
ES Cet	0.172272	–	–	–	$(2.5 \pm 1.6) \times 10^{-8}$	~ 350	1, 2, 3
J1351-0643	0.262000	–	–	–	$(2.6 \pm 2.4) \times 10^{-9}$	–	3
AM CVn	0.285768	0.71 ± 0.07	0.13 ± 0.01	–	$(7.1 \pm 0.2) \times 10^{-9}$	606^{+135}_{-93}	1, 2
J1908+3940	0.301416	–	–	–	$(6.0 \pm 2.5) \times 10^{-9}$	–	1, 4
HP Lib	0.306312	0.65 ± 0.16	0.068 ± 0.020	–	$(1.5 \pm 0.7) \times 10^{-9}$	197^{+14}_{-12}	1, 2
ASASSN-14cc	0.375000	–	–	–	$(2.30 \pm 0.65) \times 10^{-9}$	–	3
CR Boo	0.408696	0.89 ± 0.24	0.064 ± 0.020	–	$(8 \pm 4) \times 10^{-10}$	337^{+44}_{-35}	1, 2
KL Dra	0.417168	0.76	0.057	–	5×10^{-10}	–	1, 2
V803 Cen	0.443520	0.98 ± 0.20	0.074 ± 0.025	–	$(1.0 \pm 0.5) \times 10^{-9}$	347^{+32}_{-27}	1, 2
YZ LMi	0.471864	0.85 ± 0.04	0.035 ± 0.003	0.047 ± 0.001	–	–	1, 5
J0926+3624	0.472000	0.85 ± 0.04	0.035 ± 0.003	–	4×10^{-11}	465 ± 5	2
J0407-0007	0.590000	0.79 ± 0.06	0.019 ± 0.003	0.044 ± 0.002	–	–	5
J2252-0519	0.623000	0.76 ± 0.050	0.026 ± 0.008	0.049 ± 0.004	–	–	5
ASASSN-14mv	0.683000	–	–	–	$(2.60 \pm 0.79) \times 10^{-9}$	–	3
ASASSN-14ei	0.717000	–	–	–	$(7.2 \pm 1.9) \times 10^{-11}$	–	3
J1525+3600	0.739200	–	–	–	$(7.1 \pm 4.6) \times 10^{-11}$	~ 450	1, 2, 3
J1411+4812	0.768000	–	–	–	$(3.6 \pm 1.2) \times 10^{-11}$	–	1, 3
GP Com	0.776136	0.57 ± 0.07	0.011 ± 0.002	–	$(2.3 \pm 1.0) \times 10^{-11}$	75 ± 2	1, 2, 3
Gaia14aae	0.828000	0.872 ± 0.007	0.0253 ± 0.0007	0.0603 ± 0.0003	$(3.30 \pm 0.43) \times 10^{-11}$	–	1, 2, 5
J1611+6308	0.828456	0.78 ± 0.015	–	–	–	–	5
J1208+3550	0.883200	–	–	–	$(7.1 \pm 2.1) \times 10^{-11}$	–	1, 3
J0220+2141	0.888000	0.83 ± 0.07	0.014 ± 0.006	0.054 ± 0.007	–	–	5
J0003+1404	0.925000	0.79 ± 0.11	0.017 ± 0.011	0.057 ± 0.012	–	–	5
J1137+4054	0.984000	–	–	–	$(8.1 \pm 3.9) \times 10^{-12}$	–	1, 3
J1637+4917	1.025000	0.90 ± 0.05	0.023 ± 0.008	0.068 ± 0.007	–	–	5
V396 Hya	1.084560	–	–	–	$(1.40 \pm 0.62) \times 10^{-11}$	92^{+13}_{-10}	1, 2, 3
J1319+5915	1.093000	–	–	–	$(1.1 \pm 0.52) \times 10^{-11}$	–	3

Table A.1: AM CVn systems with estimated parameters other than orbital period. **References:** (1) Ritter and Kolb (2003); (2) Solheim (2010) and references therein; (3) Ramsay et al. (2018); (4) Fontaine et al. (2011); (5) van Roestel et al. (2022); (6) Barros et al. (2007).

Name	**Type**	P [hrs]	M_1 [$M_\odot$]	M_2 [$M_\odot$]	R_2 [$R_\odot$]	Ref.
V1460 Her	–	4.988	0.869±0.006	0.295±0.004	0.430±0.002	2
HS 0218+3229	–	7.133	0.545±0.105	0.335±0.105	0.63±0.05	3
V1309 Ori	–	7.983	0.70±0.12	0.5±0.1	0.74	1, 4
KIC 5608384	–	8.739	0.458±0.019	0.406±0.028	0.754±0.040	5
J1832-1627	–	8.870	0.88±0.26	0.32±0.14	0.67±0.09	6
AE Aqr	–	9.880	0.63±0.05	0.37±0.04	0.79	1, 7
J1755-2816	–	10.345	0.83±0.06	0.65±0.07	0.92±0.09	1, 8
J0826-5057	–	10.400	$0.80^{+0.34}_{-0.17}$	$0.40^{+0.21}_{-0.13}$	0.78	9
EY Cyg	–	11.024	1.10±0.09	0.49±0.12	0.805±0.161	1, 10
P2_00a	ELM	2.000	$0.98^{+0.18}_{-0.21}$	$0.13^{+0.03}_{-0.02}$	0.17±0.01	11
P2_74a	ELM	2.740	0.62±0.06	0.13±0.01	0.23±0.01	11
P3_03a	ELM	3.030	$0.77^{+0.14}_{-0.11}$	$0.17^{+0.07}_{-0.05}$	0.27±0.03	11
P3_06a	ELM	3.060	0.51±0.06	$0.18^{+0.05}_{-0.04}$	$0.27^{+0.03}_{-0.02}$	11
P3_13a	ELM	3.130	$0.74^{+0.09}_{-0.08}$	0.18±0.02	0.28±0.01	11
P3_21a	ELM	3.210	$0.95^{+0.10}_{-0.09}$	$0.24^{+0.06}_{-0.05}$	0.31±0.02	11
P3_43a	ELM	3.430	$0.57^{+0.05}_{-0.04}$	0.12±0.02	0.26±0.01	11
P3_48a	ELM	3.480	$0.53^{+0.09}_{-0.06}$	$0.11^{+0.04}_{-0.03}$	0.26±0.02	11
P3_53a	ELM	3.530	$0.83^{+0.19}_{-0.16}$	0.20±0.02	0.32±0.01	11
P3_81a	ELM	3.810	$0.96^{+0.18}_{-0.13}$	$0.24^{+0.16}_{-0.09}$	$0.35^{+0.07}_{-0.05}$	11
P3_88a	ELM	3.880	$0.59^{+0.05}_{-0.04}$	0.12±0.02	$0.28^{+0.02}_{-0.01}$	11
P3_90a	ELM	3.900	$1.17^{+0.10}_{-0.13}$	0.22±0.03	0.33±0.01	11
P3_98a	ELM	3.980	0.84±0.19	$0.32^{+0.08}_{-0.06}$	0.40±0.03	11
P4_06a	ELM	4.060	$0.81^{+0.12}_{-0.13}$	0.12±0.02	0.28±0.01	11
P4_10a	ELM	4.100	$0.81^{+0.15}_{-0.13}$	$0.25^{+0.03}_{-0.02}$	0.37±0.01	11
P4_36a	ELM	4.360	$0.92^{+0.14}_{-0.09}$	$0.26^{+0.05}_{-0.04}$	0.39±0.02	11
P4_41a	ELM	4.410	$0.82^{+0.07}_{-0.09}$	$0.20^{+0.03}_{-0.02}$	0.35±0.01	11
P4_47a	ELM	4.470	$0.82^{+0.18}_{-0.14}$	$0.20^{+0.14}_{-0.08}$	$0.36^{+0.07}_{-0.05}$	11
P4_73a	ELM	4.730	$0.85^{+0.11}_{-0.13}$	$0.23^{+0.05}_{-0.03}$	0.38±0.01	11
P5_17a	ELM	5.170	$0.44^{+0.11}_{-0.07}$	$0.15^{+0.04}_{-0.03}$	0.37±0.03	11
P5_42a	ELM	5.420	0.71±0.06	0.18±0.02	0.40±0.01	11

Table A.2: Evolved CV systems, with known masses and donor radius. **References:** (1) Ritter and Kolb (2003); (2) Ashley et al. (2020); (3) Rodríguez-Gil et al. (2009); (4) Staude et al. (2001); (5) Yu et al. (2019); (6) Beuermann et al. (2022); (7) Echevarría et al. (2008); (8) Gomez et al. (2021); (9) Sokolovsky et al. (2022); (10) Echevarría et al. (2007); (11) El-Badry et al. (2021), see this reference for the Gaia eDR3 ID of these systems.

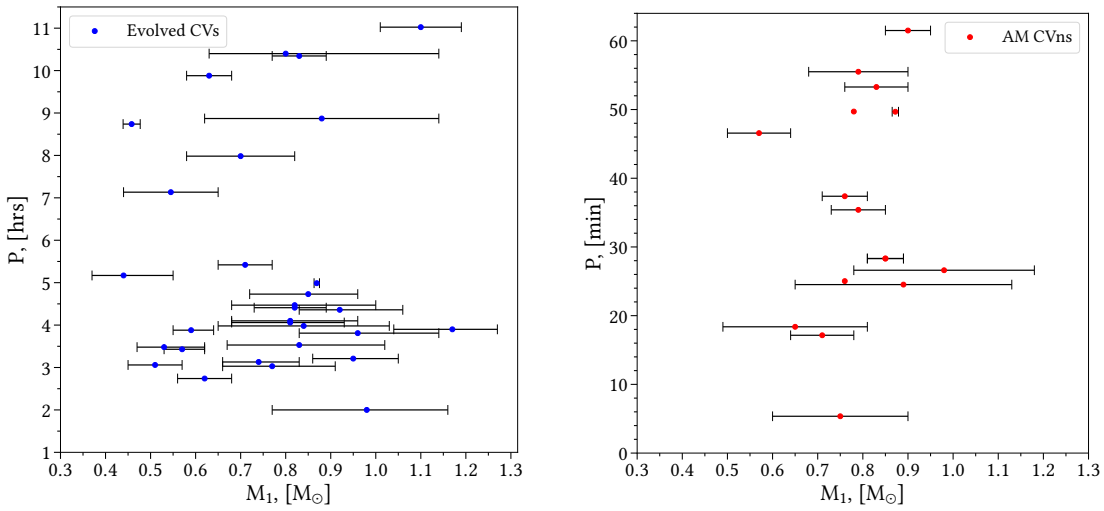

Figure A.1: The WD masses with respect to the orbital periods of the evolved CVs and AM CVns.

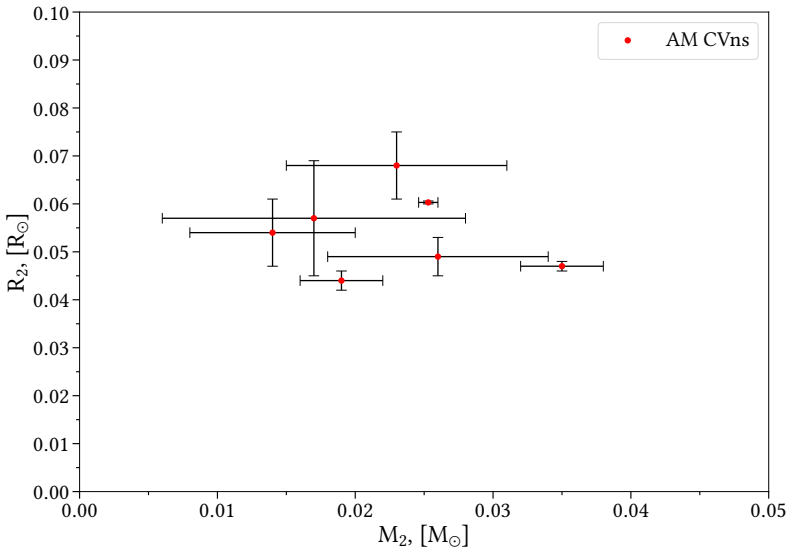

Figure A.2: The donor radii with respect to their masses for the AM CVns. Note that there are not a lot of the AM CVns in the data, which has estimated donor radii, hence only a few systems are shown.

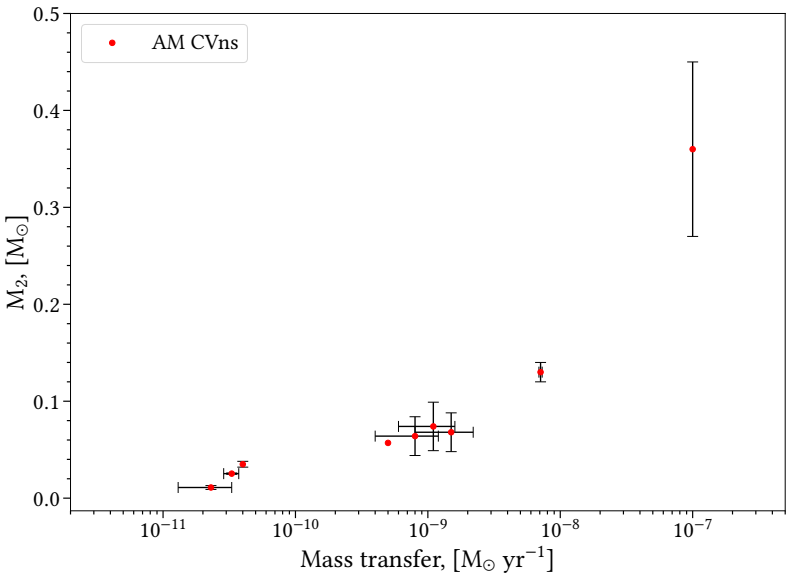

Figure A.3: The donor mass with respect to the mass transfer rates for the AM CVns.

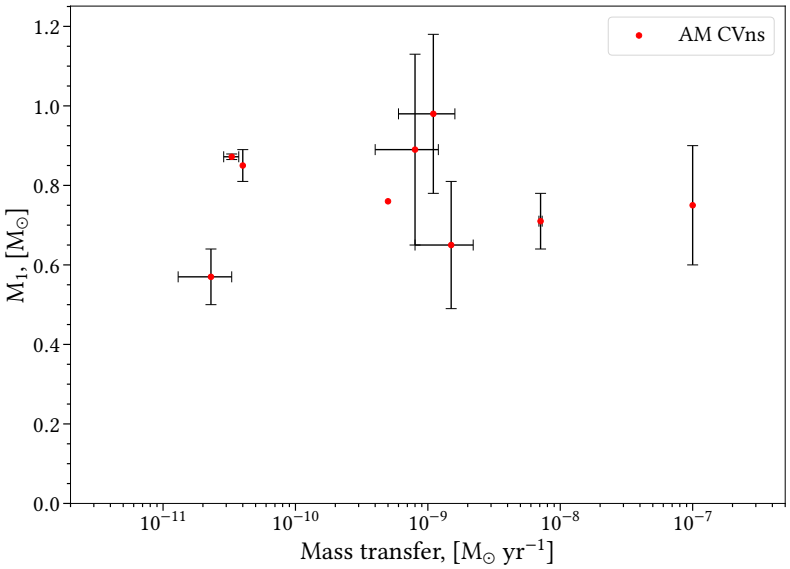

Figure A.4: The WD mass with respect to the mass transfer rates for the AM CVns.

Supplementary Simulation Plots

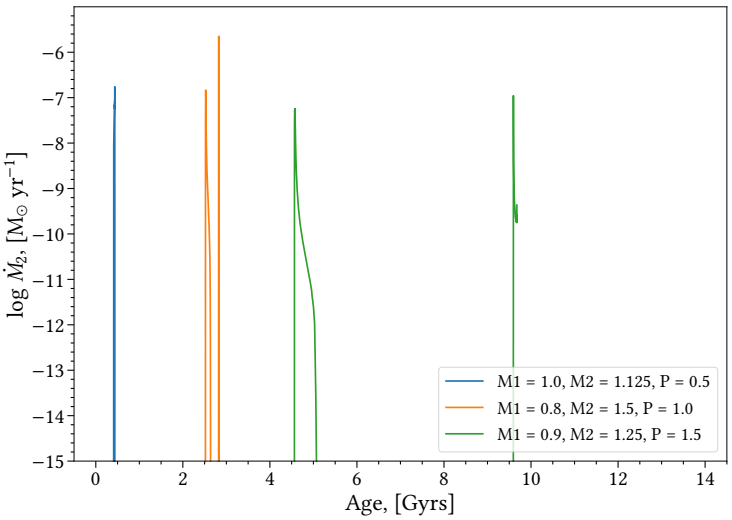

Figure B.1: The mass transfer rates throughout the three systems evolutions.

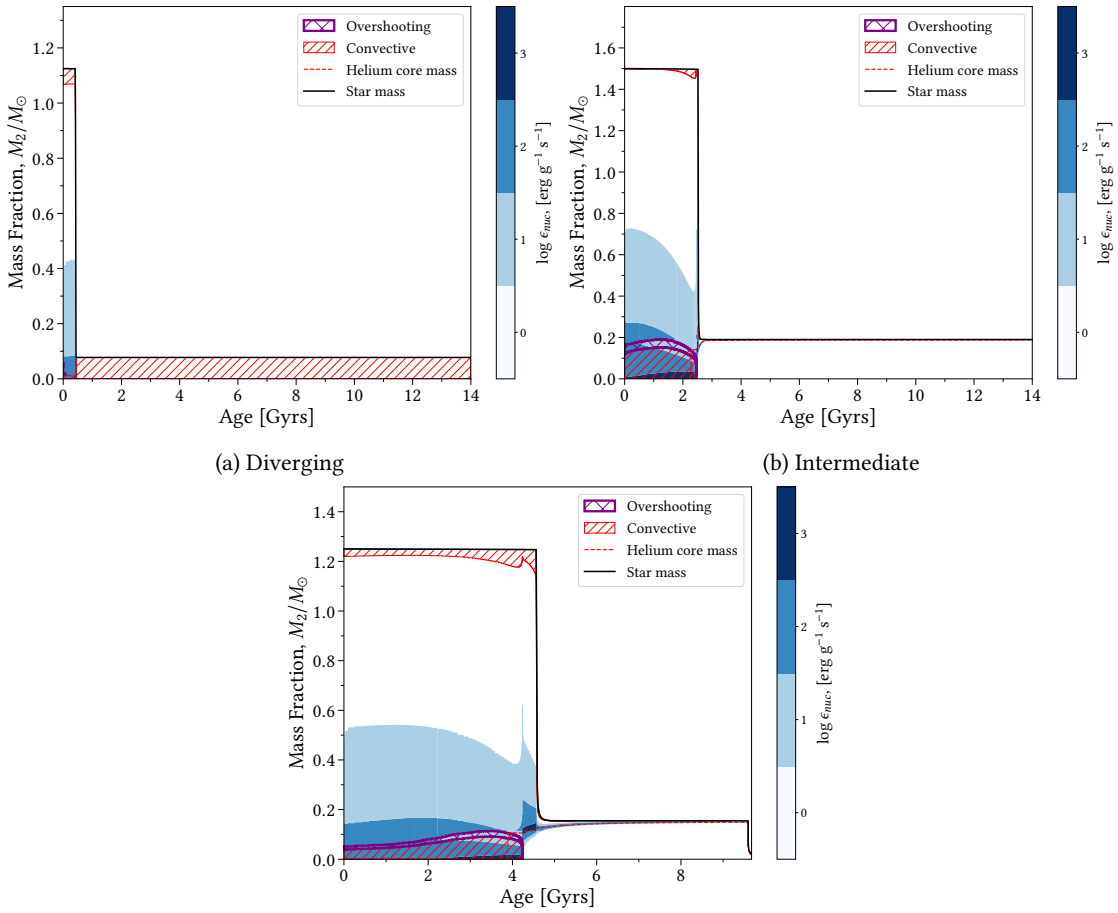

(a) Diverging

(b) Intermediate

(c) Converging

Figure B.2: Kippenhahn diagrams showing the structure of the star in terms of mass fraction and age, for the diverging (top left), intermediate (top right) and converging system (bottom). The blue areas are the burning regions of the star. A color scale is seen to the right corresponding to the logarithm of the energy generation from fusion processes.

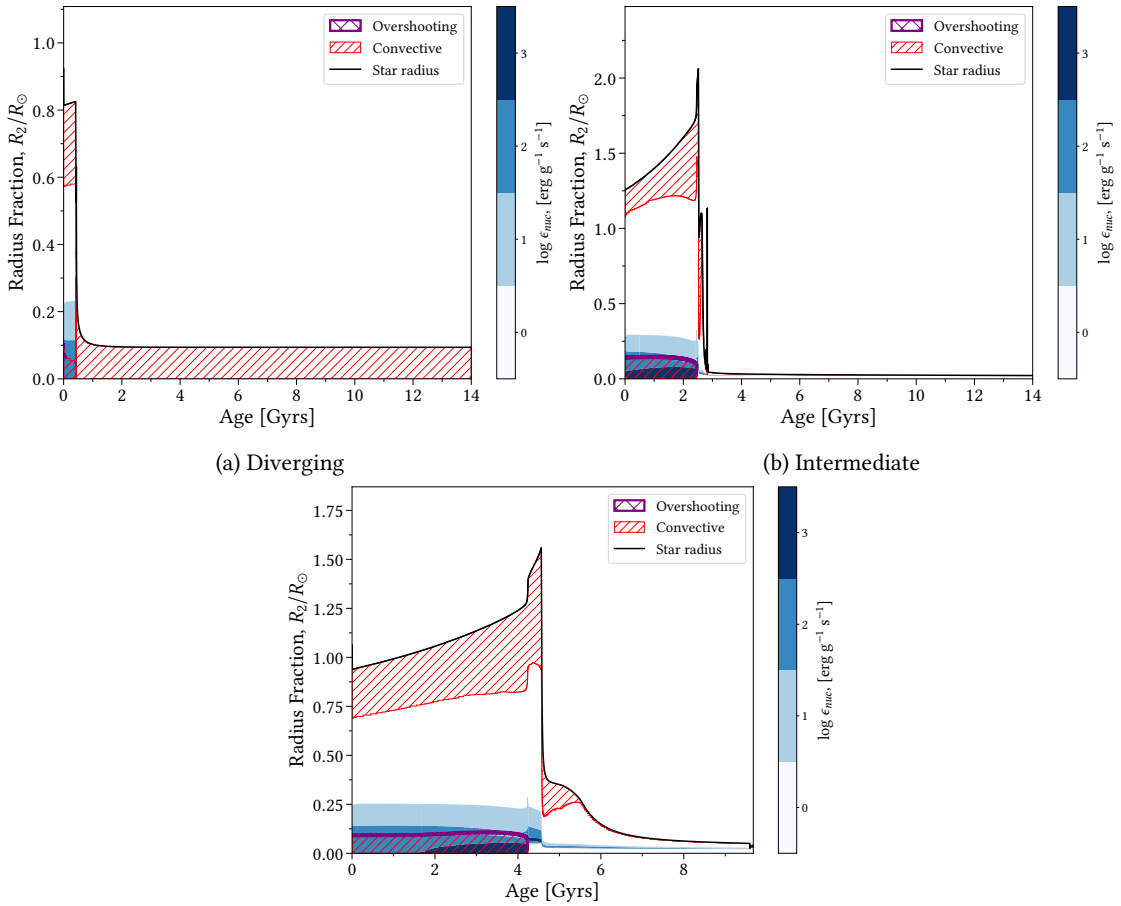

(a) Diverging

(b) Intermediate

(c) Converging

Figure B.3: Kippenhahn diagrams showing the structure of the star in terms of radius fraction and age, for the diverging (top left), intermediate (top right) and converging system (bottom). The blue areas are the burning regions of the star. A color scale is seen to the right corresponding to the logarithm of the energy generation from fusion processes.

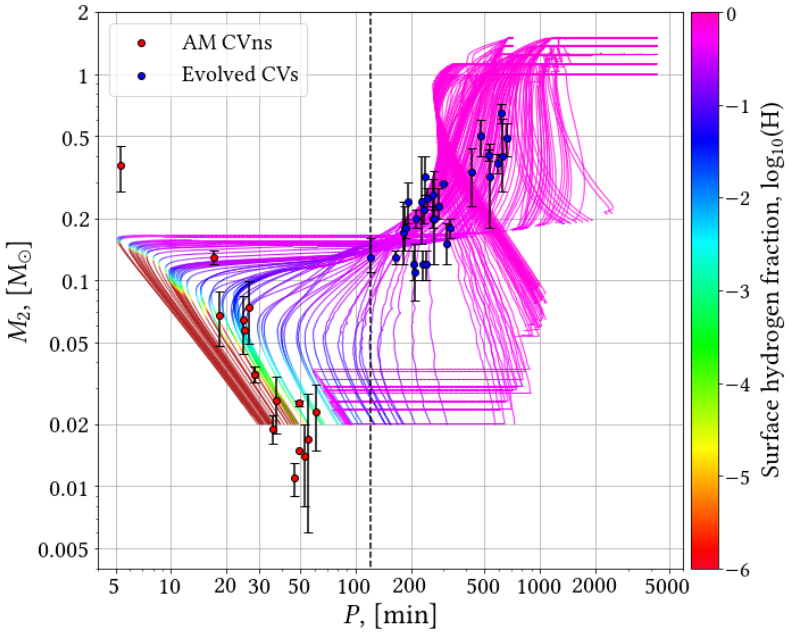

Figure B.4: The donor mass with respect to the orbital period of all simulated systems in our initial grid. The observational data for the AM CVns and evolved CVs has been plotted as red and blue dots respectively, along with known errors.

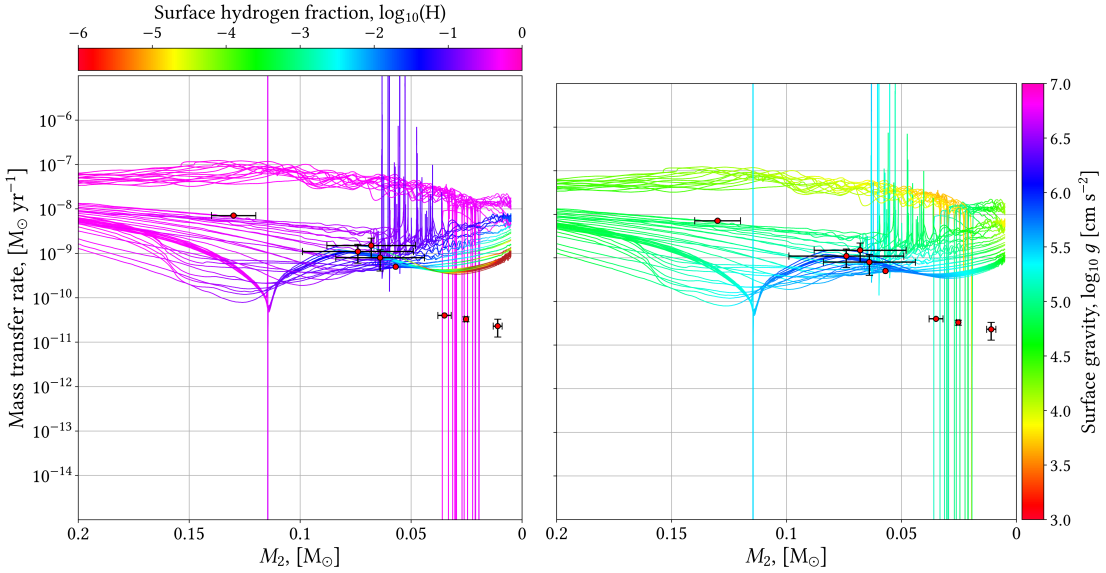

Figure B.5: The mass transfer in terms of the donor mass of our simulated systems, which reach periods $P < 2$ hrs, but where MESA did not initiate the WD cooling sequence. Two color scales have been used, one for the surface hydrogen abundance (left) and one for the surface gravity (right) of the donor. A median and gaussian filter has been used to smooth the data to remove simulation noise. The observational data for the AM CVns has been plotted as red dots, along with known errors.

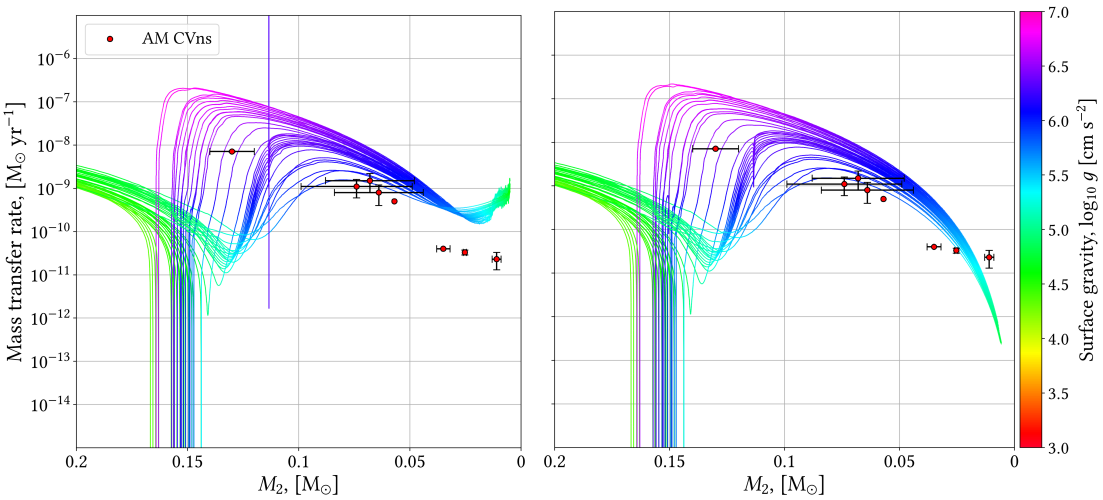

Figure B.6: The mass transfer in terms of the donor mass of our simulated systems, which reach periods $P < 2$ hrs and MESA starts the WD cooling sequence for the donor. The color scale shows the surface gravity of the donor. Note two sets of simulation is shown, one where MB is allowing during the WD cooling sequence (left), and one where MB is turned off once the donor reaches this phase (right). A median and gaussian filter has been used to smooth the data to remove simulation noise. The observational data for the AM CVns has been plotted as red dots, along with known errors.

Smoothing of Mass Transfer Rates

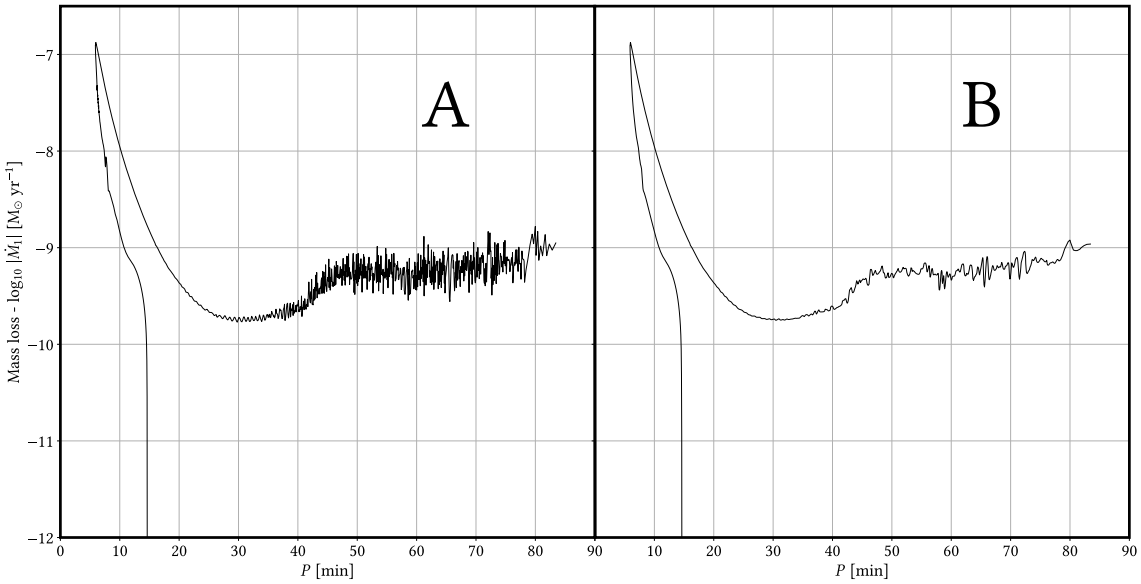

Figure C.1: Visual consequences of using median and gaussian smoothing on the mass transfer rates. Here the mass loss of the donor is plotted with respect to the orbital period for a system with initial parameters: $M_{1,0} = 0.7\ \mathrm{M}_\odot$, $M_{2,0} = 1.35\ \mathrm{M}_\odot$ and $P_0 = 1.0$ days.

Figure C.1A shows the non-smoothed data for mass loss of the donor with respect to the orbital period. Figure C.1B shows the smoothed plot. The data has been smoothed by first applying a median filter which replaces the values with the median value within a neighborhood of 5 entries around the values. This helps remove sudden and sharp spikes in the data set. Then a gaussian filter is applied to create smooth transitions between data point.